UNIVERSITY OF CAPE TOWN
IYUNIVESITHI YASEKAPA • UNIVERSITEIT VAN KAAPSTAD

Shell finite elements, with applications in biomechanics

by

Samantha Bartle

Thesis Presented in partial fulfillment
for the Degree of
MASTER OF SCIENCE IN ENGINEERING
in the Department of Mechanical Engineering
UNIVERSITY OF CAPE TOWN
April 2009

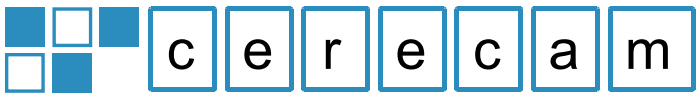

Plagiarism declaration

I know the meaning of plagiarism and declare that all of the work in the document, save for that which is properly acknowledged, is my own.

Signed: .....

Date: 24 - 04 - 2009

Shell finite elements, with applications in biomechanics

Samantha Bartle
University of Cape Town

Abstract

This thesis gives a detailed presentation of a formulation for thin shells, and its finite element approximation, with the goal of modelling soft, thin biological tissues. The rigorous but complex theory due to Simo and Fox (1986) is presented in an accessible manner, with detailed derivations where appropriate. The presentation is confined to small strains and linear elasticity, with the constitutive theory extended to take account of transverse isotropy.

The finite element formulation is given in such a way as to make various implementational aspects clear. Implementation has been carried out in deal.II, an open source library of finite element code. Substantial detail is given about how the shell formulation was implemented; this includes preprocessing, programming of the solution algorithm, and post-processing of results.

The formulation is tested against a series of benchmark problems for flat plates and cylindrical shells, under a variety of loading conditions, and compared with results in the literature.

Two example problems in biomechanics are considered: the problem of arterial clamping, and the modelling of a prosthetic aortic valve. In the case of the clamped artery, the deformed shape for a range of clamp depths compares well with results in the literature obtained using a three-dimensional formulation. The addition of helical fibre families orientated in the same manner as two different arterial layers significantly altered the resulting deformations and agreed qualitatively with those in the literature. Using the geometric and material parameters given in earlier studies of prosthetic aortic valve leaflets, the shell solution algorithm was used to simulate a leaflet with and without transverse isotropy. The deformed leaflet behaved as expected for a diastolic state and showed a significant increase in load carried by the aortic wall with the inclusion of fibres.

The work concludes with suggestions for extensions to include, for example, large strains and nonlinear material models.

A thousand thank-you's

Some mention must be made to the individuals without whom this completed master's thesis would not have been possible. Firstly, my deepest gratitude goes to the untiring and patient guidance of my supervisor Professor Daya Reddy in helping with an often daunting topic. I am continually amazed and inspired by the interest he shows in the endevours of all his students. I can never fully express my thanks for all the time, computational expertise and empathy freely given by my cosupervisor Andrew McBride. I am also indebted to my office friends at CERECAM who at various points offered help, support and large quantities of baked goods. I would especially like to mention Helen, Yaseen, Kevin, J.P, Victor, Olivia, Case and Karl. I am so very fortunate to have many close friends without whose love and support I would've endured many more struggles over the past two years. There are too many to name, but much gratitude goes to Meghan, Claire, Thandi, Dine, Nom, Odette, Benjamin, Gunther, Barry and Nick and especially to my two wonderful housemates Lyndi and Sean. I am blessed with a close and supportive family and words fail in expressing how thankful I am for their love and understanding in all my endevours. Much appreciation to Parents and sister: Trevor, Jannette and Candice. Finally, in the end all the glory goes to my Saviour and King Jesus Christ, without whose freely given grace all earthly achievements would cease to matter.

Contents

List of Figures

1

Introduction

Current statistics for patients in need of heart transplants, valve replacements, hip replacements, bypasses, and the like, make clear certain realities of the human body. Whether it be lifestyle related or genetic, certain essential organs in the human body can wear out, become diseased or damaged in various ways.

In attempts to address these challenges there has been a great deal of research into the development of prosthetic devices. However, this path has been fraught with difficulites in attempting to reproduce the complex behaviour of natural biological materials, which are generally highly nonlinear and anisotropic. The challenges facing developers of prosthetic implants include that of understanding exactly how biological materials respond to physiological loading conditions. Further issues include being able to design a prosthetic implant that will function in the correct manner, not conflict with the surrounding tissue, withstand repeated loading, and have a realistic lifespan. It is also necessary to be able to test prosthetic designs sufficiently thoroughly to be confident of their ability to function successfully after implantation.

The process of building and testing prototypes, either using specific testing rigs or animals, is costly and time-consuming. Mathematical and computational modelling offers a further avenue of investigation. Using the principles of continuum mechanics, the complexity of biological materials and their behaviour can, in

principle, be captured as a mathematical model, and realistic computational simulations developed by using an approximation method such as finite elements.

Useful to the design process, is the ease with which material and loading parameters can be adjusted to examine their effect on the system. It is also important to validate simulations against experimental test results in order for there to be a reasonably good level of confidence about their ability to model more complex situations realistically and accurately.

1.1 Motivation for and background to this thesis

The work in this thesis is motivated by the challenges specific to the modelling of soft biological tissues and prostheses which are considered to be thin. These include heart valves and, in some cases, blood vessels. The term thin is intended to describe a structure in which one length dimension is much smaller than the other two.

Shell theory provides the appropriate framework for the study of thin structures. The theory is based on the general principles of continuum mechanics, but takes into account the fact that the structure is thin, in the sense described above.

Since the theory of shells and associated numerical aspects are complex, a substantial focus of this thesis is to present a full development of shell theory, together with finite element approximations. Examples and applications involving arteries and heart valves are then treated using the theory. The shell theory and associated finite element approximations developed by Simo and Fox [29] are used as the basis of this study.

There are a number of commercially available finite element packages that are able to treat problems of the kind discussed here, with the minimum of input by the user. An approach using packages has the disadvantage, though, of not necessarily being

sufficiently flexible to accommodate the underlying theory, the full range of material types, and element types, depending on the extensions that are anticipated.

It was therefore decided to implement the shell theory used in this thesis in a library of finite element code known as deal.II. There are a number of reasons that this was done, which will now be described.

The theory due to Simo and Fox has a rigorous grounding and is devoid of many of the complications inherent in other shell theories. There is currently no documented commercial package which uses the Simo-Fox theory as the basis for shell finite element approximations.

The intention therefore is to lay the groundwork for an approach which can address problems in the modeling of thin biological materials, in a manner which will allow for future extensions: for example, the use of more sophisticated material models which take into account nonlinear material properties of biological tissues, fluid-structure interactions within blood vessels and heart valves, large strains, dynamic effects, as well as a diverse range of material models. Whilst there are means within certain commercial packages to add nonlinearity and anisotropy, for example by making use of specific user elements, the framework of such packages will often be a limiting factor.

A further motivation for the use of a general library is that the work reported in this thesis is carried out in a computational research environment in which the sharing of resources and knowledge is highly valued. Thus the development of an in-house open-source library of finite element code that has broad applications is deemed a worthwhile goal in itself.

1.2 Key objectives and aims of this thesis

A good understanding of any shell theory requires a significant investment of time and effort. The Simo-Fox theory is no exception, and therefore one aim of the thesis is to present the theory in a manner which would be more readily understood by researchers encountering it for the first time. The same considerations apply to the development of finite element approximations based on this theory.

The aims of the thesis are therefore as follows:

a) to present in an accessible and digestible manner the Simo and Fox shell theory and finite element approximations, in the context of small strains and linear elasticity

b) to make provision for very thin shells in the theory and approximations

c) to give a detailed presentation of the implementational aspects of the shell theory using the library of finite element code, deal.II

d) to validate the formulation using a series of problems available in the literature

e) to apply the working code to selected problems in biomechanics

1.3 Outline of the Dissertation

The remainder of this thesis is structured as follows. Chapter 2 presents the shell theory, in particular shell geometry and kinematics, generalized stresses and strains, balance laws, and elastic constitutive relations. Chapter 3 gives a detailed exposition of finite element approximations for shells, including the final form to be implemented computationally.

Chapter 4 describes the implementation in terms of the geometry, the preprocessing work necessary, and the structure of the code using deal.II. The various benchmarking tests performed to ascertain the functioning of the shell formulation are described in Chapter 5. Chapter 6 will shift the focus to the motivation for this work by presenting two examples from biomechanics, viz. a clamped artery problem, and the prosthetic heart valve leaflet.

Conclusions, recommendations and final remarks are presented in Chapter 7.

2

Shell Theory

Within the scope of this thesis, a shell is a plane or curved structure whose thickness is substantially less than that of its other dimensions. For the ultimate goal of modelling thin biological tissues, a robust shell theory is required.

There are several possible formulations of shell theories. These generally fall into two categories. In the first of these, often referred to as the classical approach, the shell is defined according to the properties of its midsurface and the kinematics and constitutive relations are obtained by utilising this description in relation to the three-dimensional equations. This approach, begun by the fundamental work of the Cosserats [18], was further developed and refined by Ericksen and Truesdell [19] and Cohen and DeSilva [17], to name a few.

The second approach, known as the three-dimensional "degenerated concept", utilises the equations of a three-dimensional solid and then introduces the assumptions of shell kinematics at the discretized level [32]. The origins of this methodology can be found in the paper of Ahmed, Irons and Zienkiwicz [11], and further development in the works of Ramm [27] and Hughes and Carnoy [24].

We will adopt the classical approach based on the midsurface definition as presented by Simo and Fox [29], who use a model of a shell as a midsurface with a director defined at each point. The theory is complex and makes use of concepts from

differential geometry. The objectives of this chapter are to present the theory in a systematic and easily digestible manner, as well as to describe the essential parts of the formulation in such a way as to provide the appropriate foundation for numerical approximations.

2.1 Setting out Shell Theory Formulation

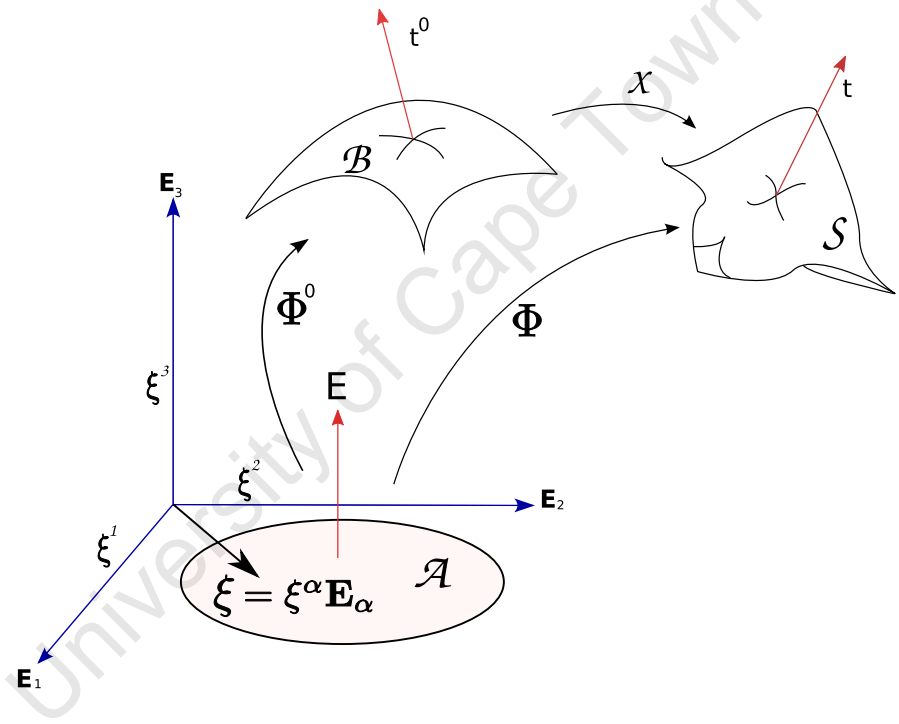

Fig. 2.1. Visualisation of the shell model kinematics

Figure 2.1 sets out the system that will be described. $\{\mathbf{E}_I\}_{I=1,2,3}$ defines a fixed inertial frame. The reference configuration of the midsurface of the shell, labelled $\mathcal{B}$, in $\mathbb{R}^3$ is generated by a map from the surface $\mathcal{A}$, lying in the $\xi^1 - \xi^2$ plane. This mapping is denoted by $\boldsymbol{\Phi}^0$. Similarly, $\boldsymbol{\Phi}$ denotes the mapping from $\mathcal{A}$ to the current configuration of the midsurface, denoted by $\mathcal{S}$.

The basic kinematic representation for the shell surface is that of an inextensible one-director Cosserat surface. A Cosserat surface is a deformable surface in a three-dimensional Euclidean space which has a deformable vector associated with each point [4]. The theory to follow incorporates these vectors, known as directors, into the model. In Figure 2.1 , $\mathbf{t}^0$ shows an arbitrary director for the shell surface in the reference configuration, and $\mathbf{t}$ the director in the deformed configuration. The director $\mathbf{t}^0$ need not be normal to the midsurface.

Consider a position vector $\boldsymbol{\xi} = \xi^1\mathbf{E}_1 + \xi^2\mathbf{E}_2$ in the surface $\mathcal{A}$ in $\mathbb{R}^2$. In the reference configuration, surface $\mathcal{B}$ is defined by the mapping $\boldsymbol{\Phi}^0$ from $\mathcal{A}$. The position vector of an arbitrary point in the reference configuration of the shell is given by

$$\begin{aligned}\mathbf{x}^0 &= \boldsymbol{\Phi}^0(\xi^1, \xi^2, \xi) \\ &= \boldsymbol{\varphi}^0(\xi^1, \xi^2) + \xi\mathbf{t}^0(\xi^1, \xi^2),\end{aligned}$$

where $\boldsymbol{\varphi}^0$ defines the midsurface position vector, $\mathbf{t}^0$ defines a unit vector field at that point on the surface, with $h^- \leq \xi \leq h^+$ and $h = h^+ - h^-$ being the thickness of the shell. This is illustrated in Figure 2.2. Similarly, the deformed configuration is also

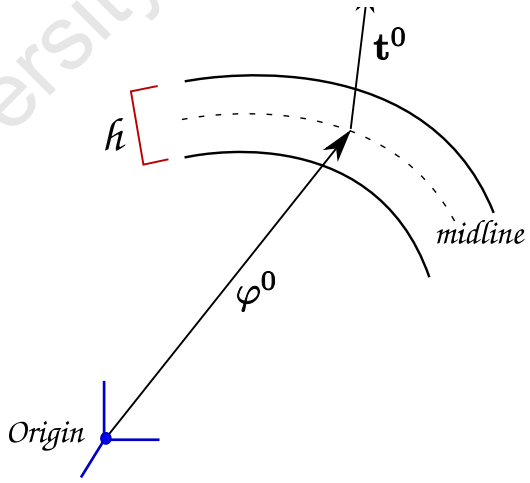

Fig. 2.2. Illustration of the midsurface and director of an arbitrary shell section

given as a mapping from the same fixed frame. The current configuration $\mathcal{S}$ is given by the mapping $\boldsymbol{\Phi}$ from $\mathcal{A}$. Therefore, the position vector of an arbitrary point in this configuration is given by

$$\mathbf{x} = \boldsymbol{\Phi}(\xi^1, \xi^2, \xi) \tag{2.1}$$

$$= \boldsymbol{\varphi}(\xi^1, \xi^2) + \xi \mathbf{t}(\xi^1, \xi^2) \tag{2.2}$$

Note: It is assumed that the shell does not undergo any change in thickness.

2.1.1 Shell Deformation

As shown in Figure 2.1, the deformation of the shell from the reference to the current configuration is given as the mapping

$$\boldsymbol{\chi} : \mathcal{B} \longrightarrow \mathcal{S}$$

where

$$\boldsymbol{\Phi} = \boldsymbol{\chi}\left(\boldsymbol{\Phi}^0\right).$$

The tangent map of $\boldsymbol{\Phi}$ is given by

$$\nabla \boldsymbol{\Phi} = \frac{\partial \boldsymbol{\Phi}}{\partial \xi^I} \otimes \mathbf{E}^I$$

$$= \mathbf{g}_I \otimes \mathbf{E}^I \tag{2.3}$$

where $I = 1, 2, 3$ and $\mathbf{g}_I = \dfrac{\partial \boldsymbol{\Phi}}{\partial \xi^I}$ is referred to as the convected basis, and $\otimes$ is the tensor product. Here and henceforth the summation convention in repeated indices is used. The deformation gradient $\boldsymbol{F}$ has components given by

$$F_{ij} = \frac{\partial x^i}{\partial x^{j^0}} = \frac{\partial \Phi^i}{\partial \xi^I}\frac{\partial \xi^I}{\partial \Phi^{j^0}}.$$

That is,

$$\mathbf{F} = \nabla \boldsymbol{\Phi} \cdot \left(\nabla \boldsymbol{\Phi}^0\right)^{-1}. \tag{2.4}$$

Following from the definition of $\boldsymbol{\Phi}$ in (2.1), equation (2.3) becomes

$$\begin{aligned} \nabla \boldsymbol{\Phi} &= (\boldsymbol{\varphi}_{,\alpha} + \xi \mathbf{t}_{,\alpha}) \otimes \mathbf{E}^\alpha + \mathbf{t} \otimes \mathbf{E} \\ &= \mathbf{g}_\alpha \otimes \mathbf{E}^\alpha + \mathbf{g}_3 \otimes \mathbf{E} \qquad , \end{aligned} \tag{2.5}$$

where the subscript $(\,),\alpha$ indicates the derivative with respect to ξ^α, and $\mathbf{E} = \mathbf{E}^3$. Here and henceforth Greek indices range over 1 to 2.

In order to determine the Jacobian of the deformation gradient J, we begin by defining

$$j = \det[\nabla \boldsymbol{\Phi}],$$
$$j^0 = \det[\nabla \boldsymbol{\Phi}^0]..$$

Then from (2.4),

$$J = \det[\boldsymbol{F}] = \frac{j}{j^0}.$$

Given a basis $\mathbf{g}_I$, the reciprocal basis $\mathbf{g}^I$ is defined by $\mathbf{g}_I \cdot \mathbf{g}^J = \delta_I^J$, where δ_I^J is the Kronecker delta. Hence $\mathbf{g}^I$ is perpendicular to $\mathbf{g}_J$, for $I \neq J$. Figure 2.3 illustrates this concept.

From (2.3),

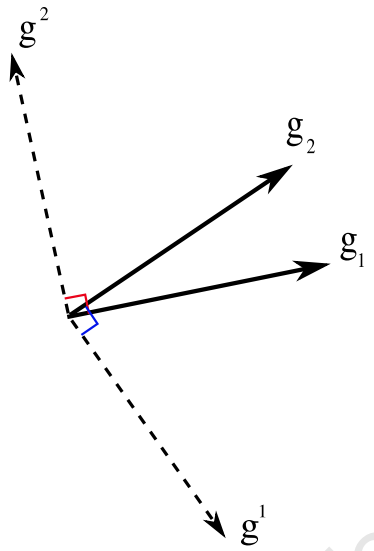

Fig. 2.3. Illustration of the reciprocal basis relationship

$$\mathbf{g}_I = (\nabla \boldsymbol{\Phi})\, \mathbf{E}_I, \tag{2.6}$$

and thus

$$\mathbf{g}^I = \nabla \boldsymbol{\Phi}^{-T} \mathbf{E}^I, \tag{2.7}$$

where $\boldsymbol{E}^I = \boldsymbol{E}_I$.

2.1.2 Frames of reference on the midsurface

There are two other reference frames crucial to the development of the shell formulation that must now be defined. They are the surface convected frame and the director orthogonal frame. $\{\mathbf{a_I}\}_{I=1,2,3}$ defines the surface convected frame where $\{\mathbf{a}_\alpha\}_{\alpha=1,2}$ represents the tangent basis to the midsurface, defined by

$$\boldsymbol{a}_\alpha = \frac{\partial \boldsymbol{\varphi}}{\partial \xi^\alpha} \tag{2.8}$$

and depicted in Figure 2.4. From equations (2.3) and (2.5),

$$\begin{aligned}\mathbf{g}_\alpha &= \frac{\partial \boldsymbol{\varphi}}{\partial \xi^\alpha} + \xi \frac{\partial \boldsymbol{t}}{\partial \xi^\alpha} \\ &= \mathbf{a}_\alpha + \xi \boldsymbol{t}_{,\alpha},\end{aligned}$$

and

$$\boldsymbol{g}_3 = \boldsymbol{a}_3 = \mathbf{t}.$$

.

$\{\mathbf{t_I}\}_{I=1,2,3}$ defines the director orthogonal frame. This frame is constructed using the orthogonal transformation $\boldsymbol{\Lambda}$, which maps the outward normal $\mathbf{E}$ of the surface $\mathcal{A}$, in $\mathbb{R}^2$, to the director $\mathbf{t}$ in the shell configuration in $\mathbb{R}^3$; that is,

$$\boldsymbol{t}_3 = \boldsymbol{t} = \boldsymbol{\Lambda} \boldsymbol{E}. \tag{2.9}$$

Then $\{\mathbf{t}_\alpha\}_{\alpha=1,2}$ are defined by

$$\boldsymbol{t}_\alpha = \boldsymbol{\Lambda} \boldsymbol{E}_\alpha.$$

See Figure 2.4.

It is also useful at this point to record an explicit formula for $\boldsymbol{\Lambda}$, derived in [29]:

$$\boldsymbol{\Lambda} = (\boldsymbol{E} \cdot \boldsymbol{t})\, \boldsymbol{I} + [\widehat{\boldsymbol{E} \times \boldsymbol{t}}] + \frac{1}{1 + \boldsymbol{E} \cdot \boldsymbol{t}} (\boldsymbol{E} \times \boldsymbol{t}) \otimes (\boldsymbol{E} \times \boldsymbol{t}). \tag{2.10}$$

The operator $\widehat{(\cdot)}$ is the tensor defined by

$$\widehat{\boldsymbol{\Theta}} \boldsymbol{h} = \boldsymbol{\Theta} \times \boldsymbol{h}, \tag{2.11}$$

for any vector $\boldsymbol{h}$.

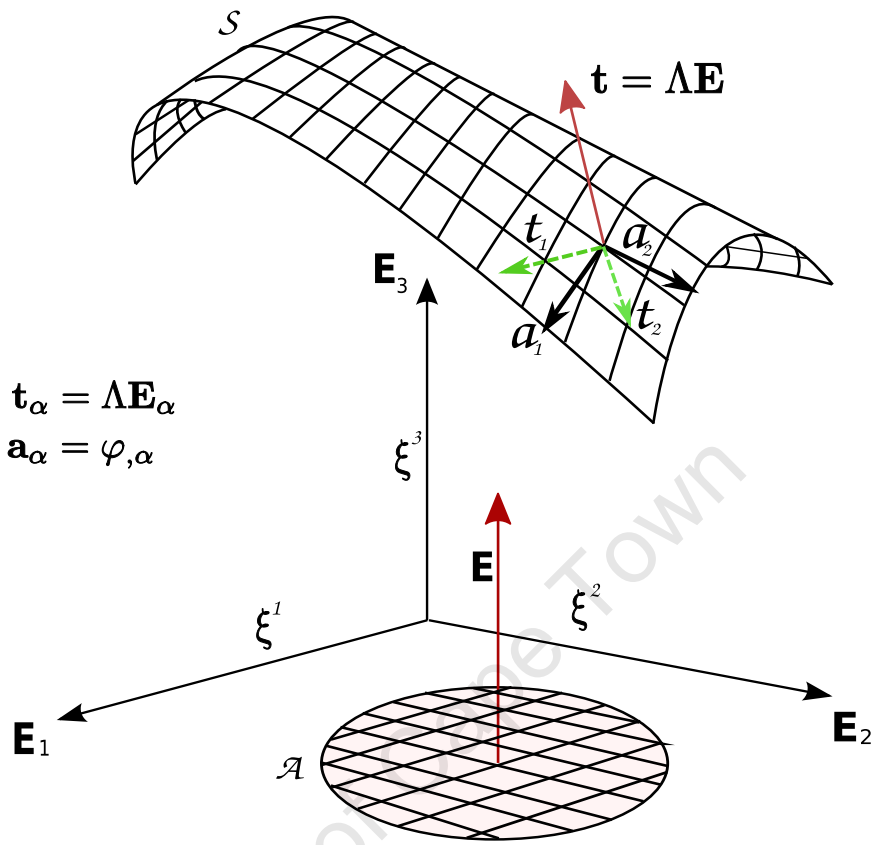

Fig. 2.4. Depiction of the important reference frames in the shell formulation

Mid-surface Jacobians can now be defined by

$$\bar{j}^0 = |\mathbf{a}_1^0 \times \mathbf{a}_2^0|, \qquad \bar{j} = |\mathbf{a}_1 \times \mathbf{a}_2|,$$

and so we can define

$$\bar{J} = \frac{\bar{j}}{\bar{j}^0}.$$

An element of midsurface area in the reference configuration is therefore given by

$$d\boldsymbol{A}^0 = \mathbf{a}_1^0 \times \mathbf{a}_2^0 d\xi^1 d\xi^2,$$

and similarly for the current configuration, by

$d\boldsymbol{A} = \mathbf{a}_1 \times \mathbf{a}_2 d\xi^1 d\xi^2$.

2.2 Incremental changes in the director vector

The transformation (2.9), when applied to the reference configuration, gives

$$\boldsymbol{t}^0 = \boldsymbol{\Lambda}\boldsymbol{E}. \tag{2.12}$$

The director vector in the current configuration is given as

$$\boldsymbol{t} = \boldsymbol{t}^0 + \Delta\boldsymbol{t}.$$

$\boldsymbol{\Lambda}$ imparts a rotation on the system, and thus is an othogonal tensor, so that

$$\boldsymbol{\Lambda}^T = \boldsymbol{\Lambda}^{-1}. \tag{2.13}$$

Due to the assumption of small displacements, $\Delta\boldsymbol{t}$ satisfies

$$\Delta\boldsymbol{t} \cdot \boldsymbol{t}^0 = 0. \tag{2.14}$$

Substitute (2.14) for $\boldsymbol{t}$ using (2.12) so that

$$\begin{aligned} 0 &= \Delta\boldsymbol{t} \cdot \boldsymbol{t}^0 \\ &= \Delta\boldsymbol{t} \cdot \boldsymbol{\Lambda}\boldsymbol{E} \\ &= \boldsymbol{\Lambda}^T \Delta\boldsymbol{t} \cdot \boldsymbol{E} \\ &= \boldsymbol{\Lambda}^{-1} \Delta\boldsymbol{t} \cdot \boldsymbol{E}. \end{aligned}$$

We now set

$$\Delta \boldsymbol{T} = \boldsymbol{\Lambda}^{-1} \Delta \boldsymbol{t}. \tag{2.15}$$

Thus

$$\Delta \boldsymbol{T} \cdot \boldsymbol{E} = 0, \tag{2.16}$$

so that

$$\Delta \boldsymbol{T} = \Delta T_\alpha \boldsymbol{E}_\alpha. \tag{2.17}$$

This means $\Delta \boldsymbol{T}$ has only two components relative to the $\boldsymbol{E}^I$ basis. From (2.15) and (2.17) we may write in matrix form

$$\{\Delta \boldsymbol{t}\}_{3\times 1} = \bar{\boldsymbol{\Lambda}}_{3\times 2} \{\Delta \boldsymbol{T}\}_{2\times 1}, \tag{2.18}$$

where $\bar{\boldsymbol{\Lambda}}$ consists of the first two columns of $\boldsymbol{\Lambda}$.

2.3 Stress resultants

Consider two sections in the current configuration, $\mathcal{S}$, shown in Figure 2.5. These sections, $\mathcal{S}^2$ and $\mathcal{S}^1$, are taken along lines of constant ξ^1 and ξ^2 respectively. That is,

$$\mathcal{S}^\alpha = \{\mathbf{x} \in \mathbb{R}^3 | \mathbf{x} = \boldsymbol{\Phi}|_{\xi^\alpha = const}\}, (\alpha = 1, 2).$$

The normal to $\mathcal{S}^1$, which also defines an element of area, is described by

$$d\mathcal{S}^1 = j\mathbf{g}^1 d\xi^2 d\xi, \tag{2.19}$$

following the reciprocal basis relationship between $\mathbf{g}^1$ and $\mathbf{g}_2$. $d\mathcal{S}^2$ is defined in a similar fashion. Using $\boldsymbol{\sigma}$ to represent the symmetric Cauchy stress tensor in the current configuration, the force acting per unit length ξ^2 on $\mathcal{S}^1$ is given by

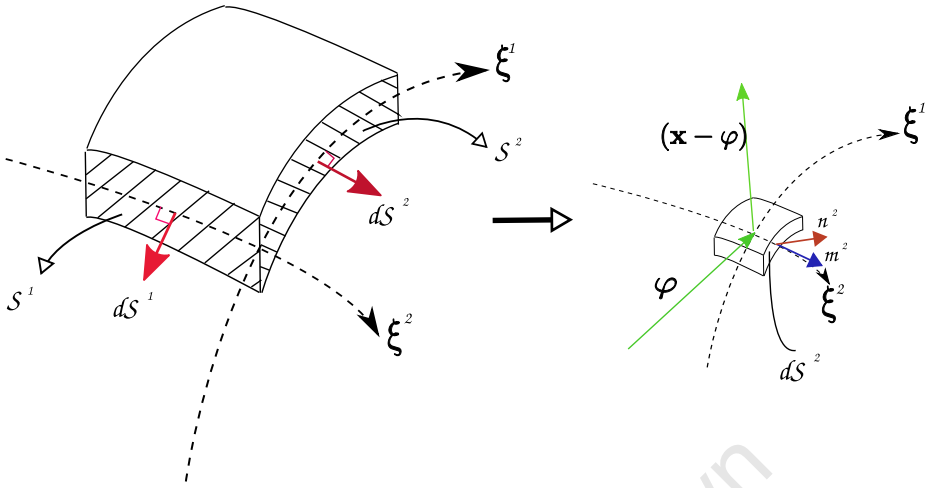

Fig. 2.5. Sections within the shell geometry of the current configuration

$$\mathbf{R}^1 = \int_{h-}^{h+} \boldsymbol{\sigma} \frac{d\mathcal{S}^1}{d\xi^2} = \int_{h-}^{h+} \boldsymbol{\sigma}\mathbf{g}^1 j d\xi. \tag{2.20}$$

The torque acting on $\mathcal{S}^1$ per unit ξ^2 is

$$\mathbf{T}^1 = \int_{h-}^{h+} (\mathbf{x} - \boldsymbol{\varphi}) \times \boldsymbol{\sigma}\mathbf{g}^1 j d\xi. \tag{2.21}$$

In a similar manner $\mathbf{R}^2$ and $\mathbf{T}^2$ can be defined. We are interested in the force and torque occurring within the surface convected frame, so normalising $\mathbf{R}^\alpha$ and $\mathbf{T}^\alpha$ with the mid-surface Jacobian allows for the definition of the stress resultant and stress couple, $\mathbf{n}^\alpha$ and $\mathbf{m}^\alpha$ respectively:

$$\mathbf{n}^\alpha = \frac{1}{\bar{j}} \int_{h-}^{h+} \boldsymbol{\sigma}\mathbf{a}^\alpha j d\xi \tag{2.22}$$

and

$$\mathbf{m}^\alpha = \frac{1}{\bar{j}} \int_{h-}^{h+} (\mathbf{x} - \boldsymbol{\varphi}) \times \boldsymbol{\sigma}\mathbf{a}^\alpha j d\xi. \tag{2.23}$$

There are two things to note at this juncture. Firstly, $\mathbf{m}^\alpha \cdot \mathbf{t} = 0$, so there is no component of the stress couple along director $\mathbf{t}$. This means that the shell surface experiences no "drilling" forces. Secondly, since $(\mathbf{x} - \boldsymbol{\varphi}) = \xi\mathbf{t}$, from equation (2.1), $\mathbf{m}^\alpha$ can be written as

$$\mathbf{m}^\alpha = \mathbf{t} \times \frac{1}{\bar{j}} \int_{h-}^{h+} \xi \boldsymbol{\sigma} \mathbf{a}^\alpha j d\xi \tag{2.24}$$

$$= \mathbf{t} \times \widetilde{\mathbf{m}}^\alpha. \tag{2.25}$$

The last quantity involving stress to be defined is the across-the-thickness-stress-resultant, $\mathbf{l}$, which is given by

$$\mathbf{l} = \frac{1}{\bar{j}} \int_{h-}^{h+} \boldsymbol{\sigma} \mathbf{g}^3 j d\xi. \tag{2.26}$$

2.3.1 Example: cylindrical shell

We illustrate the salient features of the theory presented thus far using the example of a quarter cylinder shown in Figure 2.6. Firstly, we note that the inertial frame basis ξ^α is given in terms of cylindrical coordinates (θ, r, z) by

$$\boldsymbol{\xi}^1 = \theta; \qquad \boldsymbol{\xi}^2 = r.$$

Defining the shell surface as described in (2.1) gives

$$\mathbf{x} = \boldsymbol{\Phi}\left(\xi^1, \xi^2, \xi\right) \tag{2.27}$$

$$= R\left(\cos\theta \boldsymbol{E}_1 + \sin\theta \boldsymbol{E}_2\right) + z\boldsymbol{E}_3 + \xi\boldsymbol{t}, \tag{2.28}$$

and the director vector is given by

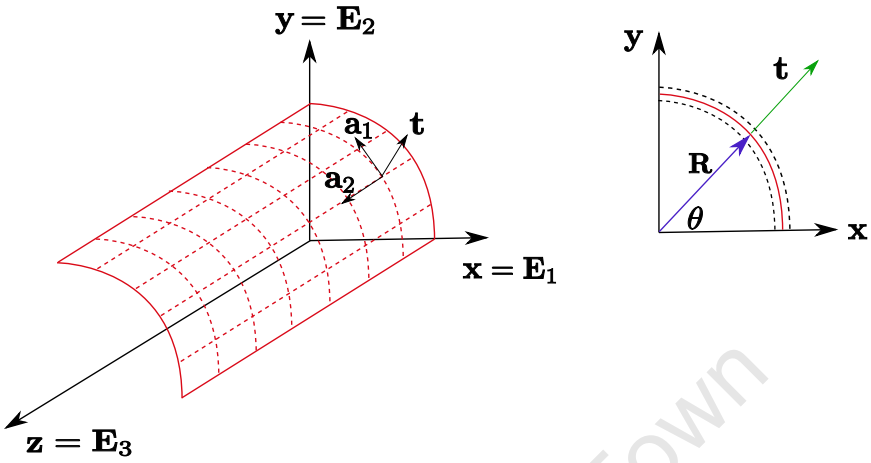

Fig. 2.6. Tangent vectors on the cylinder

$$\boldsymbol{t} = \cos\theta \boldsymbol{E}_1 + \sin\theta \boldsymbol{E}_2. \tag{2.29}$$

The convected basis can then be given by

$$\boldsymbol{g}_I = \frac{\partial \Phi}{\partial \xi^I} \boldsymbol{E}_I,$$

so that

$$\boldsymbol{g}_1 = \boldsymbol{g}_\theta = R\left(-\sin\theta \boldsymbol{E}_1 + \cos\theta \boldsymbol{E}_2\right), \tag{2.30}$$

$$\boldsymbol{g}_2 = \boldsymbol{g}_r = \boldsymbol{t}, \tag{2.31}$$

$$\boldsymbol{g}_3 = \boldsymbol{g}_z = \boldsymbol{E}_3. \tag{2.32}$$

Note the definition

$$\boldsymbol{e}^\theta = \left(-\sin\theta \boldsymbol{E}_1 + \cos\theta \boldsymbol{E}_2\right).$$

The rotation matrix $\boldsymbol{\Lambda}$ specifying the mapping from $\boldsymbol{E}$ to $\boldsymbol{t}$, as given in (2.9), can be shown to be

$$\boldsymbol{\Lambda}_{cyl} = \begin{bmatrix} \sin^2\theta & -\sin\theta\cos\theta & \cos\theta \\ -\sin\theta\cos\theta & \cos^2\theta & \sin\theta \\ -\cos\theta & -\sin\theta & 0 \end{bmatrix}.$$

Following the definition of the midsurface basis and using the geometry of the system,

$$\boldsymbol{a}_1 = \boldsymbol{g}_1 = R\left(-\sin\theta\boldsymbol{E}_1 + \cos\theta\boldsymbol{E}_2\right), \qquad \boldsymbol{a}_2 = \boldsymbol{E}_3. \tag{2.33}$$

The midsurface Jacobian is now simply determined by the length of the cross-product of $\boldsymbol{a}_1$ and $\boldsymbol{a}_2$ as

$$\boldsymbol{a}_1 \times \boldsymbol{a}_2 = R\left(\cos\theta\boldsymbol{E}_1 + \sin\theta\boldsymbol{E}_2\right).$$

Thus

$$|\boldsymbol{a}_1 \times \boldsymbol{a}_2| = \sqrt{(R\cos\theta)^2 + (R\sin\theta)^2} = R. \tag{2.34}$$

When calculating the stress resultant and stress couple we first consider the reciprocal basis $\boldsymbol{g}^I$. For the cylinder example $\boldsymbol{g}_I$ and $\boldsymbol{g}^I$ are parallel to each other, i.e.

$$\boldsymbol{g}^1 = \omega\boldsymbol{g}_1.$$

From (2.30),

$$\boldsymbol{g}_1 \cdot \boldsymbol{g}_1 = R^2$$

so that

$$\omega = \frac{1}{R^2}.$$

Therefore

$$\boldsymbol{g}^1 = \frac{1}{R}\boldsymbol{e}^\theta.$$

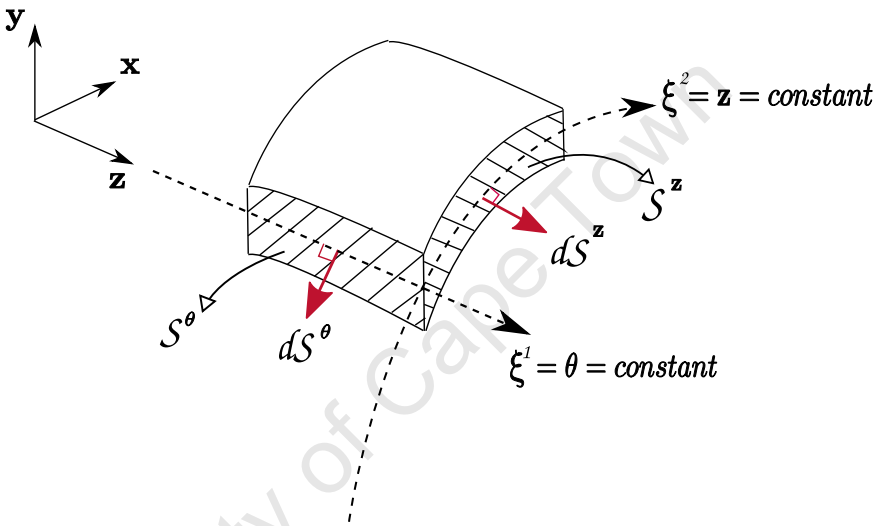

Fig. 2.7. Sections within the quarter cylinder

As in (2.19) and as indicated by Figure 2.7 , the normal to the section $\mathcal{S}^1$, or $\mathcal{S}^\theta$, is given by

$$\begin{aligned} d\mathcal{S}^\theta &= j\mathbf{g}^1 dz d\xi \\ &= j\frac{1}{R}\mathbf{e}^\theta dz d\xi. \end{aligned}$$

From (2.20) and (2.21), the force and and torque acting on $\mathcal{S}^\theta$ per unit length in the z direction are

$$\mathbf{R}^1 = \int_{h-}^{h+} \boldsymbol{\sigma} j \frac{1}{R} \boldsymbol{e}^\theta d\xi$$

and

$$\mathbf{T}^1 = \int_{h-}^{h+} (\mathbf{x} - \boldsymbol{\varphi}) \times \boldsymbol{\sigma} j \frac{1}{R} \boldsymbol{e}^\theta d\xi.$$

We note that for this case $\boldsymbol{g}_1 = \boldsymbol{a}_1$ and $j = R$, therefore upon normalising $\mathbf{R}^\alpha$ and $\mathbf{T}^\alpha$ with the mid-surface Jacobian we get

$$\begin{aligned}
\mathbf{n}^1 &= \frac{1}{\bar{j}} \int_{h-}^{h+} \boldsymbol{\sigma} \mathbf{a}^1 j d\xi \\
&= \frac{1}{R} \int_{h-}^{h+} \boldsymbol{\sigma} \frac{1}{R} \boldsymbol{e}^\theta R d\xi \\
&= \frac{1}{R} \int_{h-}^{h+} \boldsymbol{\sigma} \boldsymbol{e}^\theta d\xi
\end{aligned}$$

and

$$\begin{aligned}
\mathbf{m}^1 &= \frac{1}{\bar{j}} \int_{h-}^{h+} (\mathbf{x} - \boldsymbol{\varphi}) \times \boldsymbol{\sigma} \mathbf{a}^1 j d\xi \\
&= \frac{1}{R} \int_{h-}^{h+} (\xi \boldsymbol{t}) \times \boldsymbol{\sigma} \frac{1}{R} \boldsymbol{e}^\theta R d\xi \\
&= \frac{1}{R} \int_{h-}^{h+} (\xi \boldsymbol{t}) \times \boldsymbol{\sigma} \boldsymbol{e}^\theta d\xi
\end{aligned}$$

In a similar fashion the other components can be determined.

2.3.2 Equilibrium equations

Using the three-dimensional integral balance laws, the shell formulation equilibrium equations are the resultant form of the balance of forces and moments. The balance of forces is written as

$$\underbrace{\iint_{\partial\mathcal{V}} \boldsymbol{\sigma}\hat{\boldsymbol{\nu}}\, d\mathcal{S}}_{\text{total surface force}} + \underbrace{\iiint_{\mathcal{V}} \boldsymbol{b}\rho\, d\mathcal{V}}_{\text{total body force}} = \mathbf{0}, \tag{2.35}$$

where $\hat{\boldsymbol{\nu}}$ is the outward unit normal on the boundary $\partial\mathcal{V}$, and $\boldsymbol{b}$ denotes the body force per unit mass.

Using the vector in equation (2.1) which specifies the kinematic assumption in the shell formulation and equation (2.19) which gives the normal map relation from $\hat{\boldsymbol{\nu}}d\mathcal{S}$, (2.35) can be further expanded. Working on this expansion and using the definitions of the reciprocal basis, the midsurface, the above defined stress resultant (2.22), as well as the divergence theorem for surfaces it can be shown that the balance of forces becomes

$$\frac{1}{\bar{j}}\left((\bar{j}\mathbf{n}^{\alpha})_{,\alpha} + \bar{\mathbf{n}} = \mathbf{0}, \right. \tag{2.36}$$

where $\bar{\mathbf{n}}$ is the applied resultant force per unit length.

The equilibrium balance of moments is written as

$$\iint_{\partial\mathcal{V}} \boldsymbol{\Phi} \times \boldsymbol{\sigma}\hat{\boldsymbol{n}}\partial\mathcal{S} + \iiint_{\mathcal{V}} \boldsymbol{\Phi} \times \boldsymbol{b}\rho\partial\mathcal{V} = \mathbf{0}. \tag{2.37}$$

Employing the same techniques as mentioned above and again making use of the above defined stress and stress couple resultant (2.22), (2.23), it can be shown that the balance of moments becomes

$$\frac{1}{\bar{j}}\left((\bar{j}\mathbf{m}^{\alpha})_{,\alpha} + \mathbf{a}_{\alpha} \times \mathbf{n}^{\alpha} + \bar{\mathbf{m}} = \mathbf{0}, \right. \tag{2.38}$$

where $\bar{\mathbf{m}}$ is the applied resultant couple per unit length.

2.3.3 Constitutive restriction on the momentum equations

The equilibrium balance of moments in the three-dimensional theory is further constrained by the symmetry condition of the Cauchy stress tensor, $\boldsymbol{\sigma} = \boldsymbol{\sigma}^T$. In terms of the convected basis, $\boldsymbol{\sigma} = \sigma^{IJ}\boldsymbol{g}_I \otimes \boldsymbol{g}_J$. The symmetry condition implies $\boldsymbol{g}_I \otimes \boldsymbol{g}_J\sigma^{IJ} = \boldsymbol{g}_I \otimes \boldsymbol{\sigma}\boldsymbol{g}^I$. Integrating this equation through the shell thickness and using the definitions $\boldsymbol{g}_\alpha = \boldsymbol{a}_\alpha + \xi\boldsymbol{t}_{,\alpha}$ and $\boldsymbol{g}_3 = \boldsymbol{t}$ gives

$$\boldsymbol{a}_\alpha \times \int_{h^-}^{h^+} \boldsymbol{\sigma}\boldsymbol{a}^\alpha j d\xi + \boldsymbol{t}_{,\alpha} \times \int_{h^-}^{h^+} \xi\boldsymbol{\sigma}\boldsymbol{a}^\alpha j d\xi + \boldsymbol{t} \times \int_{h^-}^{h^+} \boldsymbol{\sigma}\boldsymbol{g}^3 j d\xi = \mathbf{0}. \tag{2.39}$$

Substituting the stress resultant $\boldsymbol{n}^\alpha$, the through-the-thickness resultant $\boldsymbol{l}$ and $\tilde{\boldsymbol{m}}^\alpha$ from (2.22), (2.26) and (2.24) into (2.39), the symmetry condition implies that

$$\mathbf{a}_\alpha \times \mathbf{n}^\alpha + \mathbf{t}_{,\alpha} \times \widetilde{\mathbf{m}}^\alpha + \mathbf{t} \times \mathbf{l} = \mathbf{0}. \tag{2.40}$$

The above equation places a limitation on the form of the constitutive equations and means that (2.38) can be recast. Firstly, using the definition in (2.25) the first term of (2.38) becomes

$$\frac{1}{\bar{j}}\left(\left(\bar{j}\mathbf{m}^\alpha\right)_{,\alpha} = \boldsymbol{t}_{,\alpha} \times \tilde{\boldsymbol{m}}^\alpha + \boldsymbol{t} \times \frac{1}{\bar{j}}\left(\left(\bar{j}\tilde{\mathbf{m}}^\alpha\right)_{,\alpha}\right.\right. . \tag{2.41}$$

Now, making use of the stipulation that the applied resultant couple $\bar{\mathbf{m}}$ should satisfy

$$\tilde{\bar{\mathbf{m}}} \cdot \boldsymbol{t} = 0 \qquad \longrightarrow \qquad \tilde{\bar{\mathbf{m}}} = \bar{\mathbf{m}} \times \boldsymbol{t},$$

and substituting (2.40) and (2.41) into (2.38), we get

$$\boldsymbol{t} \times \left[\frac{1}{\bar{j}}\left(\left(\bar{j}\tilde{\mathbf{m}}^\alpha\right)_{,\alpha} - \boldsymbol{l} + \tilde{\bar{m}}\right]\right. = \mathbf{0}. \tag{2.42}$$

The final form of the the momentum equations is as follows: from (2.36)

$$\frac{1}{\bar{j}}\left(\bar{j}\mathbf{n}^{\alpha}\right)_{,\alpha}+\bar{\mathbf{n}}=\mathbf{0}, \tag{2.43}$$

and from (2.42)

$$\frac{1}{\bar{j}}\left(\bar{j}\widetilde{\mathbf{m}}^{\alpha}\right)_{,\alpha}-\bar{\mathbf{l}}+\bar{\widetilde{\mathbf{m}}}=\mathbf{0}. \tag{2.44}$$

2.3.4 Component expressions

$\mathbf{n}^{\alpha}$ and $\tilde{\mathbf{m}}^{\alpha}$ can be expressed in terms of components relative to the basis $\{\mathbf{a}_{\alpha},\mathbf{t}\}$ according to

$$\mathbf{n}^{\alpha}=n^{\beta\alpha}\mathbf{a}_{\beta}+q^{\alpha}\mathbf{t}, \tag{2.45}$$

$$\tilde{\mathbf{m}}^{\alpha}=\widetilde{m}^{\beta\alpha}\mathbf{a}_{\beta}+\widetilde{m}^{3\alpha}\mathbf{t}. \tag{2.46}$$

Similarly, the vector $\mathbf{t}_{,\alpha}$ can be resolved relative to the basis $\{\boldsymbol{a}_1,\boldsymbol{a}_2,\boldsymbol{t}\}$ according to

$$\mathbf{t}_{,\alpha}=\lambda_{\alpha}^{\mu}\boldsymbol{a}_{\mu}+\lambda_{\alpha}^{3}\mathbf{t}. \tag{2.47}$$

The scalar λ_{α}^{3} can be determined in terms of λ_{α}^{μ} using the conditions $|\mathbf{t}|=1$ and $\mathbf{t}\cdot\mathbf{t}_{,\alpha}=0$. Taking the scalar product of each term of (2.47) with $\boldsymbol{t}$ yields

$$\lambda_{\alpha}^{3}=-\lambda_{\alpha}^{\mu}\boldsymbol{a}_{\mu}\cdot\mathbf{t}\equiv-\lambda_{\alpha}^{\mu}\gamma_{\mu}. \tag{2.48}$$

Substituting (2.45) – (2.48), into (2.40) then results in

$$\left(n^{\beta\alpha}-\lambda_{\mu}^{\beta}\widetilde{m}^{\alpha\mu}\right)\mathbf{a}_{\beta}\times\mathbf{a}_{\alpha}+\mathbf{t}\times\left[\mathbf{l}-\left(q^{\alpha}+\lambda_{\mu}^{\alpha}\widetilde{m}^{3\mu}-\lambda_{\mu}^{3}\widetilde{m}^{\alpha\mu}\right)\mathbf{a}_{\alpha}\right]=\mathbf{0}. \tag{2.49}$$

After taking the scalar product of (2.49) with $\boldsymbol{t}$ we can then define

$$\widetilde{n}^{\beta\alpha} = n^{\beta\alpha} - \lambda^{\beta}_{\mu}\widetilde{m}^{\alpha\mu}. \tag{2.50}$$

Making use of the new definition

$$\widetilde{q}^{\alpha} = q^{\alpha} - \lambda^{3}_{\mu}\widetilde{m}^{\alpha\mu} \equiv q^{\alpha} + \lambda^{\beta}_{\mu}\gamma_{\beta}\widetilde{m}^{\alpha\mu}, \tag{2.51}$$

we can then obtain an expression for $\boldsymbol{l}$ from (2.49) and (2.50); that is,

$$\mathbf{l} = \lambda\mathbf{t} + \widetilde{q}^{\alpha}\boldsymbol{\varphi}_{,\alpha} + \lambda^{\alpha}_{\mu}\widetilde{m}^{3\mu}\boldsymbol{\varphi}_{,\alpha}. \tag{2.52}$$

Useful later on is the definition

$$\bar{\boldsymbol{l}} = \boldsymbol{l} + \bar{\lambda}\boldsymbol{t}, \tag{2.53}$$

where $\bar{\lambda}$ is a director pressure, of sorts, which can be likened to hydrostatic pressure in incompressible elasticity.

2.4 Strain-displacement relations

The generalised displacement field is given by $\{\mathbf{u}, \Delta\boldsymbol{t}\}$, where $\mathbf{u}$ is the midsurface displacement in $\mathbb{R}^3$ and $\Delta\boldsymbol{t}$ the change in director vector. Relative to the tangent basis, the components are

$$\boldsymbol{u} = \begin{Bmatrix} u^1 \\ u^2 \\ u^3 \end{Bmatrix}, \qquad \Delta\boldsymbol{t} = \begin{Bmatrix} \Delta t^1 \\ \Delta t^2 \\ \Delta t^3 \end{Bmatrix}.$$

We define the tensors

$$a_{\alpha\beta} = \boldsymbol{a}_{\alpha} \cdot \boldsymbol{a}_{\beta}; \qquad a^0_{\alpha\beta} = \boldsymbol{a}^0_{\alpha} \cdot \boldsymbol{a}^0_{\beta} \tag{2.54}$$

$$\gamma_\alpha = \boldsymbol{a}_\alpha \cdot \boldsymbol{t}; \qquad \gamma^0_\alpha = \boldsymbol{a}_{\alpha^0} \cdot \boldsymbol{t}^0 \tag{2.55}$$

$$\kappa_{\alpha\beta} = \boldsymbol{a}_\alpha \cdot \boldsymbol{t}_{,\beta}; \qquad \kappa^0_{\alpha\beta} = \boldsymbol{a}_{\alpha^0} \cdot \boldsymbol{t}^0_{,\beta} \tag{2.56}$$

The relative strain measures are now defined according to the above surface basis tensors as follows

$$\varepsilon_{\alpha\beta} = \frac{1}{2}\left(a_{\alpha\beta} - a^0_{\alpha\beta}\right), \tag{2.57}$$

$$\delta_\alpha = \gamma_\alpha - \gamma^0_\alpha, \tag{2.58}$$

$$\rho_{\alpha\beta} = \frac{1}{2}\left(\kappa_{\alpha\beta} - \kappa^0_{\alpha\beta}\right). \tag{2.59}$$

Here $\varepsilon_{\alpha\beta}$ are components of the membrane strain, δ_α are components of the shear strain and $\rho_{\alpha\beta}$ are components of the bending strain. We begin with the membrane strain. The current position of a point on the shell midsurface is given by

$$\boldsymbol{\varphi} = \boldsymbol{\varphi}^0 + \mathbf{u}, \tag{2.60}$$

and thus

$$\mathbf{a}_\alpha = \mathbf{a}^0_\alpha + \mathbf{u}_{,\alpha}. \tag{2.61}$$

Applying this definition to (2.54) we get

$$\begin{aligned} a_{\alpha\beta} &= \left(\boldsymbol{\varphi}^0 + \mathbf{u}\right)_{,\alpha} \cdot \left(\boldsymbol{\varphi}^0 + \mathbf{u}\right)_{,\beta} \\ &= \mathbf{a}^0_\alpha \cdot \mathbf{a}^0_\beta + \mathbf{a}^0_\alpha \cdot \mathbf{u}_{,\beta} + \mathbf{a}^0_\beta \cdot \mathbf{u}_{,\alpha} + \mathbf{u}_{,\alpha} \cdot \mathbf{u}_{,\beta}. \end{aligned}$$

Since we are interested in the small-strain case, we assume that the term $\mathbf{u}_{,\alpha} \cdot \mathbf{u}_{,\beta}$ is much smaller than $\mathbf{a}^0_{,\beta} \cdot \mathbf{u}_{,\alpha}$ and so we disregard it, leaving the linearised form

$$a_{\alpha\beta} = \mathbf{a}^0_\alpha \cdot \mathbf{a}^0_\beta + \mathbf{a}^0_\alpha \cdot \mathbf{u}_{,\beta} + \mathbf{a}^0_\beta \cdot \mathbf{u}_{,\alpha}.$$

Thus the shell membrane strain from (2.57) becomes

$$\varepsilon_{\alpha\beta} = \tfrac{1}{2}\left(\mathbf{a}^0_\alpha \cdot \mathbf{u}_{,\beta} + \mathbf{a}^0_\beta \cdot \mathbf{u}_{,\alpha}\right). \tag{2.62}$$

Next to be expanded is the shear strain term. The current director can be written as

$$\boldsymbol{t} = \boldsymbol{t}^0 + \Delta\boldsymbol{t},$$

and so (2.55) becomes

$$\begin{aligned}\gamma_\alpha &= \left(\mathbf{a}^0_\alpha + \mathbf{u}_{,\alpha}\right) \cdot \left(\boldsymbol{t}^0 + \Delta\boldsymbol{t}\right) \\ &= \mathbf{a}^0_\alpha \cdot \boldsymbol{t}^0 + \mathbf{a}^0_\alpha \cdot \Delta\boldsymbol{t} + \mathbf{u}_{,\alpha} \cdot \boldsymbol{t}^0 + \mathbf{u}_{,\alpha} \cdot \Delta\boldsymbol{t}.\end{aligned}$$

The small-strain assumption means we may disregard the $\mathbf{u}_{,\alpha} \cdot \Delta\boldsymbol{t}$ term. The shear strain given in (2.58) then becomes

$$\delta_\alpha = \mathbf{a}^0_\alpha \cdot \Delta\boldsymbol{t} + \mathbf{u}_{,\alpha} \cdot \boldsymbol{t}^0. \tag{2.63}$$

In a similar fashion as above the remaining bending strain (2.59) can be shown to be given by

$$\rho_{\alpha\beta} = \frac{1}{2}\left(\mathbf{a}^0_\alpha \cdot \Delta\boldsymbol{t}_{,\beta} + \mathbf{a}^0_\beta \cdot \Delta\boldsymbol{t}_{,\alpha} + \mathbf{u}_{,\alpha} \cdot \boldsymbol{t}^0_{,\beta} + \mathbf{u}_{,\beta} \cdot \boldsymbol{t}^0_{,\alpha}\right). \tag{2.64}$$

2.5 Elastic constitutive relations

Later on in this chapter the stress-strain relations for elastic transversely isotropic materials will be introduced. Here we set out the constitutive relations for isotropic elastic shells.

We are concerned with relating the membrane stress, shear stress and stress couple resultants to their respective strains. We begin this process by noting that the stress resultant $\boldsymbol{n}^{\alpha}$ and stress couple $\boldsymbol{m}^{\alpha}$ for the shell midsurface are defined through the Cauchy stress $\boldsymbol{\sigma}$ in (2.22) and (2.23).

Hooke's law [20] for an anisotropic elastic material is given by

$$\sigma^{ij} = C^{ijkl}\varepsilon_{kl}. \tag{2.65}$$

It is the components of the elastic tensor $\boldsymbol{C}$ that concern us. For isotropic materials (2.65) becomes

$$\boldsymbol{\sigma} = \frac{E}{1+\nu}\left[\boldsymbol{\varepsilon} + \frac{\nu}{1-2\nu}\left(\operatorname{tr}\boldsymbol{\varepsilon}\right)\boldsymbol{I}\right], \tag{2.66}$$

where E is Young's modulus and ν is the Poisson ratio.

Due to the assumption of no thickness change from the reference to the deformed configuration, we may impose $\varepsilon^{33} = 0$. Taking this into account, we now substitute the Cauchy stress definition from (2.66) into the shell stress relations from (2.22) and (2.23). After simplifying appropriately and making use of the component expressions listed in (2.45) - (2.51), the following constitutive relations for $\widetilde{n}^{\alpha\beta}$, $\widetilde{q}^{\alpha}$ and $\widetilde{m}^{\alpha\beta}$, can be derived:

$$\begin{Bmatrix} \widetilde{n}^{11} \\ \widetilde{n}^{22} \\ \widetilde{n}^{12} \end{Bmatrix} = \frac{Eh}{1-\nu^2}\boldsymbol{H}\begin{Bmatrix} \varepsilon_{11} \\ \varepsilon_{22} \\ 2\varepsilon_{12} \end{Bmatrix}, \tag{2.67}$$

$$\begin{Bmatrix} \widetilde{q}^{1} \\ \widetilde{q}^{2} \end{Bmatrix} = \kappa G h \bar{\boldsymbol{H}}\begin{Bmatrix} \gamma_{11} \\ \gamma_{22} \end{Bmatrix}, \tag{2.68}$$

and

$$\begin{Bmatrix} \widetilde{m}^{11} \\ \widetilde{m}^{22} \\ \widetilde{m}^{12} \end{Bmatrix} = \frac{Eh^3}{1-\nu^2}\boldsymbol{H} \begin{Bmatrix} \rho_{11} \\ \rho_{22} \\ 2\rho_{12} \end{Bmatrix}, \tag{2.69}$$

where

$$G = \frac{E}{2\,(1+\nu)}, \tag{2.70}$$

is the shear modulus, κ is the shear correction factor,

$$\bar{\boldsymbol{H}} = \begin{bmatrix} a^{11}\ a^{12} \\ a^{12}\ a^{22} \end{bmatrix},$$

where, from the inverse of tensor (2.54), $a^{\alpha\beta} = (a_{\alpha\beta})^{-1}$, and

$$\boldsymbol{H} = \begin{bmatrix} a^{11}a^{11} & \nu a^{11}a^{22} + (1-\nu)\,\nu a^{12}a^{12} & a^{11}a^{12} \\ \nu a^{11}a^{22} + (1-\nu)\,\nu a^{12}a^{12} & a^{22}a^{22} & a^{22}a^{12} \\ a^{11}a^{12} & a^{22}a^{12} & \dfrac{1-\nu}{2}a^{11}a^{22} + \dfrac{1+\nu}{2}a^{12}a^{12} \end{bmatrix}.$$

For convenience we will define the constitutive matrices

$$\mathbf{D}_m = \frac{Eh}{1-\nu^2}\mathbf{H}, \qquad \mathbf{D}_s = \kappa G h \bar{\boldsymbol{H}}, \qquad \mathbf{D}_b = \frac{Eh^3}{1-\nu^2}\mathbf{H}. \tag{2.71}$$

2.6 Transverse isotropy

An important consideration in the modelling of biological materials is that of accounting for directional properties as a result of fibres embedded in the materials. These fibres affect how the loading within the material is distributed and so must be

taken into account if an accurate biological model is to be constructed. It is therefore necessary to modify the isotropic constitutive relation to take account of this feature, which is known as transverse isotropy.

Figure 2.8 illustrates a section of a cylinder with two helical families of fibres which are orientated at the same angle positively and negatively from the z-axis. This is an important illustration since arteries contain helical families of fibres. The approach to include the effects of transverse isotropy follows that in Schulze–Bauer et al. [28], specialised here to the case of shells and small strains.

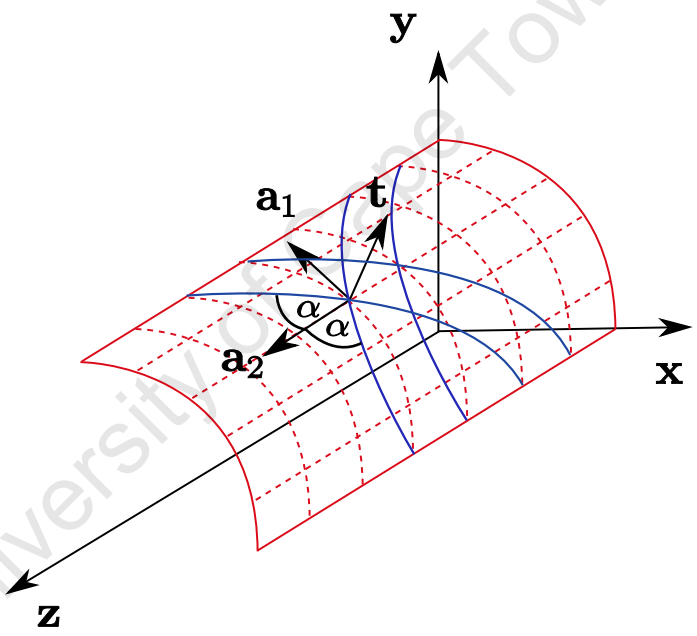

Fig. 2.8. The quarter cylinder showing two fibre families having the same angle positively and negatively from the axis of the cylinder

As indicated in Figure 2.8, the orientation of the fibres with respect to the surface basis $\boldsymbol{a}_1$ and $\boldsymbol{a}_2$ is given by the vector

$$\boldsymbol{N} = \cos\alpha\ \boldsymbol{a}_2 \pm \sin\alpha\ \boldsymbol{a}_1. \tag{2.72}$$

When including transverse isotropy we can decompose the stress in the form

$$\boldsymbol{\sigma} = \underbrace{\boldsymbol{\sigma}_o}_{\text{isotropic part}} + \underbrace{\boldsymbol{\sigma}_f}_{\text{fibre part}}, \tag{2.73}$$

where the isotropic part of the stress $\boldsymbol{\sigma}_0$ is given for hyperelasticity by

$$\boldsymbol{\sigma}_o = K\,(J-1)\,\boldsymbol{I} + G\,\mathrm{dev}\,\bar{\boldsymbol{b}}, \tag{2.74}$$

where $\mathrm{dev}\,\bar{\boldsymbol{b}} = \bar{\boldsymbol{b}} - \frac{1}{3}\left(\mathrm{tr}\,\bar{\boldsymbol{b}}\right)$, is the deviatoric part of $\bar{\boldsymbol{b}}$.

The bulk modulus K and shear modulus G are given by

$$K = \frac{E}{3\,(1-2\nu)}; \qquad G = \frac{E}{2\,(1+\nu)}, \tag{2.75}$$

and the left Cauchy-Green tensor is defined by

$$\bar{\boldsymbol{b}} = \bar{\boldsymbol{F}}\bar{\boldsymbol{F}}^T,$$

where

$$\boldsymbol{F} = J^{\frac{1}{3}}\bar{\boldsymbol{F}} = \boldsymbol{I} + \nabla\boldsymbol{u}$$

is the deformation gradient. Linearising, we obtain

$$J \approx 1 + \mathrm{div}\,\boldsymbol{u} = 1 + \mathrm{tr}\,\boldsymbol{\varepsilon}$$

and

$$\begin{aligned}\bar{\boldsymbol{b}} \approx \boldsymbol{b} &= (\boldsymbol{I} + \nabla \boldsymbol{u})\left(\boldsymbol{I} + \nabla \boldsymbol{u}^T\right) \\ &\approx \boldsymbol{I} + \nabla \boldsymbol{u} + \nabla \boldsymbol{u}^T \\ &= \boldsymbol{I} + 2\boldsymbol{\varepsilon}.\end{aligned}$$

Thus the isotropic stress is given by

$$\boldsymbol{\sigma}_o = K\,(\operatorname{tr}\boldsymbol{\varepsilon})\,\boldsymbol{I} + 2G\operatorname{dev}\boldsymbol{\varepsilon}. \tag{2.76}$$

The fibre part of the stress is given in [28] by

$$\boldsymbol{\sigma}_f = 2k_1\,(I_4 - 1)\,e^{k_2(I_4-1)^2}\operatorname{dev}\boldsymbol{N}\otimes\boldsymbol{N} \tag{2.77}$$

$$\approx 2k_1\,(I_4 - 1)\operatorname{dev}\boldsymbol{N}\otimes\boldsymbol{N}, \tag{2.78}$$

for finite strains, where k_1 and k_2 are material constants and

$$I_4 = \boldsymbol{C}\colon \boldsymbol{N}\otimes\boldsymbol{N} \tag{2.79}$$

is an invariant. Here $\boldsymbol{C} = \boldsymbol{F}^T\boldsymbol{F}$ is the right Cauchy-Green tensor and : denotes the contraction between two second order tensors (written in index notation as $\boldsymbol{A}\colon\boldsymbol{B} = A_{ij}B_{ij}$).

For small strains

$$e^{k_2(I_4-1)^2} \approx 1. \tag{2.80}$$

Furthermore,

$$
\begin{aligned}
I_4 &= \boldsymbol{F}^T\boldsymbol{F}\colon \boldsymbol{N}\otimes\boldsymbol{N} \\
&= \left(\boldsymbol{I}+\nabla\boldsymbol{u}^T\right)\left(\boldsymbol{I}+\nabla\boldsymbol{u}\right) : \boldsymbol{N}\otimes\boldsymbol{N} \\
&\approx \left(\boldsymbol{I}+\nabla\boldsymbol{u}+\nabla\boldsymbol{u}^T\right) : \boldsymbol{N}\otimes\boldsymbol{N} \\
&= 1+2\boldsymbol{\varepsilon}\colon \boldsymbol{N}\otimes\boldsymbol{N} \\
&= 1+2\boldsymbol{N}\otimes\boldsymbol{\varepsilon}\boldsymbol{N}, \\
&= 1+2\boldsymbol{N}\cdot\boldsymbol{\varepsilon}\boldsymbol{N}. \qquad (2.81)
\end{aligned}
$$

Thus $\frac{1}{2}\left(I_4-1\right)$ gives the strain in the fibre direction $\boldsymbol{N}$.

Finally, we can write

$$
\begin{aligned}
\operatorname{dev}\left(\boldsymbol{N}\otimes\boldsymbol{N}\right) &= \boldsymbol{N}\otimes\boldsymbol{N}-\tfrac{1}{3}\left(\operatorname{tr}\left(\boldsymbol{N}\otimes\boldsymbol{N}\right)\right)\boldsymbol{I} \\
&= \boldsymbol{N}\otimes\boldsymbol{N}-\tfrac{1}{3}\boldsymbol{I},
\end{aligned}
$$

leaving us with the expression for the stress in the fibres in the form

$$
\boldsymbol{\sigma}_f = 4k_1\left(\boldsymbol{\varepsilon}\colon \boldsymbol{N}\otimes\boldsymbol{N}\right)\left(\boldsymbol{N}\otimes\boldsymbol{N}-\tfrac{1}{3}\boldsymbol{I}\right). \qquad (2.82)
$$

This stress-strain relation means that for every family of fibres there is an extra $\mathbf{D}_{\text{fib}}$ matrix that must be added onto the $\mathbf{D}_m$ matrix, as previously defined in (2.67) and (2.71).

From (2.72) and (2.82),

$$
\begin{aligned}
\boldsymbol{\varepsilon}\colon \boldsymbol{N}\otimes\boldsymbol{N} &= \varepsilon_{\alpha\beta}N^\alpha N^\beta \qquad (2.83) \\
&= \underbrace{\begin{bmatrix}\sin^2\alpha & \cos^2\alpha & \pm\sin\alpha\cos\alpha\end{bmatrix}}_{\mathbf{w}_{1\times 3}}\bar{\boldsymbol{\varepsilon}}, \qquad (2.84)
\end{aligned}
$$

so that the contribution to the stress from the fibres is

$$\begin{aligned}\tilde{\boldsymbol{n}}_{\text{fib}}^{\beta\alpha} &\approx \frac{1}{\bar{j}} \int_{h-}^{h+} \boldsymbol{\sigma}_{\text{fib}}^{\beta\alpha} j d\xi \\ &\approx 4hk_1 \mathbf{W} \bar{\boldsymbol{\varepsilon}} \left(N^\alpha N^\beta - \tfrac{1}{3}\delta_\beta^\alpha \right),\end{aligned}$$

which can be expressed as

$$\begin{bmatrix} \tilde{n}^{11} \\ \tilde{n}^{22} \\ \tilde{n}^{12} \end{bmatrix} = 4k_1 h \begin{bmatrix} \mathbf{W}\left[(N^1)^2 - \frac{1}{3}\right] \\ \mathbf{W}\left[(N^2)^2 - \frac{1}{3}\right] \\ \mathbf{W} N^1 N^2 \end{bmatrix}_{3\times 3} \begin{bmatrix} \varepsilon_{11} \\ \varepsilon_{22} \\ 2\varepsilon_{12} \end{bmatrix} \tag{2.85}$$

where

$$\mathbf{D}_{\text{fib}} = 4k_1 h \begin{bmatrix} \mathbf{W}\left[(N^1)^2 - \frac{1}{3}\right] \\ \mathbf{W}\left[(N^2)^2 - \frac{1}{3}\right] \\ \mathbf{W} N^1 N^2 \end{bmatrix}. \tag{2.86}$$

3

Weak Formulation and Finite Element Approximation

The finite element method is a method for solving systems of partial differential equations approximately. It takes the form of a system of algebraic equations which can then be solved on a computer. A detailed exposition of the finite element method can be found in [15] and [23].

The first step in the method entails formulating the partial differential equations (PDE) in an integral form, known as the weak form [15]. This is done by multiplying the governing equations by an arbitrary function, known as a test function, integrating over the domain, integrating by parts where appropriate, and imposing the boundary conditions.

Two classes of functions need to be characterised to define the weak form. These are the set of test or weighting functions $\mathcal{V}$ and the set of trial solutions $\mathcal{U}$ [23]. The solution of the system comes from $\mathcal{U}$, while the members of $\mathcal{V}$ 'test' the PDE. The set of trial, or candidate solutions is required to satisfy the Dirichlet boundary conditions of the system.

The finite element method involves setting up discrete approximations of $\mathcal{U}$ and $\mathcal{V}$, which are typically continuous, piecewise polynomials. Thus $\mathcal{U}$ and $\mathcal{V}$ are approximated by convenient, finite-dimensional collections of functions [23]. Within this context the variational equations are then solved.

The chapter will begin with setting out this weak form of the shell equilibrium equations presented in the previous chapter. Following this, the finite element approximation is constructed. The chapter concludes with the construction of the matrix system, which will then be in the correct form to be solved.

3.1 The first equilibrium equation

Starting with the first equilibrium equation, (2.43), we take the scalar product of each side with a test function $\boldsymbol{v}$ and integrate over the domain $\mathcal{A}$. This gives

$$\int_A \left[\frac{1}{\bar{j}}\left(\left(\bar{j}\mathbf{n}^\alpha\right)_{,\alpha} + \bar{\mathbf{n}}\right]\right] \cdot \boldsymbol{v}\ dA = 0, \tag{3.1}$$

where $dA = \bar{j}d\xi^1 d\xi^2$. We perform integration by parts on the first term to obtain

$$\int_A \frac{1}{\bar{j}}\left(\bar{j}\mathbf{n}^\alpha\right)_{,\alpha} \cdot \boldsymbol{v}\ dA = \oint_{\partial A} \bar{j}\mathbf{n}^\alpha \frac{1}{\bar{j}} \cdot \boldsymbol{v} p_\alpha\ dS - \int_A \bar{j}\mathbf{n}^\alpha \cdot \left(\boldsymbol{v}\frac{1}{\bar{j}}\right)_{,\alpha}\ dA,$$

where $\boldsymbol{p} = p_\alpha \boldsymbol{a}^\alpha$ is the outward normal to the shell boundary.

Substituting in (3.1) we get

$$\int_A \left[-\mathbf{n}^\alpha \cdot \boldsymbol{v}_{,\alpha} - \mathbf{n}^\alpha \cdot \boldsymbol{v}\frac{1}{\bar{j}}\bar{j}_{,\alpha} + \bar{\mathbf{n}} \cdot \boldsymbol{v}\right]\ dA + \oint_{\partial A} \mathbf{n}^\alpha \cdot \boldsymbol{v} p_\alpha\ dS = 0. \tag{3.2}$$

We now work with the first term of (3.2), since the rest of the terms fall into the category of external loading and boundary conditions and will ultimately make up part of the right-hand side of the formulation to be solved. Using the definitions laid out in equations (2.45), (2.50) and (2.51) from the previous chapter, this first term becomes

$$\mathbf{n}^{\alpha}\cdot\boldsymbol{v}_{,\alpha}=\left(n^{\beta\alpha}\mathbf{a}_{\beta}+q^{\alpha}\mathbf{t}\right)\cdot\boldsymbol{v}_{,\alpha}$$

$$=\left(\widetilde{n}^{\beta\alpha}+\lambda^{\beta}_{\mu}\widetilde{m}^{\alpha\mu}\right)\mathbf{a}_{\beta}\cdot\boldsymbol{v}_{,\alpha}+\left(\widetilde{q}^{\alpha}+\lambda^{3}_{\mu}\widetilde{m}^{\alpha\mu}\right)\mathbf{t}\cdot\boldsymbol{v}_{,\alpha}.$$

Recalling the relation $\mathbf{t}_{,\alpha}=\lambda^{\mu}_{\alpha}\boldsymbol{a}_{\mu}+\lambda^{3}_{\alpha}\mathbf{t}$ from (2.47), the above expansion can be regrouped. It now becomes appropriate to define the matrices

$$\mathbb{B}_{m}=\begin{bmatrix}\mathbf{a}_{1}^{T}\dfrac{\partial}{\partial\xi^{1}}\\ \mathbf{a}_{2}^{T}\dfrac{\partial}{\partial\xi^{2}}\\ \mathbf{a}_{1}^{T}\dfrac{\partial}{\partial\xi^{2}}+\mathbf{a}_{2}^{T}\dfrac{\partial}{\partial\xi^{1}}\end{bmatrix}_{3\times3},$$

$$\mathbb{B}_{sm}=\begin{bmatrix}\mathbf{t}^{T}\dfrac{\partial}{\partial\xi^{1}}\\ \mathbf{t}^{T}\dfrac{\partial}{\partial\xi^{2}}\end{bmatrix}_{2\times3},$$

$$\mathbb{B}_{bm}=\begin{bmatrix}\mathbf{t}_{,1}^{T}\dfrac{\partial}{\partial\xi^{1}}\\ \mathbf{t}_{,2}^{T}\dfrac{\partial}{\partial\xi^{2}}\\ \mathbf{t}_{,1}^{T}\dfrac{\partial}{\partial\xi^{2}}+\mathbf{t}_{,2}^{T}\dfrac{\partial}{\partial\xi^{1}}\end{bmatrix}_{3\times3}.$$

Finally, making use of the definitions

$$\widetilde{\mathbf{N}}=\begin{bmatrix}\widetilde{n}^{11}\ \widetilde{n}^{22}\ \widetilde{n}^{12}\end{bmatrix}^{T},$$

$$\widetilde{\mathbf{Q}}=\begin{bmatrix}\widetilde{q}^{1}\ \widetilde{q}^{2}\end{bmatrix}^{T},$$

$$\widetilde{\mathbf{M}} = \left[\widetilde{m}^{11}\ \widetilde{m}^{22}\ \widetilde{m}^{12}\right]^T,$$

where $\widetilde{\boldsymbol{N}}$ is the effective membrane resultant force, $\widetilde{\boldsymbol{Q}}$ the effective shear resultant force and $\widetilde{\boldsymbol{M}}$ the effective resultant couple, the weak form of the first equilibrium equation can be written in matrix form as

$$\int_A \left([\mathbb{B}_m \boldsymbol{v}]^T \widetilde{\boldsymbol{N}} + [\mathbb{B}_{sm} \boldsymbol{v}]^T \widetilde{\boldsymbol{Q}} + [\mathbb{B}_{bm} \boldsymbol{v}]^T \widetilde{\boldsymbol{M}}\right) \bar{j}\ dA = \int_A \bar{\mathbf{n}} \cdot \boldsymbol{v} dA + \oint_{\partial A} \mathbf{n}^\alpha \cdot \boldsymbol{v} p_\alpha\ dS. \quad (3.3)$$

3.2 The second equilibrium equation

A similar approach is taken with the second equilibrium equation, (2.44). We take the scalar product of each side of this equation with a test function $\boldsymbol{k}$ and integrate over the domain $\mathcal{A}$ to get

$$\int_A \left[\frac{1}{\bar{j}} \left(\left(\bar{j} \widetilde{\mathbf{m}}^\alpha\right)_{,\alpha} - \bar{\mathbf{l}} + \bar{\widetilde{\mathbf{m}}}\right] \cdot \boldsymbol{k}\ dA = 0. \quad (3.4)$$

The test function $\boldsymbol{k}$ is chosen such that

$$\boldsymbol{t} \cdot \boldsymbol{k} = 0, \quad (3.5)$$

and thus

$$(\boldsymbol{t} \cdot \boldsymbol{k})_{,\alpha} = 0, \quad (3.6)$$

so that

$$\boldsymbol{t} \cdot \boldsymbol{k}_{,\alpha} = -\boldsymbol{t}_{,\alpha} \cdot \boldsymbol{k}. \quad (3.7)$$

Integration by parts of the first term of (3.4) yields

$$\int_A \frac{1}{\bar{j}} \left(\bar{j}\widetilde{\boldsymbol{m}}^\alpha\right)_{,\alpha} \cdot \boldsymbol{k}\ dA = \oint_{\partial A} \widetilde{\boldsymbol{m}}^\alpha \cdot \boldsymbol{k}\bar{p}_\alpha\ dS - \int_A \bar{j}\widetilde{\boldsymbol{m}}^\alpha \left(\frac{1}{\bar{j}}\boldsymbol{k}\right)_{,\alpha}\ dA.$$

After some rearranging, (3.4) then becomes

$$\int_A \left(-\widetilde{\boldsymbol{m}}^\alpha \cdot \boldsymbol{k}_{,\alpha} - \bar{j}_{,\alpha}\frac{\widetilde{\boldsymbol{m}}^\alpha}{\bar{j}} \cdot \boldsymbol{k} - \bar{\boldsymbol{l}} \cdot \boldsymbol{k} + \widetilde{\boldsymbol{m}} \cdot \boldsymbol{k}\right)\ dA + \oint_{dA} \widetilde{\boldsymbol{m}}^\alpha \cdot \boldsymbol{k}\bar{p}_\alpha\ dS = 0.$$

Again, dealing only with the parts of the equation which will form part of the left-hand side of the formulation to be solved, we obtain

$$LHS = \int_A \left(-\widetilde{\boldsymbol{m}}^\alpha \cdot \boldsymbol{k}_{,\alpha} + \bar{\boldsymbol{l}} \cdot \boldsymbol{k}\right)\ dA. \tag{3.8}$$

Using the definition from (3.7) of the restriction on $\boldsymbol{k}$ as well as (2.47), the first term of (3.8) becomes

$$\begin{aligned}
\widetilde{\boldsymbol{m}}^\alpha \cdot \boldsymbol{k}_{,\alpha} &= \left(\widetilde{m}^{\beta\alpha}\mathbf{a}_\beta + \widetilde{m}^{3\alpha}\boldsymbol{t}\right) \cdot \boldsymbol{k}_{,\alpha} \\
&= \widetilde{m}^{\beta\alpha}\mathbf{a}_\beta \cdot \boldsymbol{k}_{,\alpha} - \widetilde{m}^{3\alpha}\boldsymbol{t}_{,\alpha} \cdot \boldsymbol{k} \\
&= \widetilde{m}^{\beta\alpha}\mathbf{a}_\beta \cdot \boldsymbol{k}_{,\alpha} - \widetilde{m}^{3\alpha}\left(\lambda^\beta_\alpha\mathbf{a}_\beta + \lambda^3_\alpha\boldsymbol{t}\right) \cdot \boldsymbol{k} \\
&= \widetilde{m}^{\beta\alpha}\mathbf{a}_\beta \cdot \boldsymbol{k}_{,\alpha} - \widetilde{m}^{3\alpha}\lambda^\beta_\alpha\mathbf{a}_\beta \cdot \boldsymbol{k}.
\end{aligned} \tag{3.9}$$

Again, making use of the restriction of $\boldsymbol{k}$ in (3.5), and previous definitions for $\boldsymbol{l}$ and $\bar{\boldsymbol{l}}$ in (2.52) and (2.53), the second term of (3.8) becomes

$$\begin{aligned}
\bar{\boldsymbol{l}} \cdot \boldsymbol{k} &= \left(\bar{\lambda}\boldsymbol{t} + \lambda\boldsymbol{t} + \widetilde{q}^\alpha\boldsymbol{a}_\alpha + \lambda^\alpha_\mu\widetilde{m}^{3\mu}\boldsymbol{a}_\alpha\right) \cdot \boldsymbol{k} \\
&= 0 + 0 + \widetilde{q}^\alpha\boldsymbol{a}_\alpha \cdot \boldsymbol{k} + \lambda^\alpha_\mu\widetilde{m}^{3\mu}\boldsymbol{a}_\alpha \cdot \boldsymbol{k}.
\end{aligned} \tag{3.10}$$

Combining the results of (3.9) and (3.10) the left-hand side of the second equilibrium equation becomes

$$LHS = \int_A \left(\widetilde{m}^{\beta\alpha} \mathbf{a}_\beta \cdot \boldsymbol{k}_{,\alpha} + \widetilde{q}^{\alpha} \mathbf{a}_\alpha \cdot \boldsymbol{k} \right) \, dA. \tag{3.11}$$

The following matrices can now be defined:

$$\mathbb{B}_{bb} = \begin{bmatrix} \mathbf{a}_1^T \dfrac{\partial}{\partial \xi^1} \\ \mathbf{a}_2^T \dfrac{\partial}{\partial \xi^2} \\ \mathbf{a}_1^T \dfrac{\partial}{\partial \xi^2} + \mathbf{a}_2^T \dfrac{\partial}{\partial \xi^1} \end{bmatrix}_{3\times 3} \qquad \bar{\boldsymbol{\Lambda}}_{3\times 2} = \mathbb{B}_m \bar{\boldsymbol{\Lambda}},$$

$$\mathbb{B}_{sb} = \begin{bmatrix} \mathbf{a}_1 \\ \mathbf{a}_2 \end{bmatrix}_{2\times 3} \bar{\boldsymbol{\Lambda}}_{3\times 2},$$

where $\bar{\boldsymbol{\Lambda}}$ is as defined in (2.18) and will bring about the necessary conversion in the formulation from $\{\Delta \boldsymbol{t}\}_{3\times 1}$ to $\{\Delta \boldsymbol{T}\}_{2\times 1}$.

Using the above matrices as well as the previously stated definitions for $\widetilde{\boldsymbol{M}}$ and $\widetilde{\boldsymbol{Q}}$, the second equilibrium equation becomes

$$\int_A \left(\left[\mathbb{B}_{bb} \boldsymbol{k} \right]^T \widetilde{\boldsymbol{M}} + \left[\mathbb{B}_{sb} \boldsymbol{k} \right]^T \widetilde{\boldsymbol{Q}} \right) \bar{j} \, dA = \int_A \bar{\widetilde{\boldsymbol{m}}} \cdot \boldsymbol{k} dA + \oint_{\partial A} \widetilde{\boldsymbol{m}}^{\alpha} \cdot \boldsymbol{k} \bar{p}_\alpha \, dS. \tag{3.12}$$

3.3 The final form

Combining the weak form descriptions for the first and second equilibrium equations, we obtain

$$\int_A \left([\mathbb{B}_m \boldsymbol{v}]^T \widetilde{\boldsymbol{N}} + [\mathbb{B}_{sm}\boldsymbol{v} + \mathbb{B}_{sb}\boldsymbol{k}]^T \widetilde{\boldsymbol{Q}} + [\mathbb{B}_{bm}\boldsymbol{v} + \mathbb{B}_{bb}\boldsymbol{k}]^T \widetilde{\boldsymbol{M}} \right) \, dA$$
$$= \int_A \left(\bar{\mathbf{n}} \cdot \boldsymbol{v} + \bar{\widetilde{\boldsymbol{m}}} \cdot \boldsymbol{k} \right) dA + \oint_{\partial A} \left(\mathbf{n}^\alpha \cdot \boldsymbol{v} p_\alpha + \widetilde{\boldsymbol{m}}^\alpha \cdot \boldsymbol{k} \bar{p}_\alpha \right) \, dS. \quad (3.13)$$

It is now necessary to bring in the constitutive relations that were defined in the previous chapter. Using the definitions of the $\mathbb{B}$ matrices, the various strain measures from (2.62), (2.63) and (2.64) can be expressed in the form

$$\boldsymbol{\varepsilon} = \mathbb{B}_m \boldsymbol{u}, \quad (3.14)$$

$$\boldsymbol{\gamma} = \left[\mathbb{B}_{sm} \, \mathbb{B}_{sb} \right] \left\{ \begin{array}{c} \boldsymbol{u} \\ \boldsymbol{\Delta T} \end{array} \right\}, \quad (3.15)$$

$$\boldsymbol{\rho} = \left[\mathbb{B}_{bm} \, \mathbb{B}_{bb} \right] \left\{ \begin{array}{c} \boldsymbol{u} \\ \boldsymbol{\Delta T} \end{array} \right\}, \quad (3.16)$$

where

$$\boldsymbol{u} = \left\{ \begin{array}{c} u^1 \\ u^2 \\ u^3 \end{array} \right\}, \quad (3.17)$$

and

$$\boldsymbol{\Delta T} = \left\{ \begin{array}{c} \Delta T^1 \\ \Delta T^2 \end{array} \right\} \quad (3.18)$$

are the vectors of displacement and change in director.

Using the stress-strain relations and definitions obtained in (2.67), (2.68), (2.69), (2.71) and (3.14), the left-hand side of the combined weak form in (3.13) becomes

$$LHS = \int_A \left([\mathbb{B}_m \boldsymbol{v}]^T \mathbf{D_m} [\mathbb{B}_m \mathbf{u}] + [\mathbb{B}_{sm}\boldsymbol{v} + \mathbb{B}_{sb}\boldsymbol{k}]^T \mathbf{D_s} [\mathbb{B}_{sm}\boldsymbol{u} + \mathbb{B}_{sb}\boldsymbol{\Delta T}] \right) \bar{j} d\xi^1 d\xi^2$$
$$+ \left([\mathbb{B}_{bm}\boldsymbol{v} + \mathbb{B}_{bb}\boldsymbol{k}]^T \mathbf{D_b} [\mathbb{B}_{bm}\boldsymbol{u} + \mathbb{B}_{bb}\boldsymbol{\Delta T}] \right) \bar{j} d\xi^1 d\xi^2. \quad (3.19)$$

3.4 Finite element interpolations

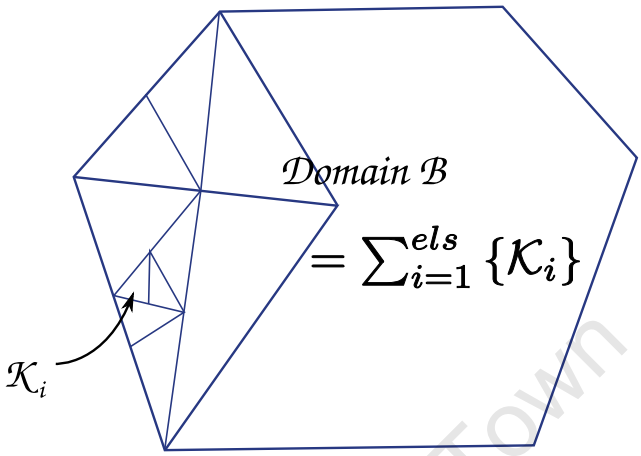

Fig. 3.1. Illustration of the subdivision of a domain into simple subdomains

The first step in the finite element method involves partitioning the domain into subdomains. These subdomains, or elements, take the form of simple shapes like quadrilaterals or triangles, so that collectively they cover, perhaps approximately, the original domain. Figure 3.1 above illustrates this concept. The collection of the integrals over the elements then replace the integral over the whole domain.

It is required that the elements making up a domain do not leave gaps, do not overlap, and that the corners are coincident.

The reference configuration of the shell surface in $\mathbb{R}^3$ is generated by maps from a reference element which, as shown in Figure 3.2, is the standard biunit square $(-1\,,1) \times (-1\,,1)$ [30]. The approximations to the shell midsurface position $\boldsymbol{\varphi}_e^h$ and unit director vector $\boldsymbol{t}_e^h$, for element e, are given by

$$\boldsymbol{\varphi}_e^h = \sum_{A=1}^{4} N^A\,(\xi,\eta)\,\boldsymbol{\varphi}_A^0 \tag{3.20}$$

and

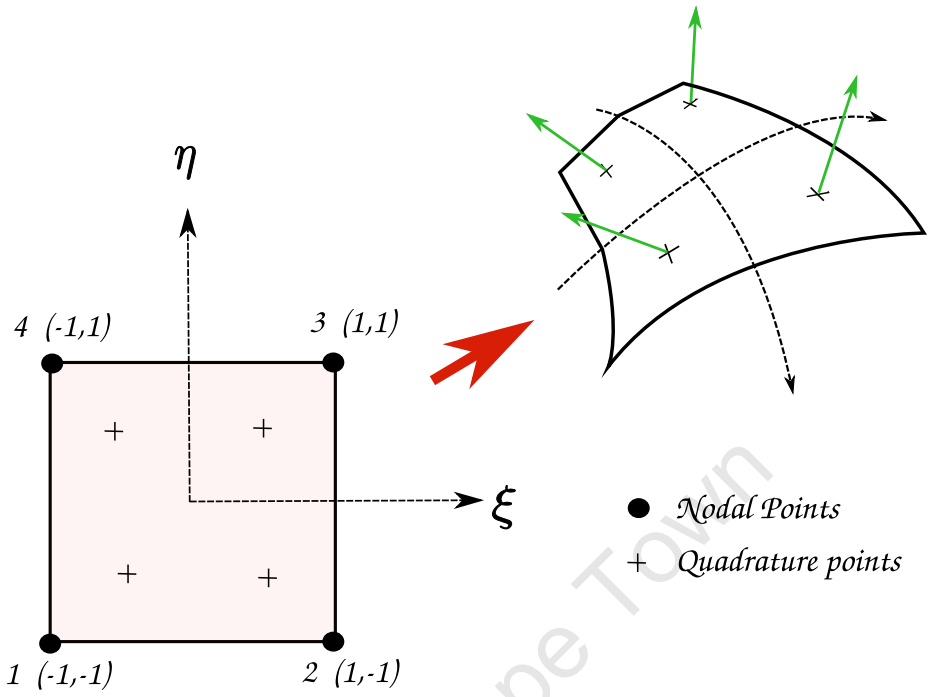

Fig. 3.2. Mapping of the shell element from the isoparametric biunit square

$$\boldsymbol{t}_e^h = \frac{\tilde{\boldsymbol{t}}^h}{\| \tilde{\boldsymbol{t}}^h \|}, \tag{3.21}$$

where

$$\tilde{\boldsymbol{t}}^h = \sum_{A=1}^{4} N^A \boldsymbol{t}_A^0 \tag{3.22}$$

and $\boldsymbol{\varphi}_A^0$ and $\boldsymbol{t}_A^0$ are in $\mathbb{R}^3$, with $A = 1, ..., 4$. The isoparametric bilinear shape functions $N^A(\xi, \eta)$ are given by

$$N^A(\xi, \eta) = \tfrac{1}{4}[1 + \xi\xi_A][1 + \eta\eta_A], \qquad A = 1, ..., 4, \tag{3.23}$$

where $(\xi_A, \eta_A) \in \{(-1, -1); (1, -1); (1, 1); (-1, 1)\}$. The director interpolation scheme ensures that $\boldsymbol{t}_e^h$ is a unit vector. Here and henceforth we write (ξ, η) for (ξ^1, ξ^2) where appropriate.

We adopt the same interpolation scheme for the test functions utilised in the weak form; that is, on an arbitrary element e,

$$\boldsymbol{v}_e^h = \sum_{A=1}^{4} N^A(\xi,\eta)\,\boldsymbol{v}_A, \tag{3.24}$$

$$\boldsymbol{k}_e^h = \sum_{A=1}^{4} N^A(\xi,\eta)\,\boldsymbol{k}_A. \tag{3.25}$$

Necessary for the implementation phase are the finite element interpolations of the surface convected basis $\boldsymbol{a}_\alpha$ as well as the director derivatives $\boldsymbol{t}_{,\alpha}$. For the case of $\boldsymbol{a}_\alpha$ we simply use the gradient of the shape functions with respect to ξ and η, so that

$$\boldsymbol{a}_{e\,\alpha}^h = \sum_{A=1}^{4} N_{,\alpha}^A(\xi,\eta)\,\boldsymbol{\varphi}_A^0 \tag{3.26}$$

However, in the case of the approximation $\boldsymbol{t}_{e\,,\alpha}^h$, obtaining the derivative is more complex as a result of having to differentiate the unit vector (3.21). We have

$$\begin{aligned}
\boldsymbol{t}_{e\,,\alpha}^h &= \frac{\partial}{\partial\xi^\alpha}\left[\frac{\sum_{A=1}^4 N^A\boldsymbol{t}_A^0}{\parallel\sum_{A=1}^4 N^A\boldsymbol{t}_A^0\parallel}\right] \\
&= \frac{1}{\parallel\sum_{A=1}^4 N^A\boldsymbol{t}_A^0\parallel}\sum_{A=1}^{4} N_{,\alpha}^A\boldsymbol{t}_A^0 \;-\; \frac{\sum_{A=1}^4 N^A\boldsymbol{t}_A^0}{\left(\parallel\sum_{A=1}^4 N^A\boldsymbol{t}_A^0\parallel\right)^2}\,\frac{\partial}{\partial\xi^\alpha}\parallel\sum_{A=1}^{4} N^A\boldsymbol{t}_A^0\parallel \\
&= \frac{\tilde{\boldsymbol{t}}_{,\alpha}^h}{\parallel\tilde{\boldsymbol{t}}^h\parallel} \;-\; \frac{\boldsymbol{t}_e^h}{\parallel\tilde{\boldsymbol{t}}^h\parallel}\left(\boldsymbol{t}_e^h\cdot\tilde{\boldsymbol{t}}_{,\alpha}^h\right) \\
&= \frac{1}{\parallel\tilde{\boldsymbol{t}}^h\parallel}\left[\boldsymbol{I}-\boldsymbol{t}_e^h\otimes\boldsymbol{t}_e^h\right]\tilde{\boldsymbol{t}}_{,\alpha}^h \qquad ,
\end{aligned} \tag{3.27}$$

where $\tilde{\boldsymbol{t}}_{,\alpha}^h = \sum_{A=1}^4 N_{,\alpha}^A\boldsymbol{t}_A^0$.

We note that the term $\left[\boldsymbol{I} - \boldsymbol{t}_e^h \otimes \boldsymbol{t}_e^h\right]$ in (3.27) defines an orthogonal projection $\mathbb{P}_t$, illustrated by Figure 3.3. The approximation for $\boldsymbol{t}_{e,\alpha}^h$ is thus given by

$$\boldsymbol{t}_{e,\alpha}^h = \frac{1}{\| \tilde{\boldsymbol{t}}^h \|} \mathbb{P}_t \tilde{\boldsymbol{t}}_{,\alpha}^h. \tag{3.28}$$

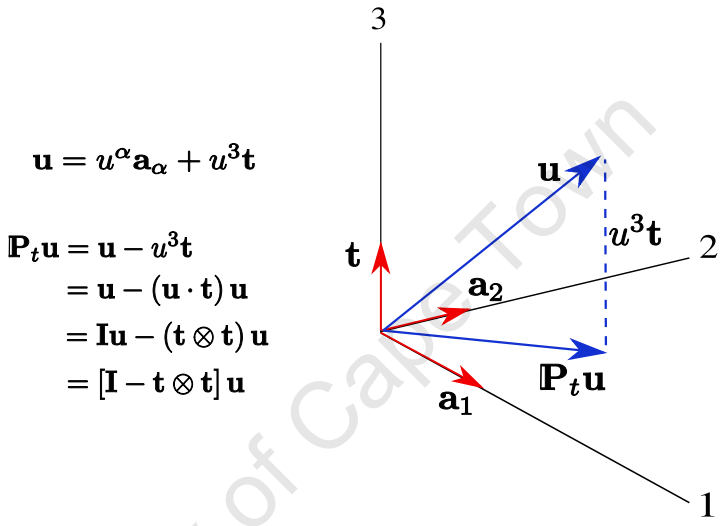

Fig. 3.3. Illustration of projecting a vector onto a plane

Finally, the displacements and change in director are interpolated according to

$$\boldsymbol{u}_e^h = \sum_{A=1}^{4} N^A(\xi, \eta)\, \boldsymbol{u}_A \tag{3.29}$$

and

$$\Delta \boldsymbol{t}^h = \frac{1}{\| \tilde{\boldsymbol{t}}^h \|} \mathbb{P}_t \Delta \tilde{\boldsymbol{t}}^h, \tag{3.30}$$

where $\Delta\tilde{\boldsymbol{t}}^h = \sum_{A=1}^{4} N^A \Delta\boldsymbol{t}_A$ and the same methodology for obtaining $\mathbb{P}_t$ is followed as in (3.27).

Substituting the interpolated relations into the term $\mathbb{B}_{sm}\boldsymbol{v}$, for example, yields:

$$\mathbb{B}_{sm}\boldsymbol{v} = \begin{bmatrix} \mathbf{t}^T \dfrac{\partial}{\partial\xi^1} \\ \mathbf{t}^T \dfrac{\partial}{\partial\xi^2} \end{bmatrix}_{2\times 3} \sum_{A=1}^{4} N^A(\xi,\eta)\,\boldsymbol{v}_A$$

$$= \sum_{A=1}^{4} \underbrace{\begin{bmatrix} \mathbf{t}^T \dfrac{\partial N^A}{\partial\xi^1} \\ \mathbf{t}^T \dfrac{\partial N^A}{\partial\xi^2} \end{bmatrix}_{2\times 3}}_{\mathbb{B}^A_{sm}} \boldsymbol{v}_A \qquad = \mathbb{B}^A_{sm}\boldsymbol{v}_A. \tag{3.31}$$

Following a similar procedure for all of the relevant terms of the weak form, (3.19) becomes

$$\begin{aligned} LHS = &\int_{\mathcal{A}} \left(\sum_{A=1}^{4} \left[\mathbb{B}^A_m \boldsymbol{v}_A\right]^T \mathbf{D_m} \sum_{B=1}^{4} \left[\mathbb{B}^B_m \mathbf{u}_B\right] \right) \bar{j}\, d\xi^1 d\xi^2 \\ &+ \left(\sum_{A=1}^{4} \left[\mathbb{B}^A_{sm}\boldsymbol{v}_A + \mathbb{B}^A_{sb}\boldsymbol{k}_A\right]^T \mathbf{D_s} \sum_{B=1}^{4} \left[\mathbb{B}^B_{sm}\boldsymbol{u}_B + \mathbb{B}^B_{sb}\Delta\boldsymbol{T}_B\right] \right) \bar{j}\, d\xi^1 d\xi^2 \\ &+ \left(\sum_{A=1}^{4} \left[\mathbb{B}^A_{bm}\boldsymbol{v}_A + \mathbb{B}^A_{bb}\boldsymbol{k}_A\right]^T \mathbf{D_b} \sum_{B=1}^{4} \left[\mathbb{B}^B_{bm}\boldsymbol{u}_B + \mathbb{B}^B_{bb}\Delta\boldsymbol{T}_B\right] \right) \bar{j}\, d\xi^1 d\xi^2. \end{aligned} \tag{3.32}$$

The above can be expanded to give

$$LHS = \int_{\mathcal{A}} \sum_{A,B=1}^{4} \left(\boldsymbol{v}_A^T \mathbb{B}_m^{A^T} \mathbf{D_m} \mathbb{B}_m^B \mathbf{u}_B + \boldsymbol{v}_A^T \mathbb{B}_{sm}^{A^T} \mathbf{D_s} \mathbb{B}_{sm}^B \boldsymbol{u}_B + \boldsymbol{k}_A^T \mathbb{B}_{sb}^{A^T} \mathbf{D_s} \mathbb{B}_{sm}^B \boldsymbol{u}_B \right) \bar{j} d\xi^1 d\xi^2$$

$$+ \left(\boldsymbol{v}_A^T \mathbb{B}_{sm}^{A^T} \mathbf{D_s} \mathbb{B}_{sb}^B \Delta \boldsymbol{T}_B + \boldsymbol{k}_A^T \mathbb{B}_{sb}^{A^T} \mathbf{D_s} \mathbb{B}_{sb}^B \Delta \boldsymbol{T}_B + \boldsymbol{v}_A^T \mathbb{B}_{bm}^{A^T} \mathbf{D_b} \mathbb{B}_{bm}^B \boldsymbol{u}_B \right) \bar{j} d\xi^1 d\xi^2$$

$$+ \left(\boldsymbol{k}_A^T \mathbb{B}_{bb}^{A^T} \mathbf{D_b} \mathbb{B}_{bm}^B \boldsymbol{u}_B + \boldsymbol{v}_A^T \mathbb{B}_{bm}^{A^T} \mathbf{D_b} \mathbb{B}_{bb}^B \Delta \boldsymbol{T}_B + \boldsymbol{k}_A^T \mathbb{B}_{bb}^{A^T} \mathbf{D_b} \mathbb{B}_{bb}^B \Delta \boldsymbol{T}_B \right) \bar{j} d\xi^1 d\xi^2. \quad (3.33)$$

We need to write the entire system in the matrix form $\mathbb{K}\mathbb{D} = \mathbb{F}$. Performing matrix multiplication, a range of different sized subsidiary $\boldsymbol{K}$ matrices are constructed according to:

$$\boldsymbol{K}_{sub}^{AB} = \int_{\mathcal{A}} \mathbb{B}^{A^T} \mathbf{D} \mathbb{B}^B \bar{j} d\xi^1 d\xi^2.$$

The LHS then becomes

$$LHS = \sum_{A,B=1}^{4} \boldsymbol{v}_A^T \boldsymbol{K}_m^{AB} \mathbf{u}_B + \boldsymbol{v}_A^T \boldsymbol{K}_{sm}^{AB} \boldsymbol{u}_B + \boldsymbol{k}_A^T \boldsymbol{K}_{sbm}^{AB} \boldsymbol{u}_B$$

$$+ \boldsymbol{v}_A^T \boldsymbol{K}_{sbm}^{BA} \Delta \boldsymbol{T}_B + \boldsymbol{k}_A^T \boldsymbol{K}_{sb}^{AB} \Delta \boldsymbol{T}_B + \boldsymbol{v}_A^T \boldsymbol{K}_{bm}^{AB} \boldsymbol{u}_B$$

$$+ \boldsymbol{k}_A^T \boldsymbol{K}_{bbm}^{AB} \boldsymbol{u}_B + \boldsymbol{v}_A^T \boldsymbol{K}_{bbm}^{BA} \Delta \boldsymbol{T}_B + \boldsymbol{k}_A^T \boldsymbol{K}_{bb}^{AB} \Delta \boldsymbol{T}_B. \quad (3.34)$$

The sizes of these subsidiary $\boldsymbol{K}$ matrices varies according to how the constitutive relations are associated with the nodal displacements $\boldsymbol{u}$, change in directors $\Delta \boldsymbol{t}$ and their corresponding test functions $\boldsymbol{v}$ and $\boldsymbol{k}$ respectively. Due to this, and after the omission of the arbitrary $\boldsymbol{v}_A$ and $\boldsymbol{k}_A$ functions, the system stiffness matrix, $\mathbb{K}$, and displacement field, $\mathbb{D}$, for one element, can be written in the form

$$\begin{bmatrix} \cdots \mathbf{d}^A \cdots \cdots \end{bmatrix}^T_{1\times 20} \begin{bmatrix} \cdots & \cdots & \cdots & \cdots \\ \cdots & \cdots & \boldsymbol{K}^{AB} & \cdots \\ \cdots & \cdots & \cdots & \cdots \\ \cdots & \cdots & \cdots & \cdots \end{bmatrix}_{20\times 20} \begin{bmatrix} \cdots \\ \mathbf{d}^B \\ \cdots \\ \cdots \end{bmatrix}_{20\times 1},$$

for nodes A and B, where

$$\boldsymbol{K}^{AB} = \begin{bmatrix} \boldsymbol{K}^{AB}_{m} + \boldsymbol{K}^{AB}_{sm} + \boldsymbol{K}^{AB}_{bm}{}_{3\times 3} & \boldsymbol{K}^{BA}_{sbm} + \boldsymbol{K}^{BA}_{bm}{}_{3\times 2} \\ \boldsymbol{K}^{AB}_{sbm} + \boldsymbol{K}^{AB}_{bm}{}_{2\times 3} & \boldsymbol{K}^{AB}_{sb} + \boldsymbol{K}^{AB}_{bb}{}_{2\times 2} \end{bmatrix}_{5\times 5} \tag{3.35}$$

and

$$\mathbf{d}^B = \begin{bmatrix} \boldsymbol{u}^B \\ \Delta\boldsymbol{t}^B \end{bmatrix}_{5\times 1}. \tag{3.36}$$

3.5 Boundary conditions

In this study there are four types of boundary conditions that are common to many of the benchmark and example problems. We will look at these in closer detail in terms of how particular components of the displacement field can be prescribed.

a) The clamped condition: for all boundaries falling into this category we set $\boldsymbol{u} = \mathbf{0}$ and $\Delta\boldsymbol{t} = \mathbf{0}$.

b) The free boundary: here $\bar{\tilde{\boldsymbol{n}}} = \mathbf{0}$, $\bar{\tilde{\boldsymbol{m}}} = \mathbf{0}$ and $\boldsymbol{q} = \mathbf{0}$. There is no stipulation placed on the displacement field.

c) The hinged boundary: here $\bar{\tilde{\boldsymbol{m}}} = \mathbf{0}$ and we set $\boldsymbol{u} = \mathbf{0}$.

d) The symmetry condition: to invoke a symmetry boundary condition, as illustrated in Figure 3.4, we need to ensure that at the symmetry boundary only in-plane motion is allowed. Following the definition of a projection onto a plane, as shown in Figure 3.3, it is specified for $\Delta \boldsymbol{t}$ by

$$\Delta \boldsymbol{t} - (\Delta \boldsymbol{t} \cdot \boldsymbol{w})\, \boldsymbol{w} = \boldsymbol{0}$$

or

$$\underbrace{(\boldsymbol{I} - \boldsymbol{w} \otimes \boldsymbol{w})}_{\mathbb{P}} \Delta \boldsymbol{t} = \boldsymbol{0}$$

where $\boldsymbol{w}$ is a vector in the symmetry plane. Similarly for the displacements, $\mathbb{P}\boldsymbol{u} = \boldsymbol{0}$

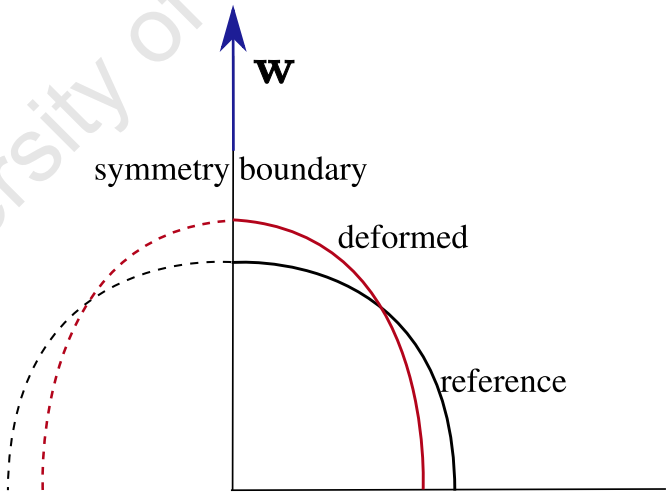

Fig. 3.4. Schematic showing a symmetry boundary condition

3.6 Gaussian quadrature

The final step in the finite element method uses numerical integration to evaluate the integrals. We make use of Gaussian quadrature, in which the integral over an element is approximated as the sum over all quadrature points of the designated function at the current quadrature point mulitplied by the respective weighting value of that quadrature point. In so doing, each subsidiary $\boldsymbol{K}$ in the weak form (3.34) is obtained as

$$\boldsymbol{K}_m^{AB} = \sum_{e=1}^{N^e} \sum_{qp=1}^{N^{qp}} \sum_{A,B=1}^{4} \mathbb{B}_m^{A^T} \mathbf{D}_m \mathbb{B}_m^B \bar{j} \mathcal{W}(qp) \tag{3.37}$$

where N^e is the number of elements in the domain and N^{qp} is the number of quadrature points per element.

3.7 Selective reduced integration

It is a well-known fact that as one reduces the thickness of a shell the accuracy of the approximation deteriorates. This comes about as a result of the thickness factor h present in the shear terms as opposed to h^3 present in the bending terms. This phenomenon is known as shear locking and, while for in-plane problems it causes no concern, it is a limiting factor in solving bending and shear related problems. Due to the types of problems being tackled here as well as the nature of the future development of this formulation for biomedical applications it was necessary to include measures to deal with problems in the thin shell limit. Simo and Fox have employed a method, based on the Hu-Washizu principle developed by Bathe and Dvorkin [14], to deal with this problem known as the *assumed strain method*. This changes the way in which one interpolates tranverse shear strains. Alternatively, the problem can be addressed by underintegrating the shear terms. Gosz [22] utilised

this method, and due to the relative ease with which it could be implemented as well as its ability to deal with the shear locking issue it was the approach adopted here. This technique is known as the *method of selective reduced integration* [23].

From (3.37) it can be seen that approximating the the subsidiary $\boldsymbol{K}$ matrices for each element involves a sumation over each quadrature point, where the location of the quadrature points for this formulation can be viewed in Figure 3.2. The method of selected reduced integration involves underintegrating the $\mathbb{B}_{sm}$ and $\mathbb{B}_{sb}$ from (3.33), by utilising only one quadrature point per element. Subsequently each subsidiary $\boldsymbol{K}$ matrix to do with shear is also underintegrated.

4

Implementation

The shell forumulation was implemented in deal.II, an open-source finite element library of C++ code [13]. deal.II provides a set of tools to facilitate the implementation of finite element formulations but does not directly accommodate shells. In terms of setting up the computational structure in deal.II, the challenges included the process of translating a three-dimensional surface into a two-dimensional geometry, taking into account the additional director degrees of freedom and managing the numerous variables at nodes and quadrature points.

This chapter explains how some of the aforementioned challenges were dealt with in terms of the choice of programming language, the pre-processing measures taken, as well as how the code was structured. deal.II itself is not used here to construct complex geometries and meshes, nor is it used to view the results obtained. In our case, the geometry construction and meshing has been carried out using the programme Cubit [5], and the results viewed in the open-source programme ParaView [10]. Figure 4.1 summarises the three key components of the implementation: pre-processing, solving and post-processing.

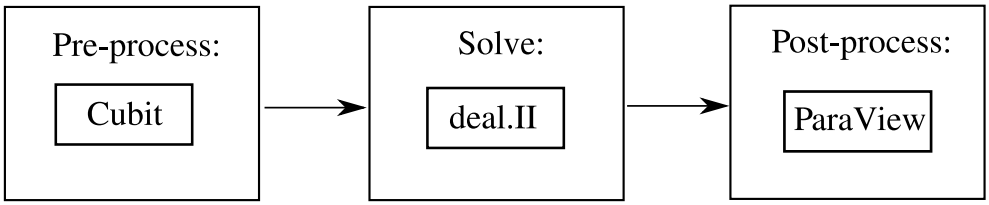

Fig. 4.1. The process followed for implementing the shell formulation

4.1 deal.II

deal.II (differential equations analysis library), is essentially a tool for solving a vast range of partial differential equations using finite element approximations [12]. The library itself is large and, given its complexity and broad range of functions, requires a good understanding of C++ as well as sufficient time to familiarise oneself with it. However, the flexibility it offers in terms of managing complex problems makes it a good choice for the problem considered. deal.II would also be of great value in extending this code to model nonlinear biological materials and the effect of solid-fluid interactions, which are of paramount importance for the realistic modelling of a cardiovascular system.

The system to be solved is made up of many matrices linked in various ways to the nodal positions and directors with their responses governed by their specific constitutive relations. deal.II allows the incorporation of additional nodal degrees of freedom into a system and the flexibility to fill the system matrix as dictated by the formulation. deal.II constructs the stiffness matrix from contributions at the level of the degree of freedom of an element and not in a nodal manner, as is normally the case in finite element codes. Also worth noting is deal.II's use of the unit square as a reference element, as apposed to the familiar biunit square.

4.2 Pre-processing

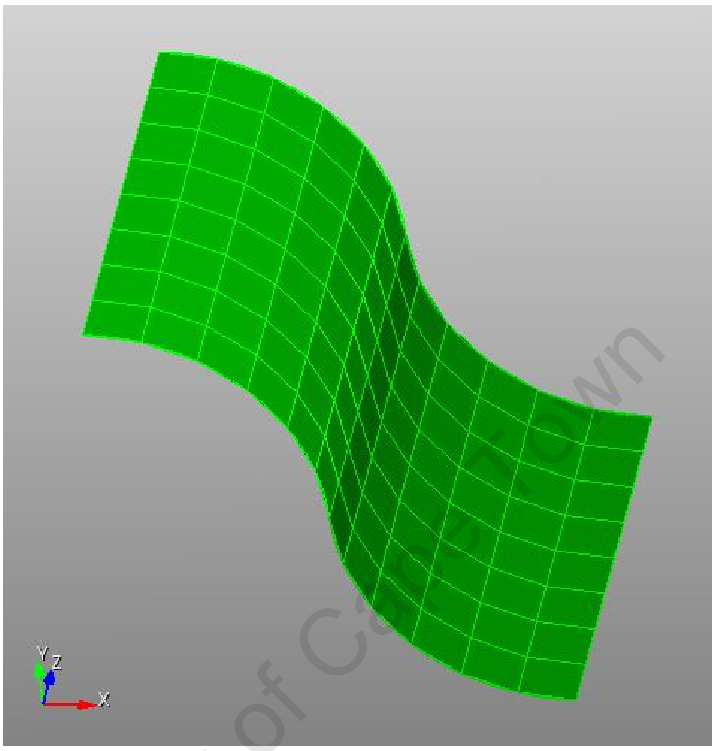

Fig. 4.2. An arbitrary surface in three dimensions, created and meshed in Cubit

Figure 4.2 shows an arbitrary three-dimensional surface constructed and meshed using the programme Cubit. Cubit can generate a file which translates the geometric and topological information of the mesh into a format that deal.II can interpret. Utilising this file in one's code enables one to use deal.II's functionality to associate the degrees of freedom and finite element interpolations to the mesh quite easily. However, additional complications in the case of the shell problem arises due to the finite element mapping between a two-dimensional reference element to a surface in three dimensions, see Figure 3.2. If the file generated by Cubit for a three-dimensional surface is used directly within deal.II, it would associate three-dimensional shape functions with it. However, a coherent link between the geometry of the system and the coded formulation must be maintained. It was decided that if information pertaining to a two-dimensional mesh could be sent in,

providing the correct data relating to element connectivity as well as boundary positions, then the appropriate finite element values would be generated by deal.II.

The original orientation of each point in three-dimensional space as well the corresponding director vector are required for various calculations in the formulation, so an additional data deck needed to be created to house this information.

Furthermore, an additional Jacobian determinent would need to be calculated to provide a link between the change in area taking place between the three-dimensional elements and the two-dimensional elements, since deal.II's capabilities only determine those between its reference element and the mesh it read in.

After the three-dimensional shell surface is created and meshed in Cubit, appropriate boundaries are labelled with specific boundary identities. These boundary identites will be used at a later point in the solving structure for loading and specifying boundary conditions. Pre-processing is then done using the output file from Cubit utilising a MATLAB [9] routine coded for this purpose.

Based on the geometry of the shell surface a decision has to be made about how to create a two-dimensional geometry. One possible option is to map the three-dimensional surface onto a cylinder or a sphere in order to "remove" one of the dimensions. This is demonstrated in Figure 4.3 which shows a map of the abitrary mesh from Figure 4.2 onto a cylinder.

As illustrated by Figure 4.4, the surface mesh is presented on a two-dimensional cylindrical coordinate system (θ, z). The MATLAB routine now uses the locating information pertaining to this mesh with its boundary information (which is the same as the three-dimensional surface) to output a file in the same format as the original Cubit output file.

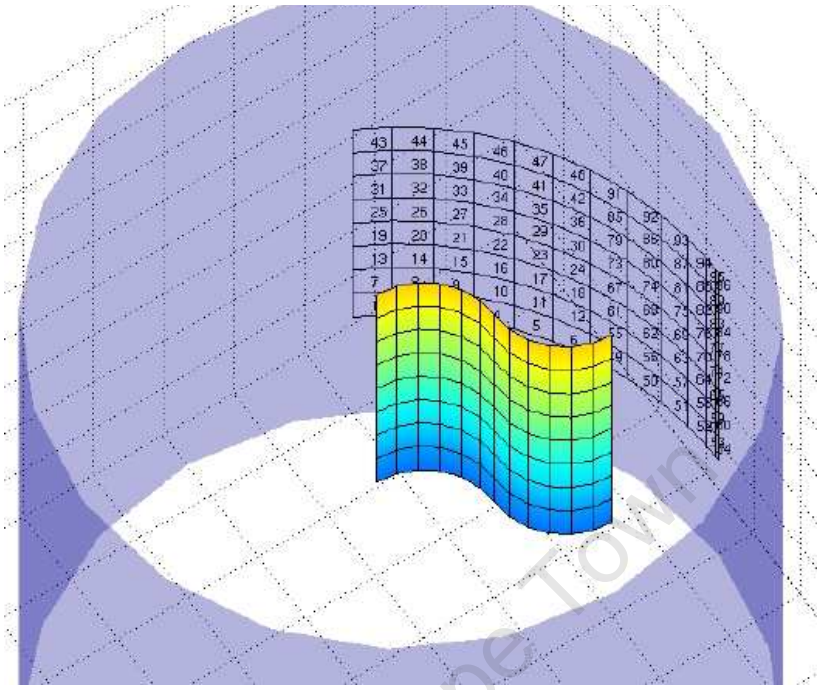

Fig. 4.3. Mapping of an arbitrary three-dimensional surface onto a cylinder surface

The MATLAB script creates the additional data deck that will provide director and three-dimensional locating information for use in deal.II. A surface vector describing the line from every nodal point on the three-dimensional surface to its adjacent nodal point is calculated using the three-dimensional data obtained from the Cubit output file. The director vector, which is normal to the surface at each nodal point, is created by averaging and normalising the sum of cross products between a surface vector with its adjacent surface vector at a node. Figure 4.5 displays these directors on the arbitrary shell surface.

The director vector, three-dimensional surface location and two-dimensional surface location for each nodal point are output into the data deck.

Since this was an arbitrary example, the two-dimensional mesh shown is purely illustrative. For the mesh to be sent into deal.II, care must be taken to ensure that the three-dimensional surface is orientated in such a way as to minimise the distortion of the two-dimensional elements.

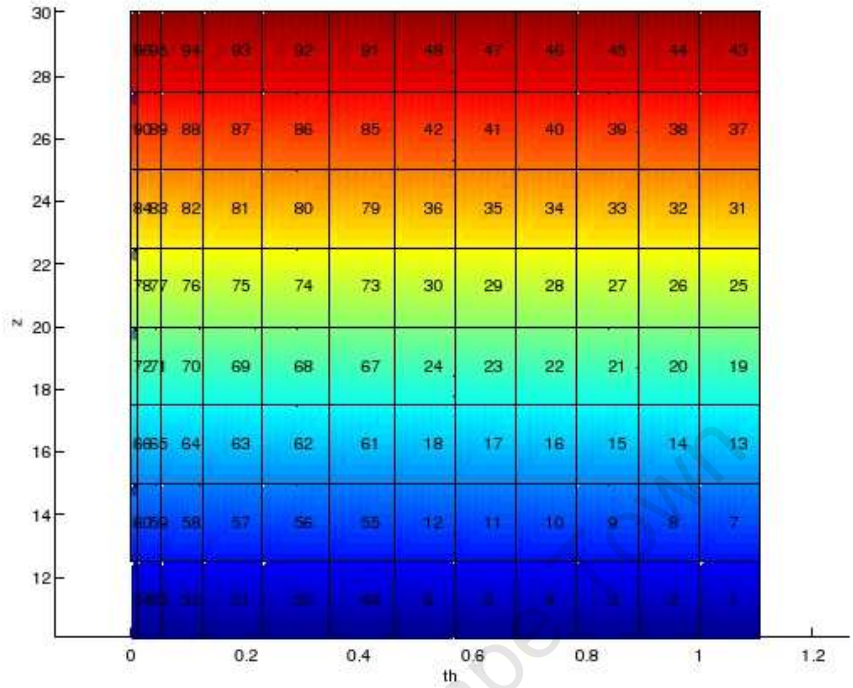

Fig. 4.4. The two-dimensional mesh after the mapping has taken place

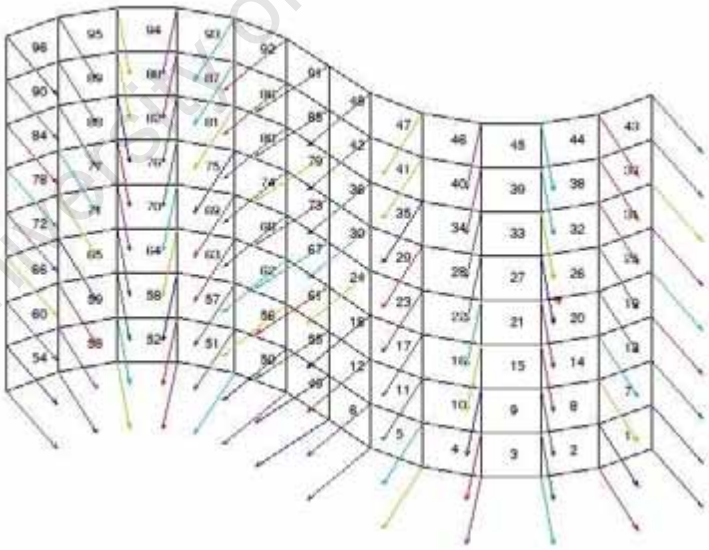

Fig. 4.5. The arbitrary three-dimensional surface showing the director vector at each point

4.3 An overview of the structure of deal.II

Before explaining the structure of the shell solution algorithm, it is necessary to present the most important groups of classes in deal.II associated with the solving of finite element problems. Using Figure 4.6 as a basis for this overview, we will briefly explain this classification of groups. There are numerous other classes in deal.II that are beyond the scope of this discussion.

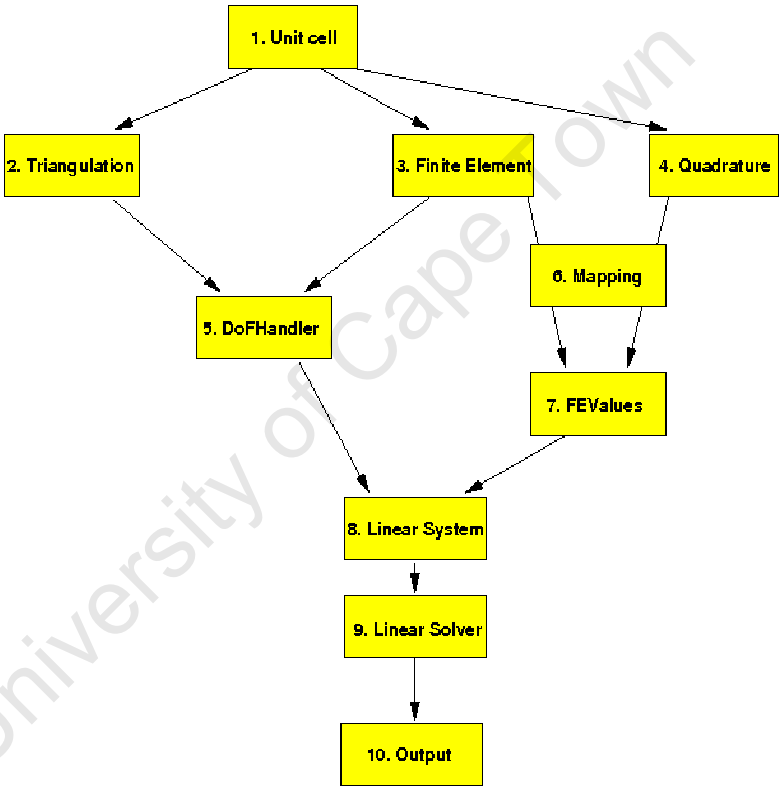

Fig. 4.6. Collaboration diagram for the most important groups of classes in deal.II, taken from [6]

We begin with the *Unit cell*. In deal.II the only type of reference element for one, two and three dimensions is the unit line, unit square and unit cube respectively. The *GeometryInfo* class describes properties of the unit cell (or element, as we will refer to it here) such as number of vertices, ordering of faces and edge directionality.

In deal.II a mesh is essentially a collection of elements described by the *Triangulation* class. This class only stores where each vertex is located and the connectivity of these vertices to elements. Querying any information about a triangulation is generally done by iterating over all the elements, or all the faces of an element. Pointer-like structures, known as iterators, allow access to the first and last element of the triangulation, and by looping over elements information about any element can be obtained.

The properties of the finite element space, such as knowledge about the number of degrees of freedom on a given geometric aspect of an element, or values and gradients of individual shape functions at various points on an element, are described by *Finite element* classes.

Quadrature objects give the location and respective weights of quadrature points on the unit element.

The *DoFHandler* class acts as a merging agent between triangulations and finite elements and assigns global numbering to geometric entities. Based on the number of vertices, lines and elements present in a triangulation the *DoFHandler* object apportions space according to the number of degrees of freedom needed, as designated by the finite element class. Most processes on DoFHandlers are done, once again, by iterating over all the elements.

Calculating the stiffness matrix and right-hand entries for each element is a primary activity for a finite element program. This is done by making use of the shape functions and quadrature points that have been defined as per the functionality of the finite element and quadrature classes. To achieve this, shape functions, quadrature points and quadrature weights need to be linked from the unit element to each element in the triangulation. The *Mapping* class assists the process of mapping points from unit to real space and vice versa. This class also provides the Jacobian determinants.

Given finite element, quadrature and mapping objects the *FEValues* class has the ability to evaluate shape functions and gradients at quadrature points, when they have been mapped to an element in the triangulation. It is here that a continuous function space is restricted to a discrete number of points.

Using DoFHandler iterators and the ability to evaluate shape functions and gradients due to the FEValues class, assembly of the stiffness matrix and right-hand side of the *Linear System* can be done. deal.II provides a range of vector and matrix classes to facilitate this process.

The *Linear Solver* classes in deal.II makes use of a range of techniques for solving a linear system of equations. The solvers are often iterative, but deal.II also contains numerous direct and sparse direct solvers.

The final component of the finite element collaboration of classes in deal.II is the *Output*. After solving there is a library that enables the output of the solution into various formats that can be understood by a range of visualisation programmes, such as ParaView.

4.4 Structure of the solution algorithm

The aim of this section is to provide a coherent link between the weak formulation presented in Chapter 3 and the corresponding numerical implementation. For the shell problem there were a range of classes that needed to be created to manage the various components of the formulation. The detail of each of these classes is listed below, followed by the solution algorithm given as pseudo-code in Algorithm 4.1.

The *ShellPoints* class caters for the specific format of the additional data deck, which contains a director vector, three-dimensional point and two-dimensional point for each node in the mesh. An instance of this class is created for every nodal point

on the two-dimensional mesh. When looping over each element of the triangulation this information can be retrieved as necessary.

Many of the variables utilised in the shell formulation need to be evaluated at the quadrature points of each element. The *PointHistory* class was created so that the calculation of these variables can be removed from the main formulation and so that they need not be recalculated. To allocate the correct amount of memory, a pointer to a vector of quadrature history objects is created based on the mesh size and quadrature rule. We are now able to store and access information at each quadrature point. The *PointHistory* class loops over each element, quadrature point and, where applicable, each node and determines the relevant variables then stores them. The variables stored at each quadrature point are: $\bar{\boldsymbol{\Lambda}}$, $\mathbf{D}_m$, $\mathbf{D}_s$, $\mathbf{D}_b$ and each of the five $\boldsymbol{B}$ matrices stored four times at each quadrature point as evaluated for each node.

ShellUtility was created to house a number of utility functions separately from the shell algorithm. Its purpose is to remove the clutter and complexity of a host of values, vectors and matrices that need to be calculated as well as miscellaneous tasks that need to be performed at different instances of the shell formulation. Some of its functions include: determining $\boldsymbol{a}_\alpha$, $\boldsymbol{t}$, $\boldsymbol{t}_{,\alpha}$, $\boldsymbol{\Lambda}$, the $\mathbf{D}$ matrices, each $\boldsymbol{B}$ matrix, making the subsidiary $\boldsymbol{K}$ matrices, populating the element stiffness matrix, calculating the extra Jacobian determinant and helping with the management of specialised boundary conditions.

Two subsidiary classes were created for specifying and applying loading to boundaries and areas of the shell surface. These are *rhsConditions* and *pressureConditions* respectively.

Finally, the *ShellFormulation* class encapsulates a range of activities that begin with setting up the system and end with outputting the solution. The pseudo-code shows only the key features of the process followed in solving the shell formulation.

Algorithm 4.1 Fundamental structure of the shell formulation

Initialisation

- Initialise the triangulation
- Read in the two-dimensional mesh
- Read in the additional data deck
- Intialise DoFHandler, FEValues, system stiffness matrix $\mathbb{K}$, system RHS vector $\mathbb{F}$ and system solution vector $\mathbb{D}$
- Set up quadrature history

for each element **do**
  for each quadrature point **do**
    for each node $(A = 1, \cdots, 4)$ **do**
      for each node $(B = 1, \cdots, 4)$ **do**
        Use stored quadrature history values to calculate subsidary $\boldsymbol{K}$ matrices of general form: $\boldsymbol{K}^{AB}_{\text{sub}} = \int_{\mathcal{A}_e} \mathbb{B}^{A^T} \mathbf{D} \mathbb{B}^B \bar{j} d\xi^1 d\xi^2$
        Add contribution from $\boldsymbol{K}^{AB}_{\text{sub}}$ to element stiffness matrix $\mathbb{K}^e$
      end for
    end for
  end for
  if element at mesh boundary **then**
    if boundary-element at loading boundary **then**
      for each face-quadrature point **do**
        Apply load
        Add value to $\mathbb{F}^e$
      end for
    end if
  end if
  if element has an applied surface pressure **then**
    for each quadrature point **do**
      Apply pressure
      Add value to $\mathbb{F}^e$
    end for
  end if
  Send $\mathbb{K}^e$ to global $\mathbb{K}$
end for

- Apply Dirichlet (Essential) boundary conditions
- Solve $\mathbb{K}\mathbb{D} = \mathbb{F}$
- Post-processing of solution
- Output solution variables to file

5

Benchmarking

To test the validity and accuracy of the computational implementation various benchmark tests were carried out. These tests examine the response of a shell undergoing pure membrane deformation, as well as bending of a flat plate and cylinder. Two examples, viz. the Cook membrane problem and the pinched cylinder, are taken from [30]. The clamped plate problem, set out in [22], was also used for comparative purposes.

This chapter will set out the results for the benchmark problems and show how they compare with results in the literature as well as, in applicable thick shell cases, with a 3D elasticity code constructed in deal.II. The effects of entering the thin shell limit, the use of selected reduced integration and the results of including transverse isotropy in a flat plate are also examined.

5.1 Cook membrane test

The Cook membrane problem is a well-known problem for testing the capabilities of a structure undergoing in-plane loading. It involves the clamping of a trapezoidal plate along one edge and subjecting it to a distributed load along the other edge, in-plane, as Figure 5.1 shows. Due to the large shear deformation that takes place in-plane, this test can ascertain an element's ability to model membrane-dominated

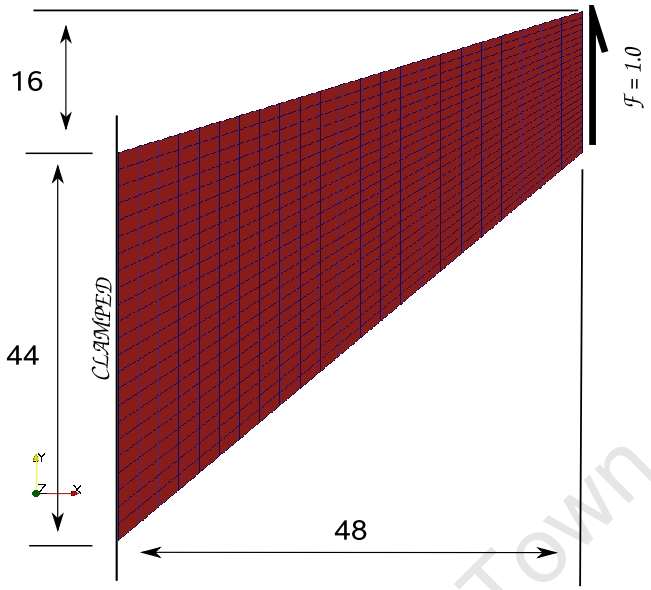

Fig. 5.1. Parameters of the Cook's membrane test

situations. Specifically in the formulation used here, it is the $\mathbb{B}_m$ matrices within the system stiffness matrix that are activated and which govern the response of the system. The directors are in no way affected. The skew nature of the elements in the mesh also make for an excellent way to test the formulation for distorted meshes. The material properties of the system are as follows: Young's modulus $E = 1.0$, Poisson's ratio $\nu = 0.33$, and the thickness of the plate $h = 1.0$.

A comparison can be seen between the solution obtained using the elasticity code and the shell formulation, in Figure 5.2. For each the mesh refinement was approximately the same, with the three-dimensional solid elasticity mesh containing 525 hexahedral elements, and the three-dimensional surface shell mesh containing 529 elements.

A finite element converged solution of 25.114 is used to normalise the results obtained from the shell formulation for five different mesh sizes, namely 21, 100, 256, 529 and 12024 elements. Figure 5.3 shows the expected convergence of the solution as refinement increases.

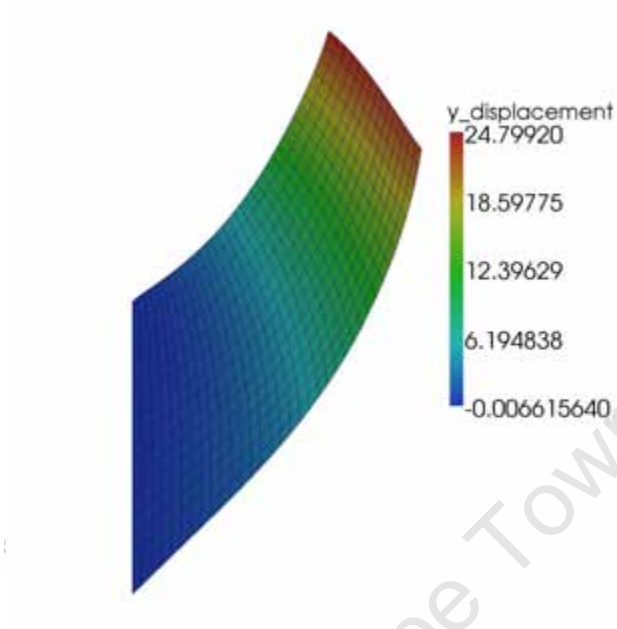

(a) Elasticity solution

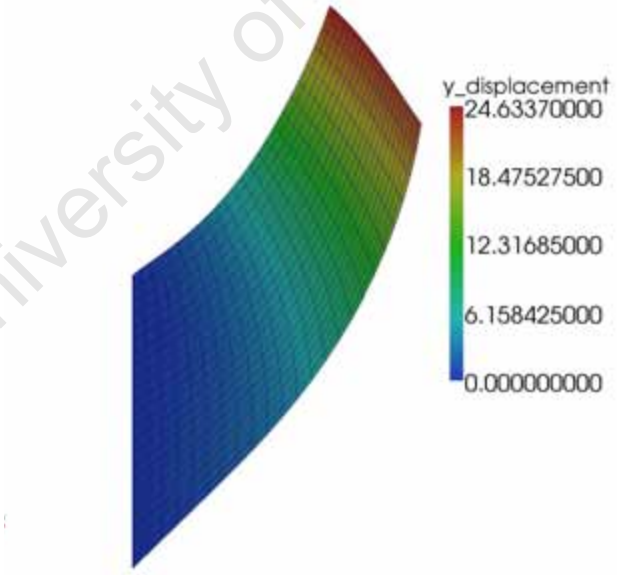

(b) Shell solution

Fig. 5.2. Results of the Cook's membrane test

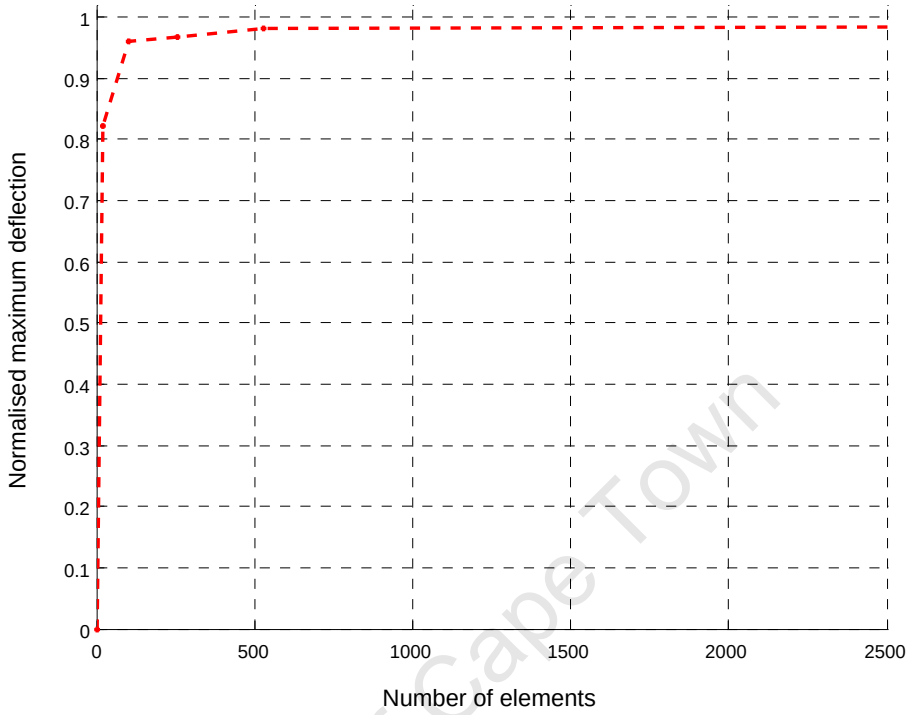

Fig. 5.3. Convergence of the shell formulation for the Cook's membrane test

5.2 The clamped plate

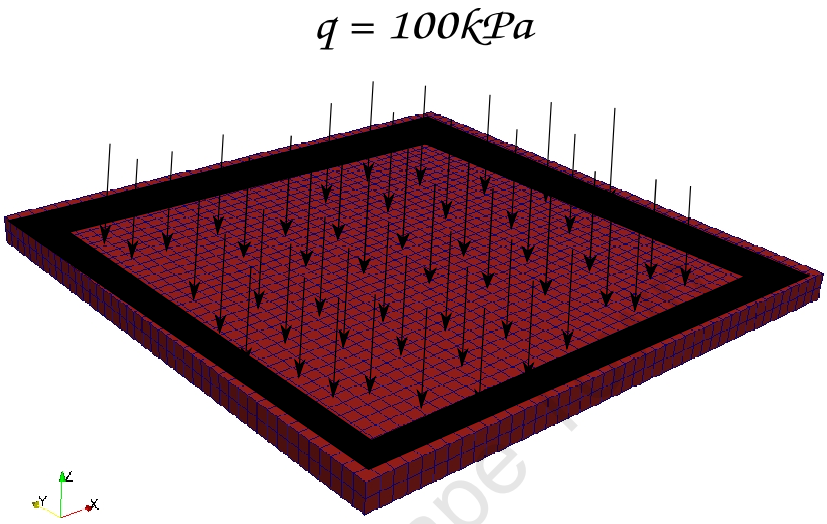

Fig. 5.4. Setup for the deflection test of a clamped plate

The next test to be performed is one to ascertain the out-of-plane response of the shell formulation. To do this we consider the deflection of a clamped plate loaded by a uniform traction, as shown in Figure 5.4. The $2m \times 2m$ plate, clamped on all edges, is loaded in the negative z-direction with a distributed load of $q = 100kPa$. The material properties of the linearly elastic and isotropic plate are $E = 200GPa$ and $\nu = 0.3$. The plate was tested with a thickness of $0.1m$ and $0.01m$, since another aim of this test is also to compare the response for thin plates. We expect that in the thin limit the standard shell element would experience locking, and the deflections would be grossly underestimated. Thus, we compare the results of the standard shell formulation with that using selective reduced integration.

Also useful in this test is the analytical solution for the midpoint deflection, v^c, which is given by

$$v^c = \alpha \frac{qa^4}{D},$$

where, to ten decimal places, $\alpha = 1.265319087 \times 10^{-3}$, a is the length of the square plate and

$$D = \frac{E}{1-\nu^2}\frac{h^3}{12}.$$

For a thickness of 0.1 the exact solution of the mid-point deflection is $v^c_{\text{exact}} = 0.000110538$. The results for the elasticity code and the standard shell are shown in Figure 5.5. They compare quite favourably to the exact solution with $v^c_{\text{elasticity}} = 0.0001160$, and $v^c_{\text{std shell}} = 0.0001070$.

Since we have out-of-plane deflections, it is important to view the response of the directors. For this particular test, the deflections are miniscule and so for the purposes of viewing ease the new director vectors of the system have been scaled up, as Figure 5.6 shows.
When repeating the test for a thickness of 0.01 the locking issues becomes apparent. Figure 5.7 shows the comparison between the standard shell formulation and that using selected reduced integration (SRI). The exact mid-point deflection of the 0.01 thick plate was calculated to be $v^c_{\text{exact}} = 0.1105382$. The shear locking phenomenon is demonstrated in the standard shell whose deflection is $v^c_{\text{std shell}} = 0.01207$, while the inclusion of selected reduced integration yields a favourable $v^c_{\text{SRI}} = 0.11016$.

The plot in Figure 5.8 demonstrates the comparative deflections for each case, this time along a diagonal line through the plate. Here the solution is normalised with the exact solution. This example highlights the need for including a method such as selected reduced integration, and demonstrates how well the shell formulation captures the deformation of the system.

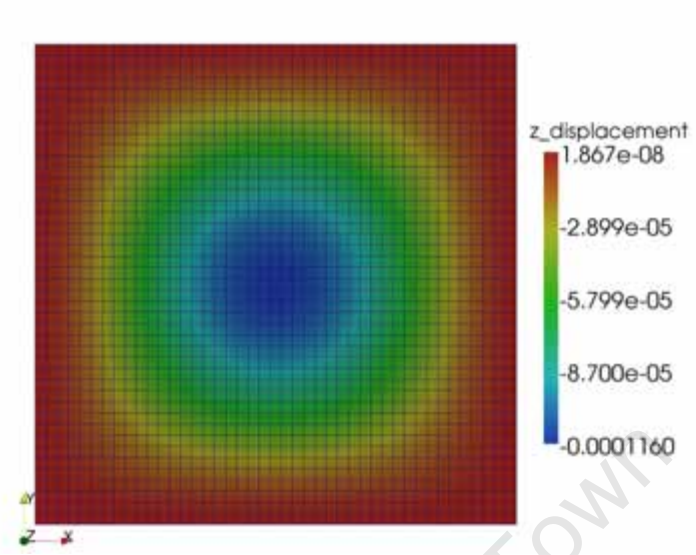

(a) Elasticity Solution

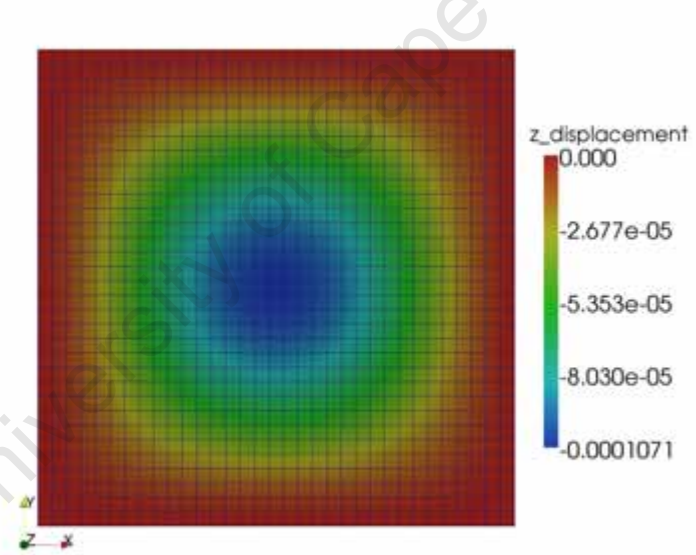

(b) Standard Shell Solution

Fig. 5.5. Results for the deflection of a 0.1 thick clamped plate

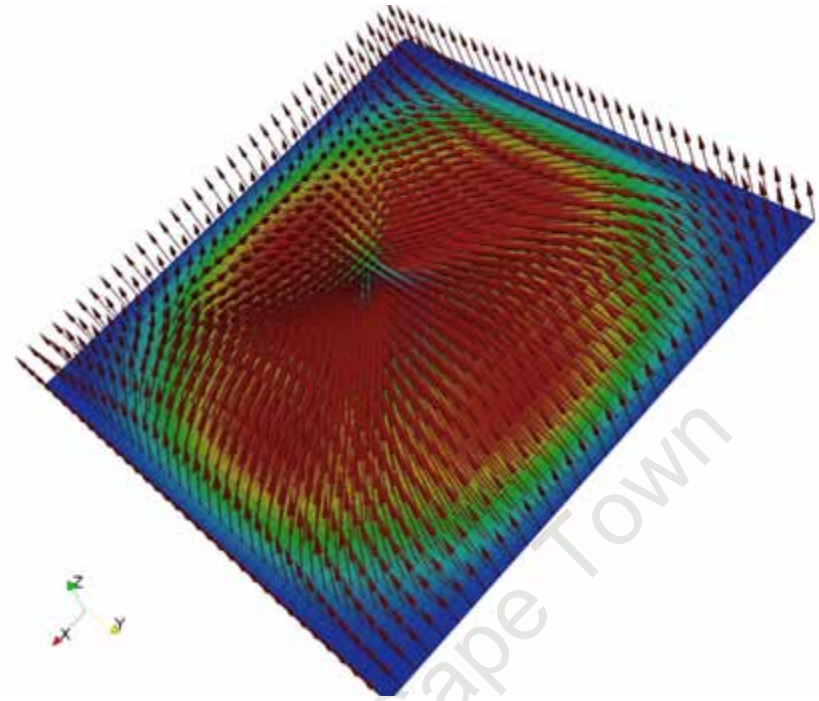

(a) Top view

(b) Side view

Fig. 5.6. Exaggerated results for the change in director vectors of the clamped plate test

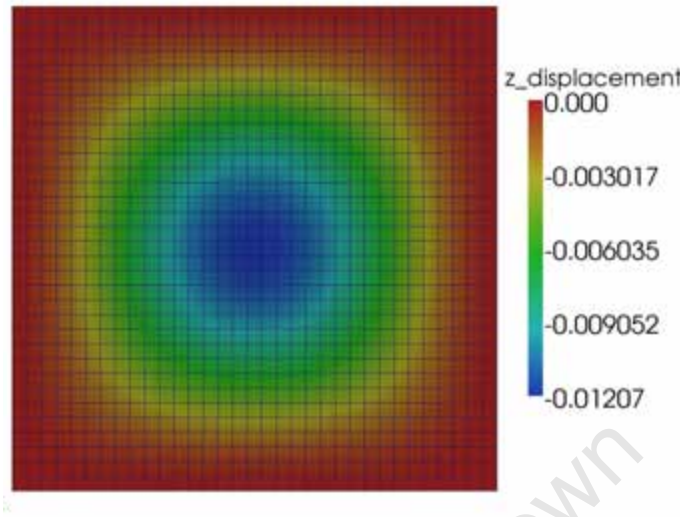

(a) Standard shell solution

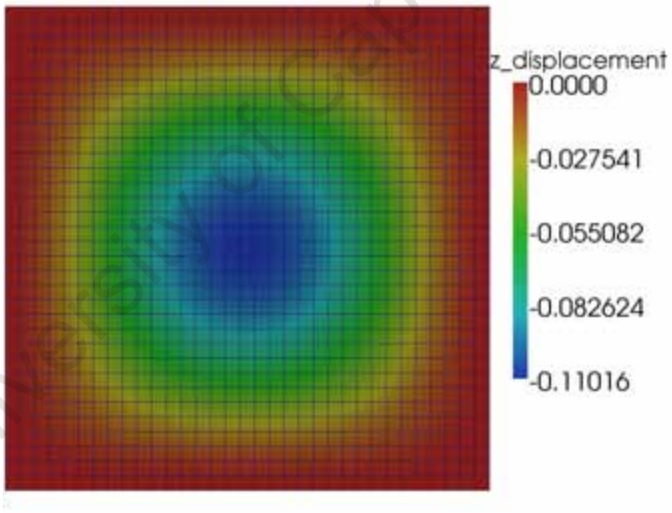

(b) Selective reduced integration shell solution

Fig. 5.7. Results for the deflection of a 0.01 thick clamped plate

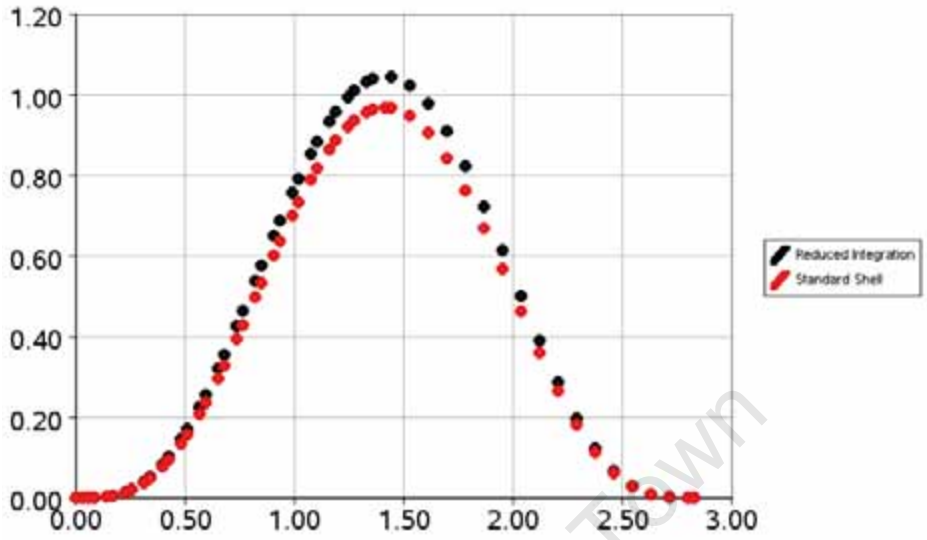

(a) 0.1m plate thickness

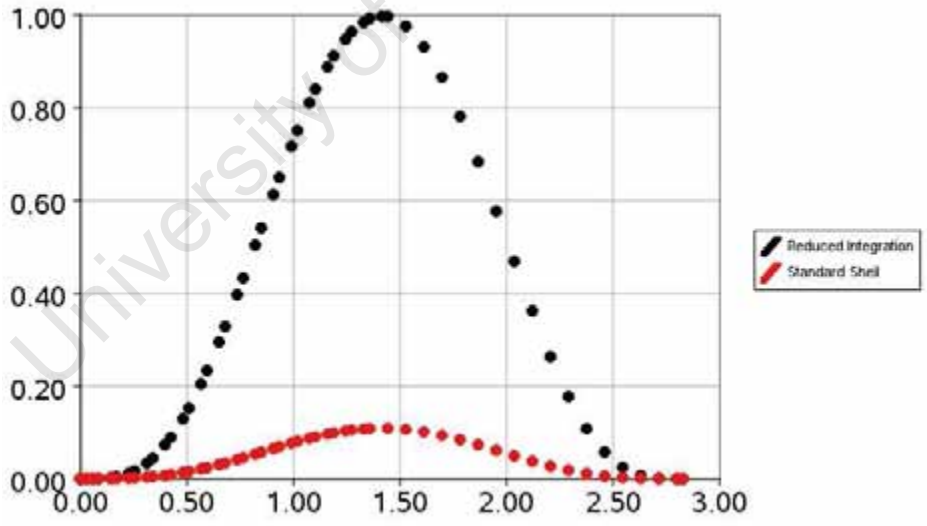

(b) 0.01m plate thickness

Fig. 5.8. Comparison of the standard shell solution with selective reduced integration for different plate thicknesses, normalised with the exact solution

5.3 The Pinched Cylinder Test

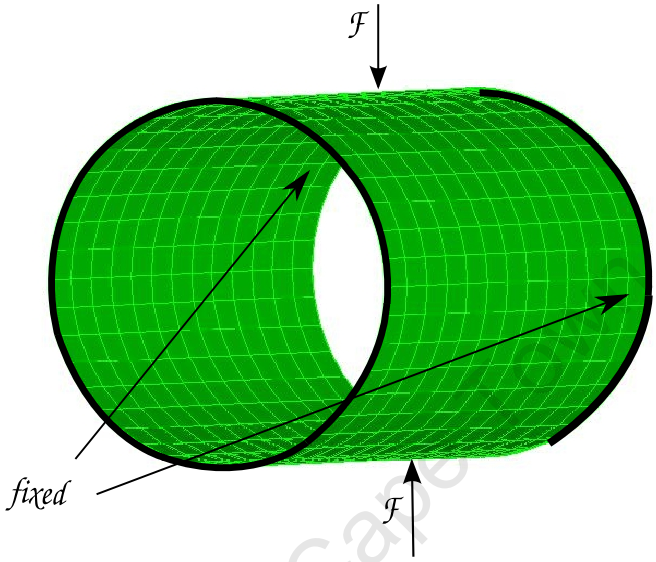

Fig. 5.9. Setup for the pinched cylinder test

This benchmark test from [30] involves a short cylinder, as shown in Figure 5.9, clamped at both ends and subjected to two pinching vertical forces at its centre. The parameters of the cylinder are as follows: length $L = 600$, radius $R = 300$, thickness $h = 3$, Young's modulus $E = 3 \times 10^6$, $\nu = 0.3$, and the pinching force $F = 1$. Using symmetry boundary conditions, as discussed in Chapter 3, only a quarter of the cylinder needs to be modelled. Figure 5.10 schematically shows how the symmetry boundary conditions are applied for this example.

The thickness-to-radius ratio of the cylinder used in this problem quite obviously puts it in the thin shell category. Due to this, selected reduced integration was employed for all the simulations performed. Figure 5.11 illustrates the solution obtained for a mesh of 1156 elements. The analytical solution, given in [30], for the maximum deflection is $1.82488\, e^{-5}$. The deflection of the mesh illustrated reaches 98.198 % of this value with its result of $1.792\, e^{-5}$.

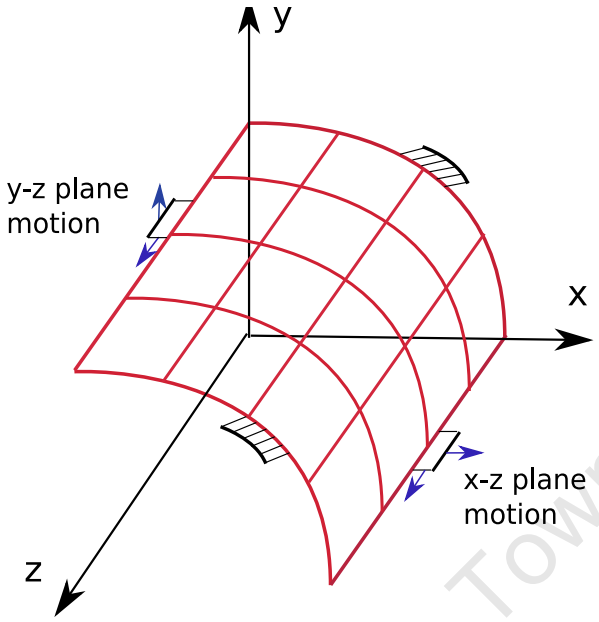

Fig. 5.10. Schematic illustrating the symmetry boundary conditions used to model a quarter of a pinched cylinder

A range of simulations for the pinched cylinder problem were run using meshes of varying refinement. The deflection results for meshes of 64, 256, 574 and 2500 elements were then normalised with the analytical solution and can be seen on the plot in Figure 5.12, together with the results from [30], which demonstrates their convergence.

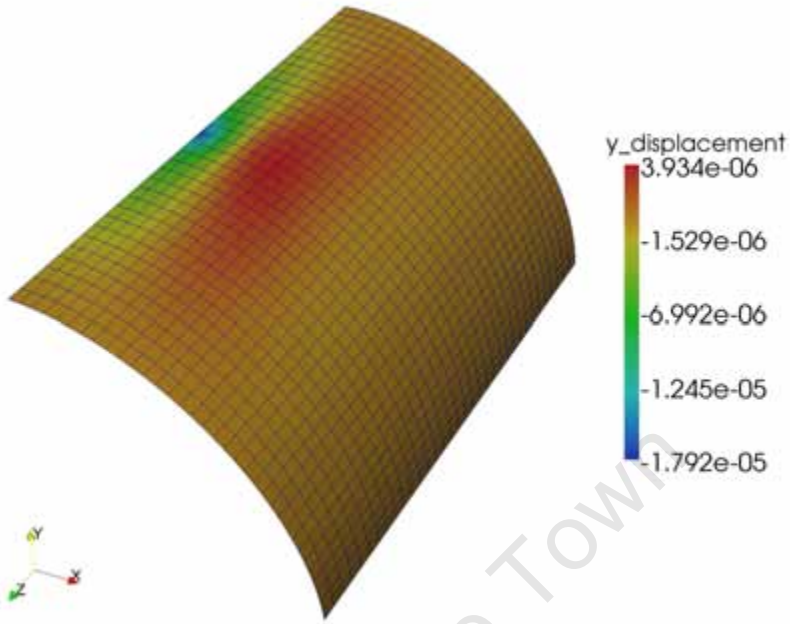

Fig. 5.11. Deflection results for the pinched cylinder test

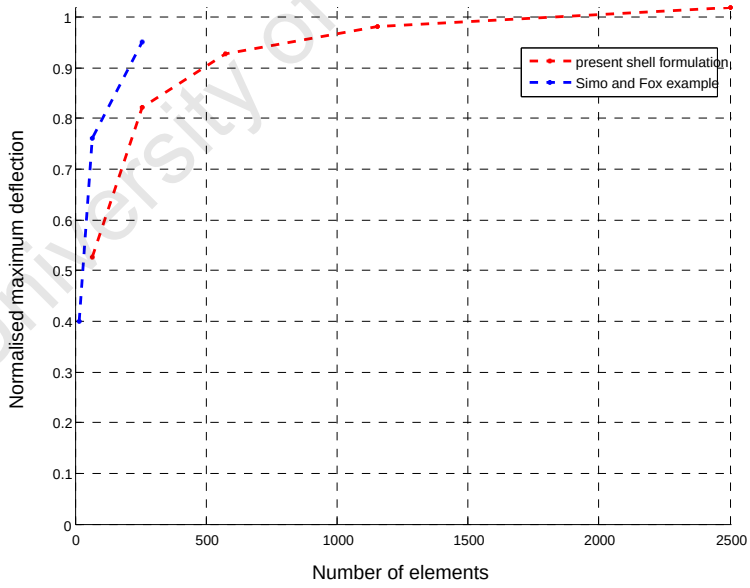

Fig. 5.12. Normalised pinched cylinder deflection results for a range of mesh refinements

5.4 Anisotropy in a plate in tension

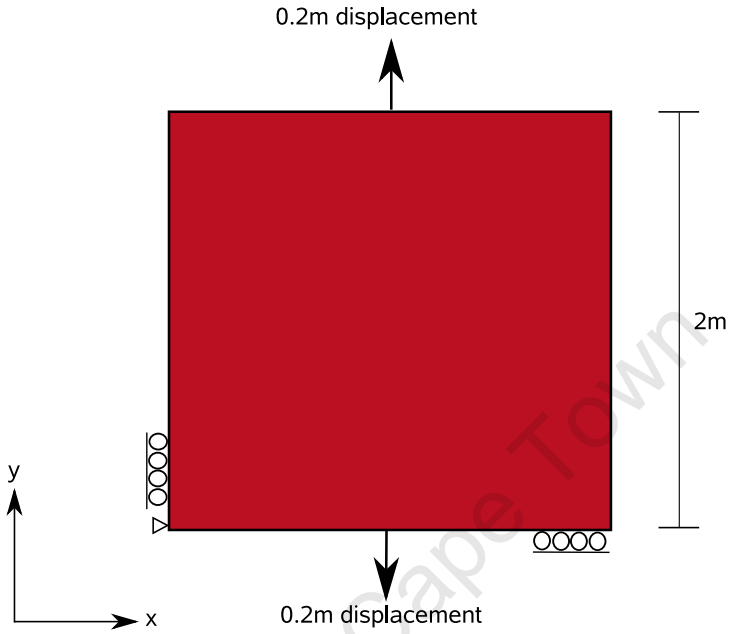

Fig. 5.13. The setup for testing the functionality of the transverse anisotropy formulation

In this example we examine the effects of transverse isotropy in a flat plate subjected to a prescribed displacement in the y-direction. Using a square plate, as in Figure 5.13, simulations were performed using two substantially different fibre angles of 10° and 45° respectively from the horizontal axis. Each plate was designated one family of fibres with the angle orientated anti-clockwise from the x-axis. For this example the plate has a thickness of $h = 0.74$ with the following material properties: $E = 10.0\,e^3$, $\nu = 0.33$ and $k_1 = 2.128\,e^3$. Figures 5.14 – 5.16 show the contours of the x-displacement with and without the inclusion of fibres. For viewing purposes the deformation, which is indicated by the shading on the figures, is displayed on the undeformed geometry. The fibres can be seen to encourage a displacement in accordance with their orienation.

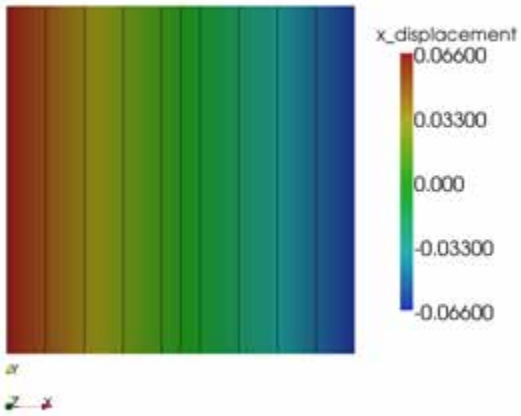

Fig. 5.14. Contour lines of x-displacements for the flat plate without fibres

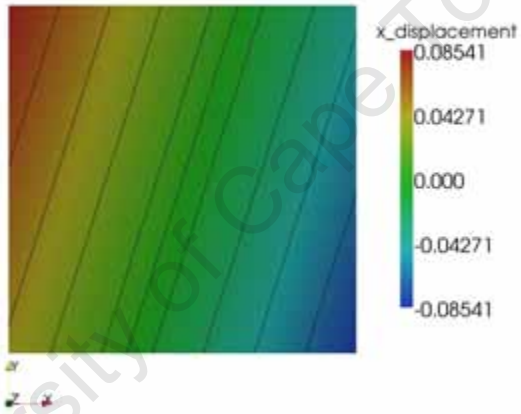

Fig. 5.15. Contour lines of x-displacements for the flat plate with a fibre angle of 10° to the x-axis

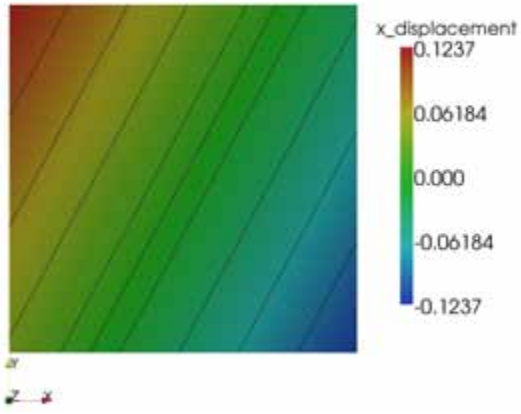

Fig. 5.16. Contour lines of x-displacements for flat plate with a fibre angle of 45° to the x-axis

The graph of Figure 5.17 shows how the shallower fibre angle restricts the x-displacement by effectively adding additional stiffness to the structure, whilst the increased angle allows more lateral motion, thereby decreasing the plate stiffness.

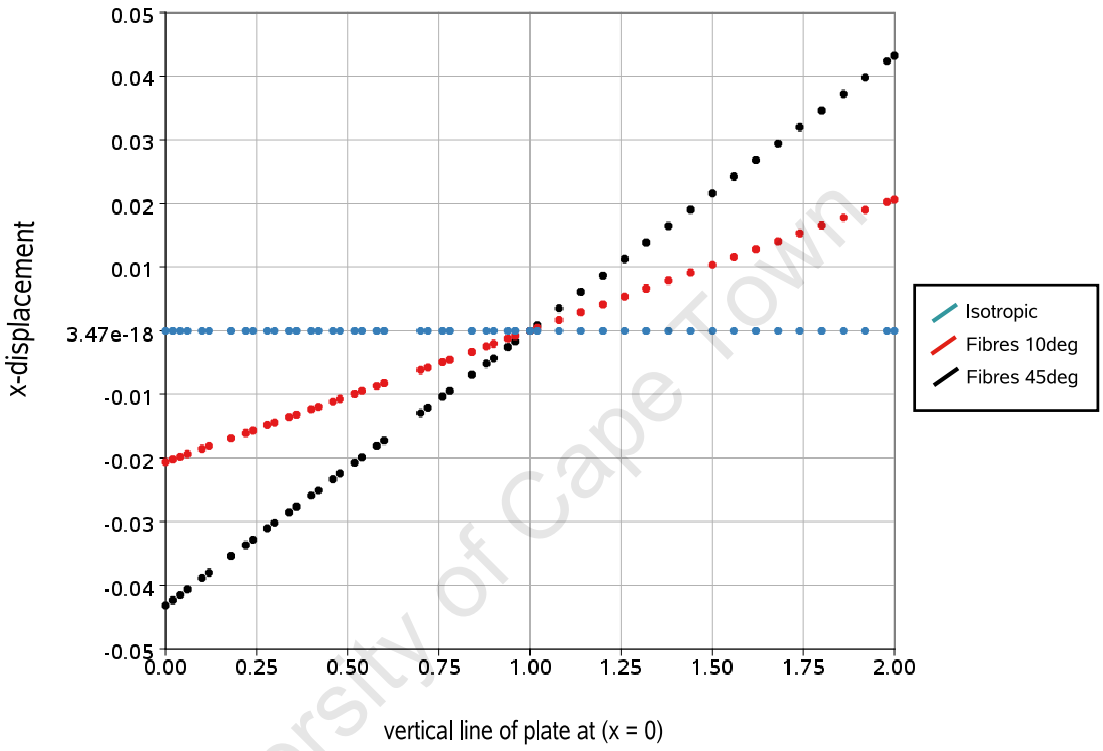

Fig. 5.17. Plot over the midline of the plate, for a constant x, comparing x-displacements for different fibre configurations

6

Biomedical applications

The basis for the development and implementation of a shell theory was for modelling thin biological tissues. This chapter will consider two applications: (a) surgical arterial clamping, and (b) the modelling of leaflets within a prosthetic heart valve.

The relevant biomedical background is given, after which the results of simulations are presented. The effects of anisotropy in each problem are also considered.

6.1 The clamped artery problem

6.1.1 Background

During surgery arterial clamps are an essential means to arrest the flow of blood. However, various injuries to the vessel wall can result from such a procedure. This can lead to short and long-term complications for the patient. Issues such as vessel obstructions which could lead to bleeding and subsequent blockages after the operation, and excessive thickening of the internal arterial layer over time due to tissue growth in the affected region, are two concerns [28]. The choice of clamp, therefore, is important to its efficiency in terms of restricting blood flow as well as in

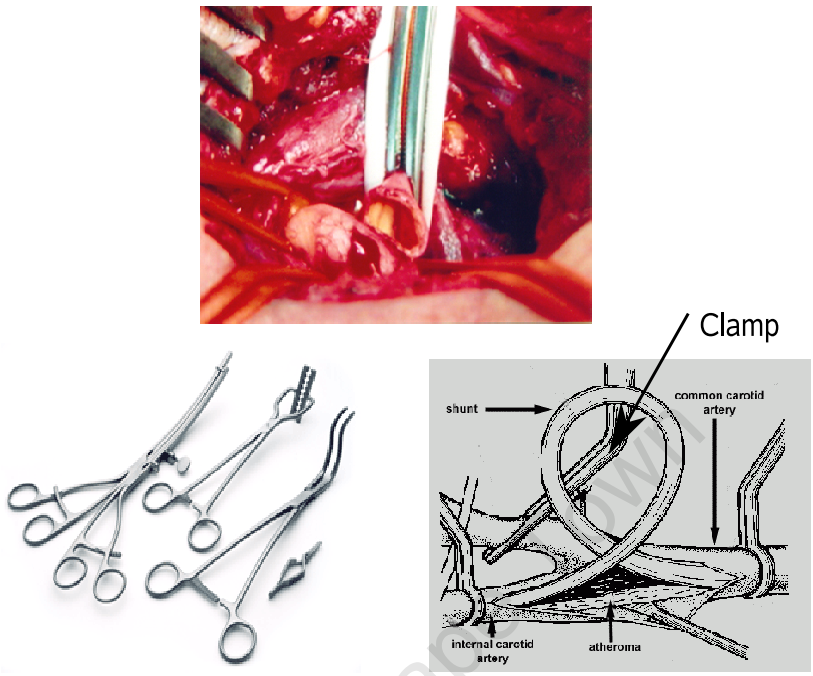

Fig. 6.1. Diagrams illustrating arterial clamping in practice and some examples of the tools used, taken from [1], [2] and [3]

bringing about minimal harm to the tissue. The damage that may be caused by a clamp could be due to the clamping force used, the geometry of the clamp, the type, and hence properties, of the specific artery in question. Schulze–Bauer et al. [28] sought to model this problem with a view to optimising the clamping procedure, which would lead to the improvement of clamp designs. Computational approaches are important in light of the restrictions and cost of experimental testing and the fact that the approach to arterial clamp design has not, in the past, taken into account the mechanical process of clamping and its resulting wall stresses.

The few experimental studies that have been performed have allowed for the identification of the key clamp-induced issues, but do not aid the process of

designing better clamps or adjusting their usage parameters. Computational modelling can give important information surrounding the stress-strain distribution in the arterial walls.

Schulze–Bauer et al.[28] implemented a three-dimensional finite element model, modelling the artery as a nonlinear material with two layers and reinforced by fibres. These two layers are representative of the media and adventitia, which are the middle and outer layers of the artery respectively. Fibrous constituents are arranged in two helical families set at angles depending on the layer in which they are present. Schulze–Bauer et al. [28] also modelled this problem in the large-strain domain, and included the effects of residual stresses. Figure 6.2 illustrates the arterial layers as well as their properties.

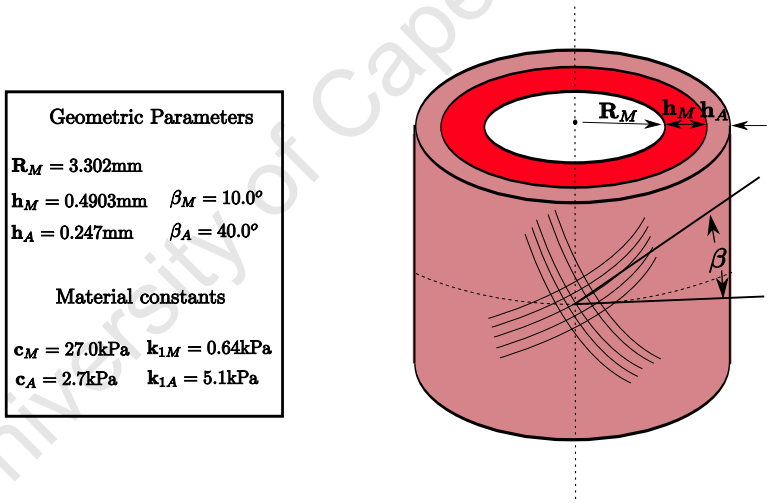

Fig. 6.2. Illustration of the two arterial layers and their parameters, utilised by [28]

6.1.2 The shell formulation

The objective is to qualatively replicate the results achieved by [28] using our small-strain shell formulation. The nature of shells means that for the purposes of this analysis the properties in the two layers have to be smoothed. We will investigate the effect of anisotropy by modelling the artery with and without helical fibres, and by the effect of angle on the deformation.

The flow of blood is represented by an internal pressure acting normal to the shell surface. In the case of this specific biological material we assume near-incompressibility and use a value of Poisson's ratio of $\nu = 0.49$. From the data pertaining to the two arterial layers above, a shell thickness of $h = 0.74mm$ was used with an artery radius of $R = 3.5mm$. This is quite obviously a thick shell. The averaged Young's modulus is calculated using the parameters set up in [28] as follows: By using the parameters of the media and adventitia layers, described in Figure 6.2, the Young's modulus for each layer can be determined by the relation given in (2.75) between the shear modulus c and E. Assuming that each layer experiences the same strain during a uniaxial deformation, the total stress in the artery is given by

$$\begin{aligned}\sigma_h &= \sigma_M h_M + \sigma_A h_A \\ &= E_M \varepsilon_M h_M + E_A \varepsilon_A h_A \\ &= (E_M h_M + E_A h_A)\, \varepsilon,\end{aligned}$$

so that

$$\begin{aligned}E &= \frac{\sigma}{\varepsilon} \\ &= \frac{E_M h_M + E_A h_A}{h} \\ &= \frac{(80.46)\,(0.493) + (8.046)\,(0.247)}{0.493 + 0.247} \qquad = 56.3 \text{ kPa.}\end{aligned}$$

Symmetry conditions are employed, as presented schematically in Figure 3.4, and half an artery is analysed. To prevent free body motion the line $x = 0$, $y = R$ is prescribed to have zero displacement in the x-direction. The end of each artery is allowed to expand in the direction of the outward normals, without axial motion, and the director vectors are prescribed to remain constant. According to [28] the blood pressure used is 13.33kPa. The result is illustrated in Figure 6.3

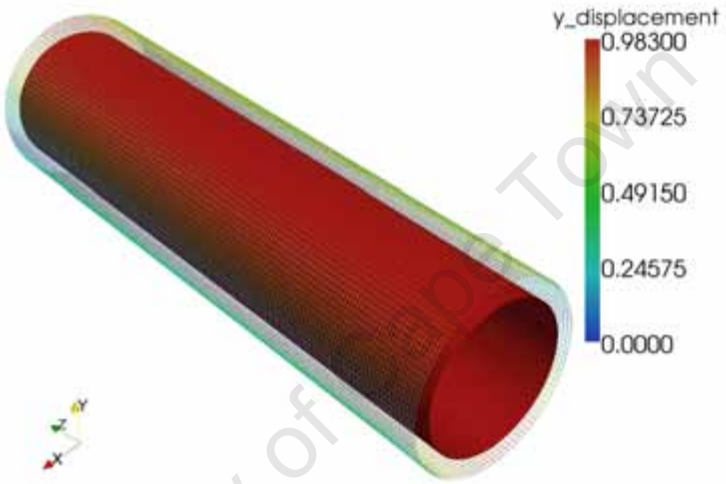

Fig. 6.3. The wire frame shows the y-displacement of inflated artery after the imposition of a blood pressure of 13.33 kPa

A prescribed displacement mimics the clamping action and is imposed in combination with the uniform pressure. The type of clamp considered for this test is a cylindrical one of radius $3mm$. The way in which this cylindrical clamping was achieved was by prescribing a fixed displacement to the affected region of the artery consistent with a cylindrical indentation. At each point where there was a prescribed displacement, the new director vector needed to be determined and the boundary conditions adjusted to take into account what the correct value of $\boldsymbol{\Delta T}$ should be. Figure 6.4 shows the setup.

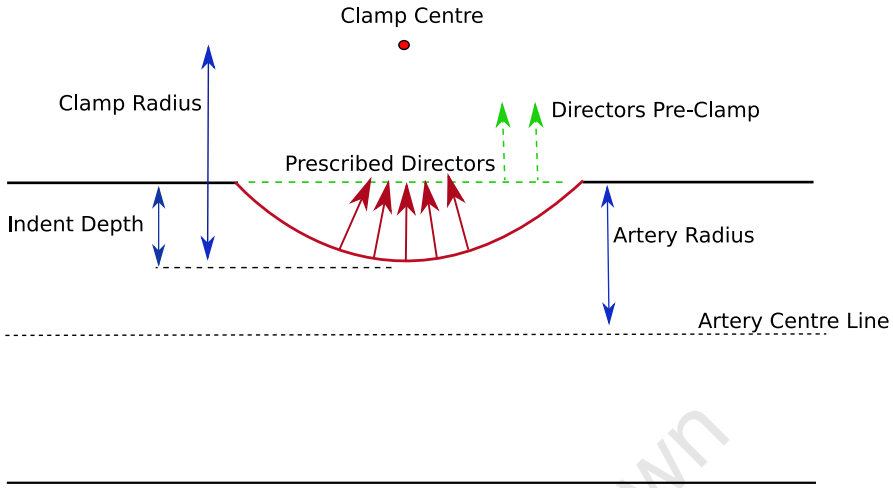

Fig. 6.4. The prescribed boundary condtions for the implementation of the required depth of arterial clamping

Figure 6.5 shows the initially pressurised artery followed by its state after the maximum prescribed clamp indentation.

Six clamping states were considered ranging from an indentation depth of $0mm - 2.5mm$. The images in Figure 6.6 show the results obtained for these clamping states. The colour distribution shows variation in vertical displacement. The deformations to the artery model, shown stage by stage, compare well with those obtained by [28].

(a) Pre-clamping configuration

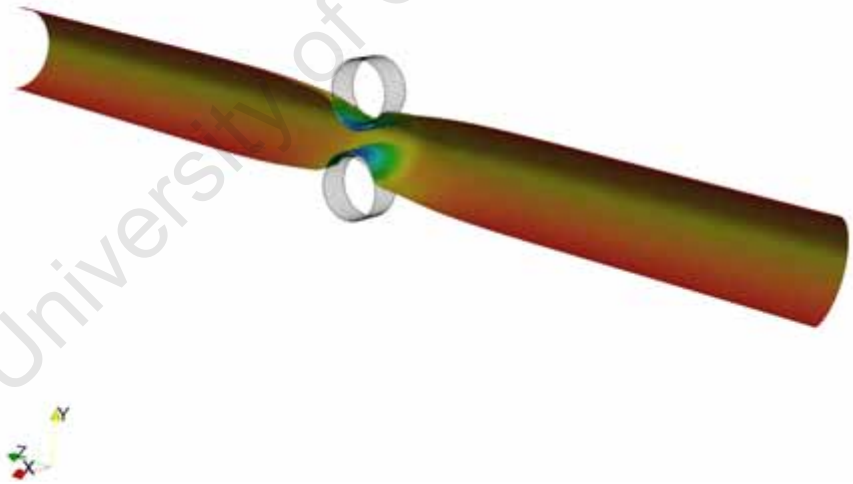

(b) Post-clamping configuration

Fig. 6.5. Demonstration of the clamping setup as performed in this study

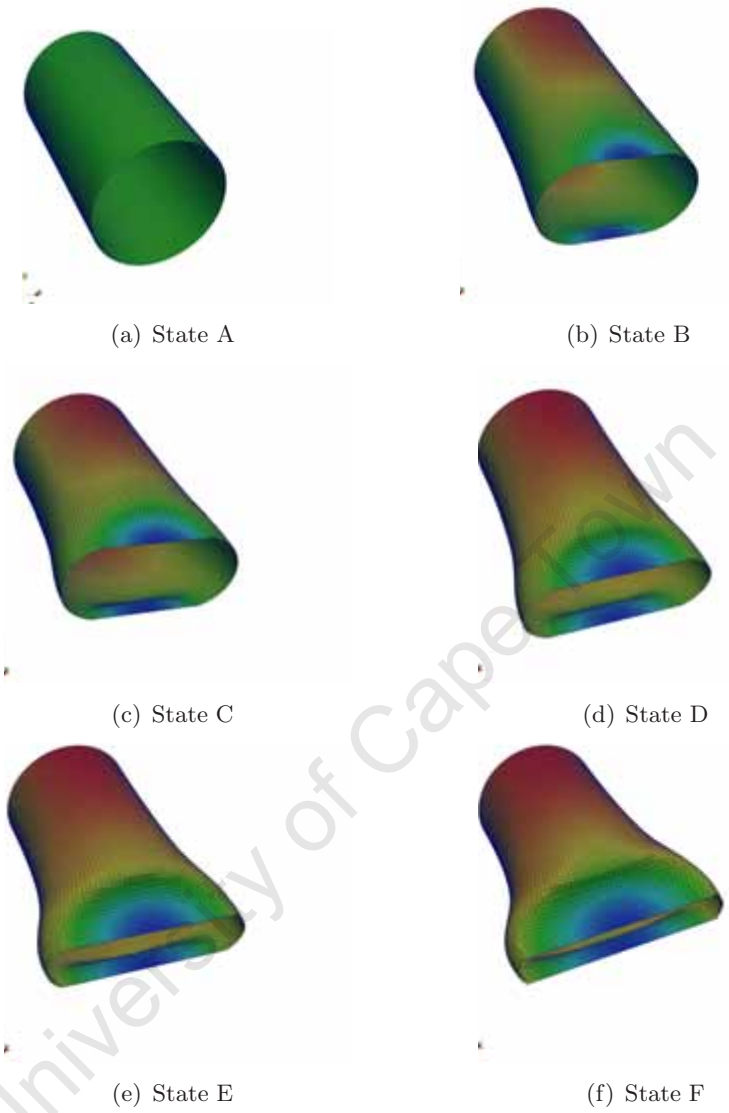

(a) State A (b) State B

(c) State C (d) State D

(e) State E (f) State F

Fig. 6.6. Stepping through the arterial clamping states from an indentation depth of 0.0 to 2.5mm

6.1.3 The effect of arterial anisotropy

Using a clamp indentation depth of $2.5mm$ we now demonstrate the effect of anisotropy. Schulze–Bauer et al. [28] used two different families of helical fibres for each arterial layer, from Figure 6.2, $\beta = 10$ degrees and $\beta = 40$ degrees respectively.

As shown in (2.85), a material constant k_1 is needed to determine the D_{fib} matrices to be added to the system for the case of transverse isotropy. A similar procedure to that of determining the Young's modulus from the values given in 6.2, was used to calculate the k_1 constant used here. The effects of the fibre inclusion are clearly visible in Figure 6.7.

The steeper angle out of the two heilical fibre families seemed to restrict the displacements seen in the clamped artery. As mentioned previously, Schulze–Bauer et al. [28] modelled an artery with two layers. Their outer layer , or adventitia ($\beta = 40$) is much stiffer than the inner layer, or media ($\beta = 10$). As a result, at the junction between the two layers, the more flexible inner layer experiences a large increase in stress, in comparison to the stress at its internally free side. These increased stresses show how the outer layer limits the expansion and restricts the motion of the inner layer. Figure 6.7(b) therefore, with its restricted expansion in comparison to 6.7(a), would seem to be behaving in accordance with those results.

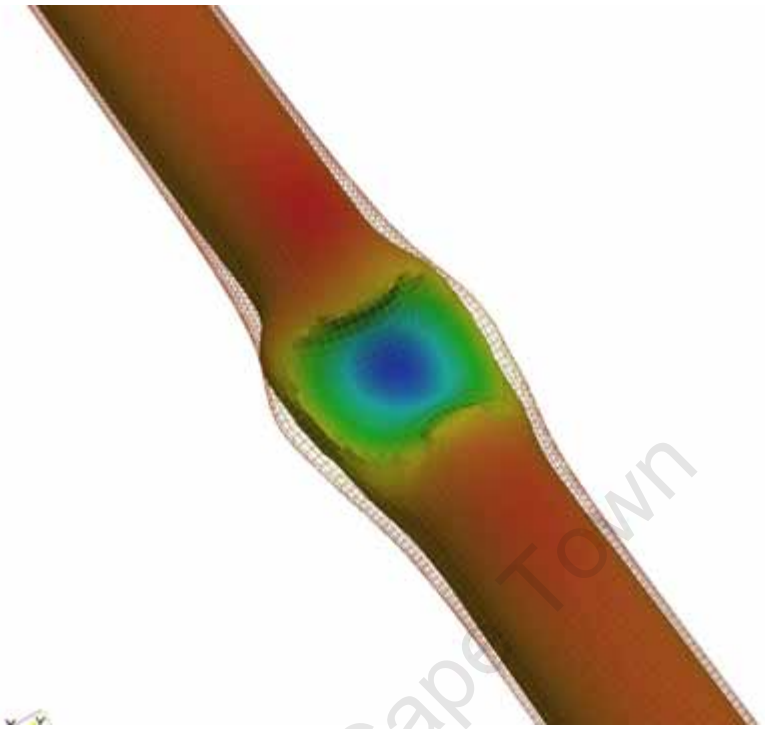

(a) Fibre angle $\beta = 10^{o}$

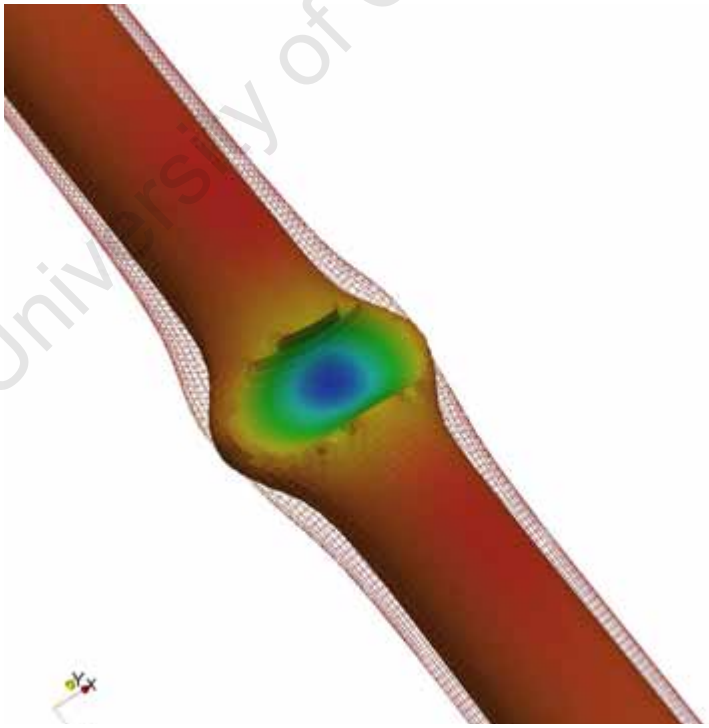

(b) Fibre angle $\beta = 40^{o}$

Fig. 6.7. Comparison between 2.5mm clamped result using the fibre family orientation in the media and adventita respectively. The arterial layers are overlayed with a wire-mesh showing the isotropic result

6.2 The aortic heart valve

6.2.1 Background to the cardiovascular system and aortic valves

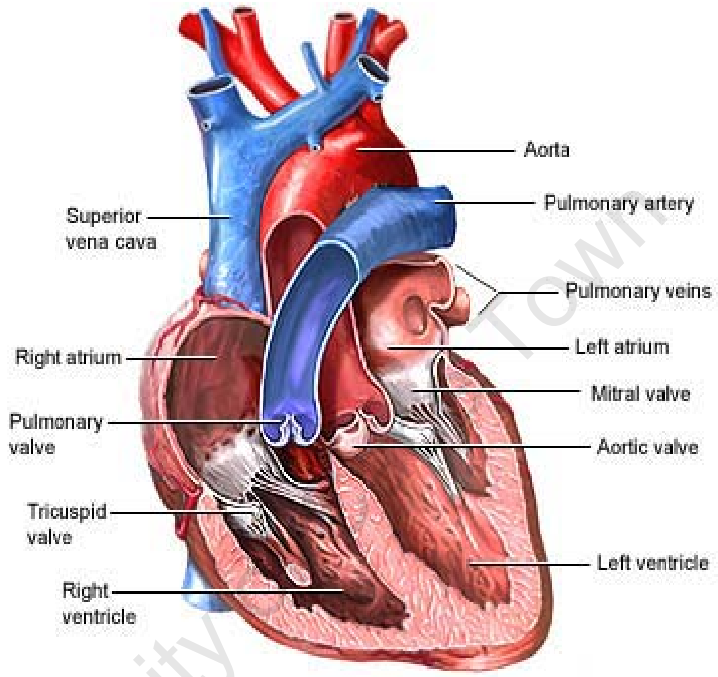

Fig. 6.8. Descriptive view of the heart showing the arrangement of valves and chambers, obtained from [7]

There are two circuits within the human body maintaining blood pressure and motion. The first of these is the systemic circuit which delivers oxygenated blood to the body and returns deoxygenated blood back to the heart. The second is the pulmonary circuit whose function is to send the deoxygenated blood to the lungs and return oxygenated blood once more to the heart. Within the heart the two circuits function separately by making use of four chambers, namely two atria and two ventricles. Figure 6.8 shows a section through the chambers in the heart.

In the pulmonary circuit blood is pushed from the right ventricle into the pulmonary artery to the lungs and returned into the left atrium via the pulmonary vein and subsequently the left ventricle. It is at this point that it is transferred to the systemic circuit. Blood is now ejected into the aorta which in turn branches out into the rest of the body. To maintain uni-directional flow the heart has four valves, one present at each in-flow and out-flow of the ventricles. The valve between the right atrium and right ventricle is known as the tricuspid valve, and leading out of the right ventricle is the pulmonary valve. The intake valve for the left ventricle is known as the mitral valve and finally the valve between the left ventricle and all other arterial branches of the body is the aortic valve.

There are two phases of interest in the cardiac cycle. The first process is known as diastole or the filling phase, when the ventricles prepare for ejection by filling with blood. During this phase the aortic and pulmonary valves are shut, preventing back-flow from the arteries. The second phase is known as systole or the emptying phase, and this is when blood is forcefully pushed out of the ventricles and through pulmonary and aortic valves. During the second phase, the tricuspid and mitral valves are shut [25].

Of interest in this study is the aortic valve. Figure 6.9 shows its structure; it can be seen to consist of three leaflets and three, somewhat bulging, regions behind them, known as the sinuses of Valsalva. The leaflets undergo large deflections during the processes of diastole and systole, bearing its load during diastole whilst in the closed position. In the human body an aortic leaflet ranges in thickness from $0.25mm$ to $1.1mm$ at various regions. During diastole the pressure gradient over the valve leaflet is about 10.67kPa and during systole the blood pressure is of the order of 16kPa.

6.2.2 Some comments on previous computational work

Since the aortic valve is the primary controller of the distribution of oxygenated blood to the body, its malfuntioning in terms of restricted opening or allowing

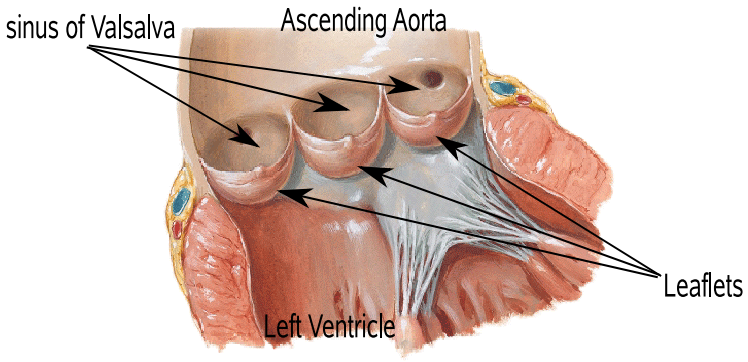

Fig. 6.9. From [25], a detailed illustration of the aortic heart valve

backflow from the arteries can adversely affect the quality of life of an individual and can result in fatalities. In many cases valve replacement can offer improved cardiac functioning and increase the lifespan of affected patients. Currently available valve prostheses are either mechanical or biological, with each offering advantages and disadvantages in terms of their functioning, durability and need to be combined with anticoagulant treatment [31]. Figure 6.10 shows a commercially available prosthetic heart valve. Finite element models of the aortic valve have been used successfully to gain an understanding of the mechanics behind real and prosthetic valves as well as of their probable causes of failure [26].

Heart valves are inherently anisotropic and exibit nonlinear material behaviour. Figure 6.11 clearly displays the predominant fibre orientation in a human aortic leaflet. Koch [25] sought to capture the effects of anisotropy and nonlinearity in valve leaflets by performing a comparative analysis on linear elastic and hyperelastic materials, with and without anisotropy, using a three-dimensional model. He obtained the parameters for the exponential strain energy function for a hyperelastic material by performing tension tests on fresh porcine aortic valve

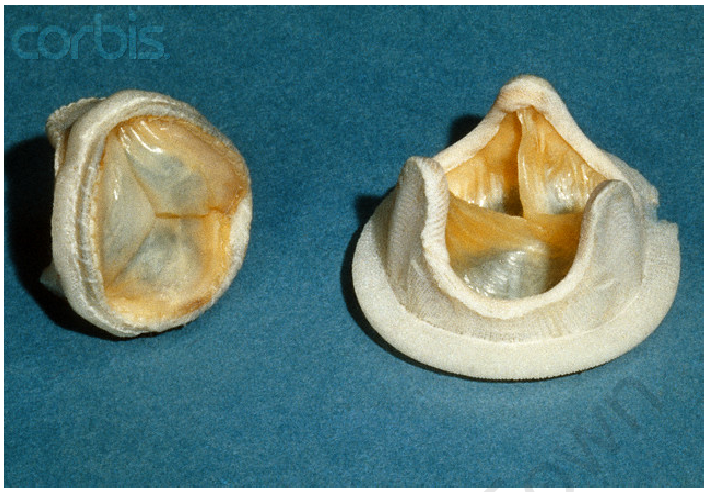

Fig. 6.10. An example of a prosthetic aortic valve

leaflets. His conclusion was the affirmation of the noticable effect of anisotropy, aligning the maximum pricipal stresses with the fibre distribution in the leaflet.

In the natural valve, fibre reinforcement is the predominent stress-reducing factor. The fibres run along the leaflet starting and ending at either side of the leaflet-aortic attachment line, as seen in Figure 6.11. This property means that by way of the fibres the load on the leaflet can be transfered to the artery wall. Cacciola in [21] was concerned with the issues facing three-leaflet prosthetic aortic valves, which, although very similiar to those biologically present, were not being used in patients in vivo due to fatigue failure in the leaflet. She sought to design, analyse, manufacture and test these types of valves focusing on fibre reinforcement to reduce the problematic stresses present that had hindered previous designs. She considered various concentrations and orientations of fibres into a EPDM (Ethylene-Propylene-Diene-Monomer rubber matrix). Her numerical testing

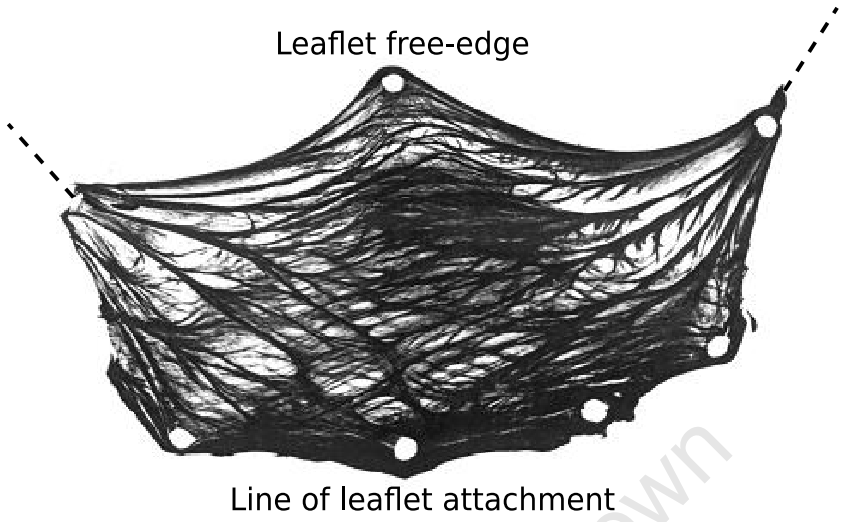

Fig. 6.11. Porcine aortic valve leaflet, clearly demonstrating its fibre orientation, adapted from [25]

revealed that the leaflet material could experience a stress reduction of up to 60% due to fibre reinforcement.

6.2.3 The shell model of a leaflet

The thickness of different prosthetic valve prototypes ranges from $0.16mm$ to $0.23mm$ [16] with an expected ventricular diameter ranging between $22mm$ to $28mm$. This range of thickness-to-diameter ratios renders the aortic leaflet a prime candidate for modelling using a shell model. The objective of this approach is once again to correlate qualitively the valve leaflet response with that of other studies, and in particular to gauge the effect of including an appropriately specified fibre component to the leaflet model.

Using the methodology from [16], the leaflet model geometry can be constructed by taking a section of a cylinder as illustrated in Figure 6.12.

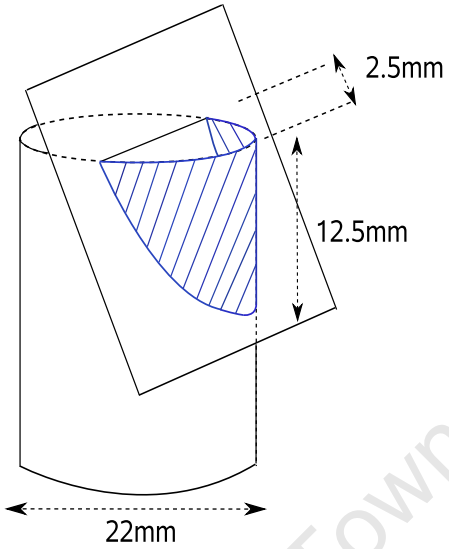

Fig. 6.12. How the aortic valve leaflet is geometrically constructed for modelling purposes

The parabolic curve of the leaflet geometry is attached to the aortic wall as indicated in Figure 6.13, where the arrangement of all three leaflets can be seen. Note the geometry of the leaflet is constructed for the open leaflet configuration, and Figure 6.13 shows the closed valve for schematic purposes.

The setup for the shell formulation, as previously described, is the linearised form whereas Koch [25] made use of a nonlinear formulation. Specifically the hyperelastic properties he makes use of allows for intial flexibility in the small strain region, followed by a rapid increase in stiffness as it moves into larger deformations. Since we are modelling small strains in this study, the value of E used for the leaflet is taken from [25] for the small strain region and is determined from the shear modulus c he uses (represented in our formulation as G) by use of the relation in (2.75). For $c = 27.3732$ kPa we calculate $E = 81.572e^3$ kPa. We again approximate material incompressibility with $\nu = 0.49$, make use of a leaflet thickness of 0.2mm and utilise the diastolic pressure, 10.67kPa, for the leaflet loading.

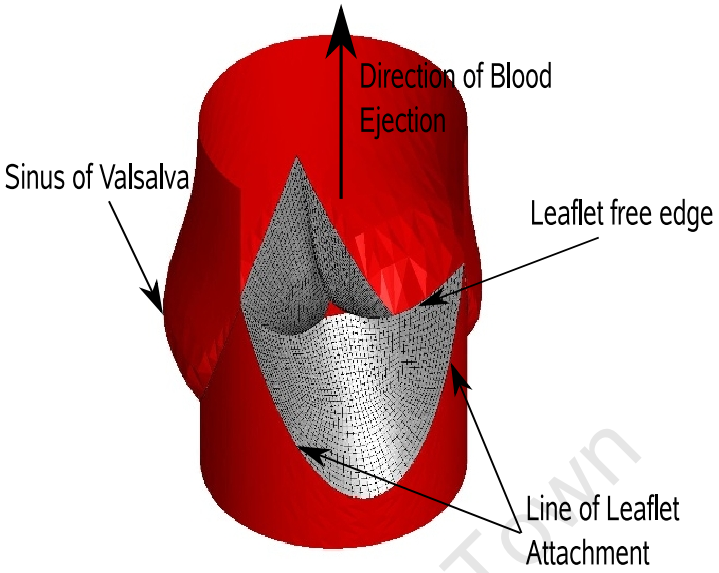

Fig. 6.13. Demonstrative illustration of how leaflet model fits into general arrangement of aorta, adapted from [8]

In order to simulate leaflet attachment and diastolic loading, the parabolic edge of the leaflet model was fixed in all displacement and director degrees of freedom and a uniform pressure load applied normal to the entire surface. Figure 6.14 shows the change obtained from the initial to the deformed configuration. The leaflet deforms inwards in a symmetrical manner with the same deformed shape visually as those in [16].

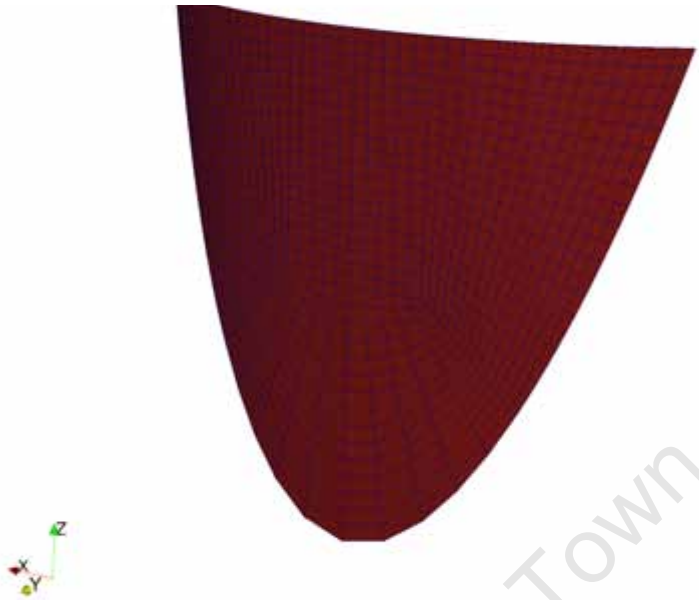

(a) Undeformed or open position

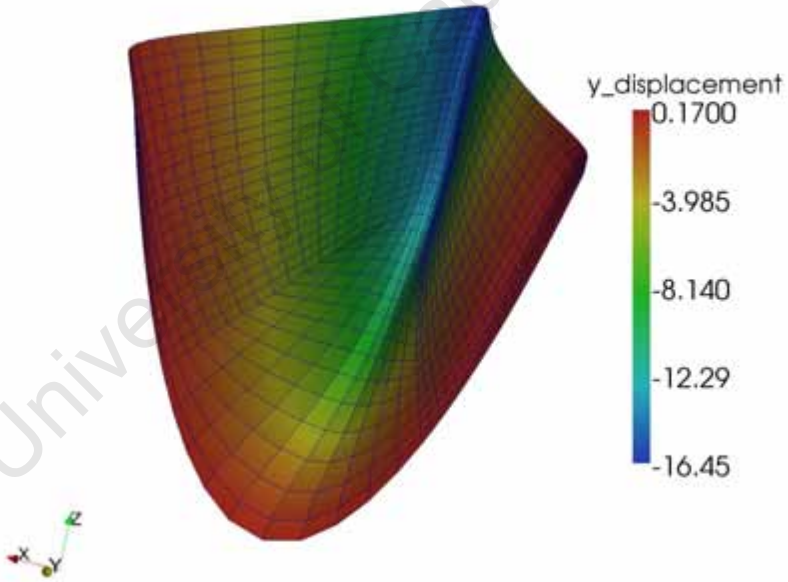

(b) Deformed or closed position

Fig. 6.14. The isotropic case: undeformed configuration of the heart leaflet model compared to the loaded response

6.2.4 The Effect of Leaflet Anisotropy

Anisotropy was added to the leaflet model in the same manner as in the clamped artery problem. To mimic the real leaflet fibre arrangement angles of orientation for the two fibre families needed to be quite shallow. It was therefore decided to use $\beta = \pm 5^o$, relative to the horizontal in Figure 6.14. The next concern is to gauge the effect of the fibres through the material constant k_1 in (2.85). Since this information was not available, an initial estimate was based on keeping the ratio of $\frac{E_{\text{artery}}}{k_{1\text{artery}}}$, from the artery tests above, constant. This was found to bring about far too much rigidity within the leaflet, and thus a few different parameters were tested, resulting in the selection of the value $k_{1\text{leaf}} = \frac{E_{\text{artery}}}{k_{1\text{artery}} \times 40}$.

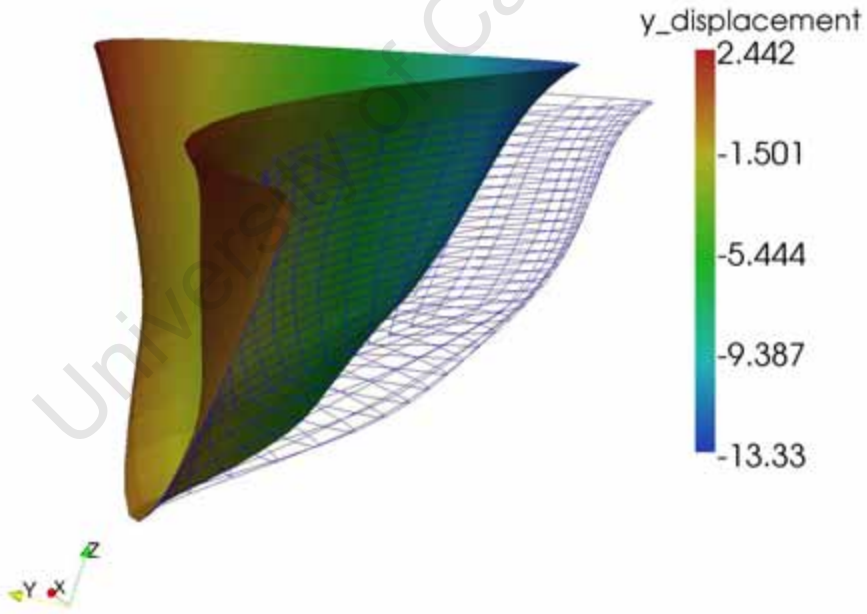

Fig. 6.15. Effect of anisotropy on the shell leaflet model

In Figure 6.15 the effect of fibre reinforcement is shown. The internal region of the leaflet is seen to experience less deformation while the region surrounding the line of

leaflet attachment experiences increased deformation in comparison to the isotropic result. Figure 6.16 also presents this notable change due to the fibres by giving the displacement values obtained for the isotropic and transversely isotropic cases.

These results support the conclusion reached by Cacciola [16]. The fibres had the effect of reducing the displacements of the middle of the leaflet while transferring additional stress to the line of leaflet attachment, and hence, the artery wall.

	Isotropic Leaflet	Anisotropic Leaflet
Interior deflection	-16.45	-13.33
Exterior deflection	0.17	2.442

Fig. 6.16. Comparison between the deformation distribution of an isotropic and anisotropic leaflet

7

Conclusions and recommendations

7.1 Conclusions

The work presented in this thesis covers a wide scope of objectives. The intial motivation was to model soft biological tissues considered to be thin. The first goal was the clear presentation of a complex shell theory and its approximation using the finite element method, followed by a step-by-step explanation of the implementation process using appropriate programming techniques and software. From there, this study sought to validate the approach taken with specific benchmark problems, notably those for thin shells, and with the inclusion of transverse isotropy. Finally, the background, method and results for two examples from biomechanics, namely the clamped artery problem and the prosthetic heart valve leaflet, were presented.

The shell theory due to Simo and Fox [29] has been presented logically, with enough detail to enable a researcher in this field to easily understand each step in the process. The finite element approximations for this theory were also presented clearly and systematically, additionally discussing the implementation of boundary conditions and the methodology for dealing with the thin shell limit.

With regard to implementation, the preprocessing phase allowed for a shell surface to be successfully constructed, meshed and subsequently interrogated using a MATLAB routine. This prepared the required input decks for deal.II so that the

traversing of a two-dimensional mesh with associated director vectors and three-dimensional position vectors could be obtained with ease. The preprocessing also ensured that the connectivity of the mesh was maintained, and allowed for the allocation of boundary identities to assist with the implementation of boundary conditions.

Setting up the algorithm using deal.II involved utilising their suite of finite element classes along with additional classes created specifically for the shell forumulation. Within this structure, additional amendments were made that enabled various shell examples to be run for thin shells, for problems with specialised boundary conditions, and the inclusion of directional fibre families into the material.

Even though deal.II does not currently have the capability to work directly with a surface in three-dimensional space, its functionality is such that the intricacies of the shell formulation could be handled adequately for the purposes of this dissertation. At present, the structure of deal.II is being extended to provide the additional routines to handle these types of meshes. Additionally, as a platform for this research deal.II is able to cater for a broad range of extensions and is able to solve computationally challenging complex problems due to its parallel capabilities. The decision to use deal.II was, thus, a good one.

The benchmark problems attempted compared favourably with the analyical solutions available. Cook's membrane test validated the shell element for in-plane problems, the clamped plate test demonstrated its accuracy for bending related problems and thin shells, the pinched cylinder test showed correct behaviour for curved shells and lastly, the plate anisotropy test behaved as expected for varying fibre orientations. The success of these examples allowed us to have confidence that the implementation of the theory had been a success and that problems in biomechanics could be attempted.

The problem of surgical arterial clamping was modelled using a cylindrical geometry, specifying an internal surface load to model blood pressure, specifying the

displacements and director changes using an appropriate clamp geometry and indentation depth and finally, by specifying material properties and transverse isotropy in accordance with the literature. Visually, the results of a range of clamp depths attempted matched those achieved by Schulze–Bauer et al [28]. There was also a significant difference in the solution when fibre directionality was included. The different fibre orientations attempted showed results that qualitatively match the stress experienced in the arterial layers given by Schulze–Bauer et al [28].

The process of modelling a prosthetic valve leaflet involved constructing the geometry as set out in [16], using material properties and loading conditions based on the work of Koch [25] and Cacciola [21] and also including fibre effects in the same manner as Schulze–Bauer et al [28]. The results displayed the correct displaced shape of an aortic valve leaflet during diastole. The inclusion of fibres decreased the strain experienced at the centre of the leaflet and increased the strain experienced at the line of leaflet attachment, effectively allowing the load to be carried by the aortic wall, as expected by [16].

In summary, the aims of this thesis have been met successfully.

7.2 Recommendations

The Simo and Fox shell theory has been implemented and validated for the case of small strains as well as linear isotropic and transversely isotropic elasticity. It is recommended that the continuation of this work should focus on adding functionality for large strains and nonlinear material models. These additions, as well as that of including fluid structure interactions, would allow the simulations to model soft biological tissues and their environment more realistically. The shell formulation was implemented, using the open-source library of code deal.II, with the possibility of these developments in mind.

For the scope of this study and examples attempted, the preprocessing methods were sufficient. Due to the current framework of deal.II, it is further recommended that more complex geometries be considered, with further mapping options to accomodate them.

References

[1] http://www.jvascbr.com.br/04-03-02/04-03-02-131/04-03-02-131.htm. Accessed: 08-04-2009.

[2] http://www.bikudo.com/product_search/details/13797/debakey_clamp.html, . Accessed: 08-04-2009.

[3] http://www.gvg.org.uk/carimags.htm, . Accessed: 08-04-2009.

[4] http://adsabs.harvard.edu/abs/1965ArRMA..20..287G. Accessed: 12-04-2009.

[5] http://cubit.sandia.gov/index.html. Accessed: 17-04-2009.

[6] file:///home/sam/Programs/deal.II-6.1.0/deal.II/doc/doxygen/deal.II/index.html. Accessed: 17-04-2009.

[7] http://health.allrefer.com/health/mitral-stenosis-heart-valve-surgery-series.html. Accessed: 08-04-2009.

[8] http://www2.imperial.ac.uk/ssherw/bioflow/people/Raoul_van_Loon/Project/main.html. Accessed: 08-04-2009.

[9] http://www.mathworks.com/products/matlab/. Accessed: 17-04-2009.

[10] K. Moreland J. Ahrens A. Cedilnik, B. Geveci and J. Favre. *Remote Large Data Visualization in the ParaView Framework*, 2006.

[11] S. Ahmad, B.M. Irons, and O.C. Zienkiewicz. Analysis of thick and thin shell structures by curved finite elements. *International Journal for Numerical*

Methods in Engineering, 2:419–451, 1970.

[12] W. Bangerth, R. Hartmann, and G. Kanschat. `deal.II` *Differential Equations Analysis Library, Technical Reference*. URL `http://www.dealii.org`. `http://www.dealii.org`.

[13] W. Bangerth, R. Hartmann, and G. Kanschat. deal.II — a general-purpose object-oriented finite element library. *ACM Transactions on Mathematical Software*, 33:24, 2007.

[14] K.J. Bathe and E.N Dvorkin. A continuum mechanics based four-node shell element for general nonlinear analysis. *International Journal for Computer-Aided Engineering and Software*, 1:77–88, 1984.

[15] T. Belytschko and J. Fish. *A First Course in Finite Elements*. John Wiley and Sons, Ltd., Chichester, 2007.

[16] G. Cacciola. *Design, Simulation and Manufacturing of Fibre Reinforced Polymer Heart Valves*. PhD thesis, Eindhoven University of Technology, The Netherlands, 1998.

[17] H. Cohen and C.N. DeSilva. Nonlinear theory of elastic directed surfaces. *J. Math. Phys.*, 6:960–966, 1966.

[18] E. Cosserat and F Cosserat. Theorie des corps deformables. *Chwolson's Traite de Physique*, 2:953–1173, 1909.

[19] J.L Ericksen and C. Truesdell. Exact theory of stress and strain in rods and shells. *Arch. Rat. Mech. Anal.*, 1:295–323, 1958.

[20] W. Flugge. *Tensor Analysis and Continuum Mechanics*. Springer-Verlag, Berlin, 1972.

[21] P.J.G. Schreurs G. Cacciola, G.W.M. Peters. Effect of fibre orientation on the stress distribution within a leaflet of a polymer composite heart valve in the closed position. *Journal of Biomechanics*, 33:521–530, 2000.

[22] M. R. Gosz. *Finite Element Method - Applications in Solids, Structures, and Heat Transfer*. John Wiley and Sons, Ltd., Florida, 2007.

[23] T.J.R. Hughes. *The Finite Element Method: Linear Static and Dynamic Finite Element Analysis*. Dover Publications, Inc., New York, 2000.

[24] T.J.R Hughes and E. Carnoy. Nonlinear finite element shell formulation accounting for large membrane strains. *Comp. Meth. Appl. Mech. Engng.*, 39: 69–92, 1983.

[25] T. M. Koch. Non-linear finite element analysis of the aortic heart valve. Master's thesis, University of Cape Town, South Africa, 2004.

[26] Y. Liu, V. Kasyanov, and R. T. Schoephoerster. Effect of fibre orientation on the stress distribution within a leaflet of a polymer composite heart valve in the closed position. *Journal of Biomechanics*, 40:1099–1106, 2007.

[27] E. Ramm. A plate/shell element for large deflection and rotations. *Formulations and Computational Algorithms in Finite Element Analysis*, 1977.

[28] C.A.J. Schulze-Bauer, T.C. Gasser, and G.A. Holzapfel. A three-dimensional finite element model for arterial clamping. *Journal of Biomedical Engineering*, 124:355–363, 2007.

[29] J.C. Simo and D.D. Fox. On a stress resultant geometrically exact shell model. Part I: formulation and optimal parametrization. *Computer Methods in Applied Mechanics and Engineering*, 72:267–304, 1989.

[30] J.C. Simo, D.D. Fox, and M.S Rifai. On a stress resultant geometrically exact shell model. Part II: The linear theory; computational aspects. *Computer Methods in Applied Mechanics and Engineering*, 73:53–92, 1989.

[31] I. Vesely. The evolution of bioprosthetic heart valve design and its impact on durability. *Cardiovascular Pathology*, 12:277–286, 2003.

[32] P. Wriggers. *Nonlinear Finite Element Methods*. Springer, Berlin, 2008.